Free electron laser pulse characterization by THz streaking

Kumulative Dissertation
zur Erlangung des **Doktorgrades**
an der Fakultät für Mathematik, Informatik und Naturwissenschaften
Fachbereich Physik
der Universität Hamburg

vorgelegt von
Ivette Jazmin Bermúdez Macias
aus Puebla, México

Hamburg
2022

Universität Hamburg
DER FORSCHUNG | DER LEHRE | DER BILDUNG

Thesis advisors: Dr. Stefan Düsterer and Prof. Dr. Ulrike Frühling   Ivette J. Bermúdez Macias

Free electron laser pulse characterization by THz streaking

Abstract

The goal of this dissertation was to investigate a reliable single-shot pulse duration diagnostic tool for the pulse duration and wavelength range delivered at the Free Electron LAser of Hamburg (FLASH). At Self-Amplified-Spontaneous-Emission-based free-electron lasers (FELs), the radiation parameters - duration, arrival time, energy, spectrum, and spatial distribution - differ for each pulse. A dedicated single-shot diagnostic tool for each parameter is therefore essential in order to interpret the experimental data on a pulse-to-pulse basis.

This work summarizes the effort to realize a temporal diagnostic tool using the streaking technique by building a terahertz (THz) "streak camera". The setup was prepared and calibrated, and various pulse duration measurements with different experimental settings were performed in order to explore and validate the application range of the streaking method. The aspects limiting the temporal resolution using the commissioned streaking setup were characterized experimentally. The pulse duration measurements were analyzed using classical and quantum mechanical streaking theory models. Furthermore, a deep statistical study on the SASE fluctuations was realized using single-shot measurements of various radiation parameters. Scaling laws were derived using theoretical simulations and the measured data. This analysis enabled the intrinsic statistical SASE fluctuations to be disentangled from accelerator-based fluctuations and measurement uncertainties.

Exploiting the capabilities of the THz-streaking setup, fundamental atomic physics questions were also addressed.

Within this thesis, the Post-Collision Interaction (PCI) effect in THz-assisted Auger decay was studied for different noble gas atoms using a semi-classical analytical model. Moreover, a quantum-mechanical description was developed in order to enhance the current methods. Numerical simulations of Auger electron spectra in the presence of a THz field were performed using the semi-classical model for various experimental parameters, focusing on achievable experimental conditions at currently operational FELs and particularly at FLASH. The results revealed the optimal parameter range in which a measurable PCI effect can be expected and were used to prepare PCI experiments at FLASH2 using the THz streaking setup.

iii

Free electron laser pulse characterization by THz streaking

Zusammenfassung

Ziel dieser Dissertation war es, ein zuverlässiges Einzelschuss-Diagnosewerkzeug für den Puls-dauer- und Wellenlängenbereich des Freien Elektronen-Lasers (FEL) in Hamburg (FLASH) zu entwickeln.

Die Strahlungsparameter, die von FELs mit selbstverstärkter Spontanemission (SASE) erzeugt werden, sind für jeden Licht-Puls unterschiedlich. Dauer, Ankunftszeit, Pulsenergie, spektrale und räumliche Verteilung ändern sich von Puls zu Puls. Daher kann eine Diagnose, die puls-aufgelöst die zeitlichen Charakteristik der FEL Pulse vermessen kann, einen wichtigen Beitrag zur genaueren Interpretation von Experimenten an FLASH liefern. Zu diesem Zweck wurde eine Terahertz (THz) "Streak-Kamera" aufgebaut, die in dieser Arbeit vorgestellt wird.

Der Aufbau wurde vorbereitet, kalibriert, und es wurden verschiedene Pulsdauermessungen mit unterschiedlichen experimentellen Parametern durchgeführt, um den Anwendungsbereich der Methode zu erkunden und zu validieren. Durch die Analyse der gewonnenen Daten wurden die Grenzen der zeitliche Auflösung dieses Streaking-Aufbaus untersucht. Die Messungen wurden mit klassischen sowie quantenmechanischen Methoden analysiert. Darüber hinaus wurde eine eingehende statistische Untersuchung der SASE-Fluktuationen anhand von Single-Shot-Messungen verschiedener Strahlungsparameter durchgeführt. Anhand von Simulationen und gemessenen Daten wurden Skalierungsgesetze abgeleitet. Diese Analyse ermöglichte es, die impliziten statistischen SASE-Fluktuationen von beschleunigerbedingten Fluktuationen und Messunsicherheiten zu separieren.

Weiterhin ermöglicht THz-Streaking eine Vielzahl von Pump-Probe-Photoelektronenspektro-skopie Experimenten. Als Beitrag zu grundlegenden Fragen der Atomphysik wurde der Post-Collision Interaction (PCI)-Effekt beim THz-unterstützten Auger-Zerfall für verschiedene Edelgasatome mit Hilfe eines semi-klassischen analytischen Modells untersucht. Darüber hinaus wurde eine quantenmechanische Beschreibung entwickelt, um die bisherigen Methoden zu erweitern. Numerische Simulationen von Auger-Elektronenspektren, in Gegenwart eines THz-Feldes, wurden unter Verwendung des semiklassischen Modells für verschiedene experimentelle Parameter durchgeführt. Hier lag der Schwerpunkt auf den experimentellen Bedingungen, die

mit derzeit im Betrieb befindlichen FELs (insbesondere FLASH) erreichbar sind. Die Ergebnisse zeigen den optimalen Parameterbereich auf, in dem ein messbarer PCI-Effekt erwartet werden kann, und wurden zur Vorbereitung von PCI-Experimenten an FLASH2 mit Hilfe des THz-Streaking-Aufbaus verwendet.

This section summarizes the publications in scientific peer-reviewed journals derived from my work and specifies my contributions. The publications are attached in Appendix A and are referred to as A.1, A.2, A.3 and A.4 in the text.

A.1 **Single-shot temporal characterization of XUV pulses with duration from 10 fs to 350 fs at FLASH.**
R. Ivanov, I. J. Bermúdez Macias, J.Liu, G. Brenner, J. Roensch-Schulenburg, G. Kurdi, U. Frühling, K. Wenig, S. Walther, A. Dimitriou, M. Drescher, I. P. Sazhina, A. K. Kazansky, N. M. Kabachnik and S. Düsterer. 2020 J. Phys. B: At. Mol. Opt. Phys. 53 184004

I analyzed and interpreted the majority of the experimental data with the supervision of S. Düsterer. The experiment was performed half a year before I started my PhD by S. Düsterer, R. Ivanov and J. Liu. I developed part of the theoretical simulations using N.M Kabachnik and A. K. Kazansky's model. U. Frühling, K. Wenig, S. Walther and A. Dimitriou measured and analyzed the Auger spectra. R. Ivanov, S. Düsterer, N.M Kabachnik and I prepared the initial manuscript. All of the other co-authors have provided suggestions and proof-reading to finalize the manuscript.

A.2 **Study of temporal, spectral, arrival time and energy fluctuations of SASE FEL pulses.**

I.J. Bermúdez Macias, S. Düsterer, R. Ivanov, J. Liu, G. Brenner, J. Roensch-Schulenburg, M. K. Czwalinna, and M. V. Yurkov. Opt. Express 29, 410491 − 10508 (2021).

I analyzed the experimental data and interpreted the experimental results presented with the supervision and approval of S. Düsterer. M.V. Yurkov performed the numerical simulations and wrote the theoretical part of the paper. S. Düsterer, R. Ivanov and J. Liu performed the experiment half a year before I started the PhD thesis. S. Düsterer and I wrote and prepared the manuscript. All of the other co-authors have provided suggestions and proof reading to finalize the manuscript.

A.3 **Post-collision interaction effect in THz-assisted Auger decay of noble gas atoms.**

I.J. Bermúdez Macias, S. Düsterer, R. Ivanov, U. Frühling, and N. M. Kabachnik. 2021 J. Phys. B: At. Mol. Opt.Phys. 54085601.

U. Frühling, S. Düsterer and I suggested and developed the concept of the systematic studies of PCI experiments at FLASH2. Based on preliminary work done by S. Bauch and M. Bonitz, I developed the code and performed the numerical simulations with the guidance of N.M. Kabachnik. I interpreted the numerical results together with N.M. Kabachnik and wrote and prepared the initial manuscript. All the coauthors contributed to the interpretation of the results and the final version of the manuscript.

A.4 Time-dependent postcollision interaction effects in THz-field-assisted Auger decay.

I.J. Bermúdez Macias, S. Düsterer, R. Ivanov, and N. M. Kabachnik. Physical Review A. Accepted.

N.M. Kabachnick and I proposed and developed the novel theoretical model as well as performed the computational simulations. I interpreted the numerical results and prepared the initial manuscript with the help of S. Düsterer, R. Ivanov and N.M. Kabachnik. All the coauthors contributed to the final version of the manuscript.

Additional Contributions

I also contributed to the following publications which are not included in this thesis. As a member of the FLASH team and with expertise on THz streaking, I conducted the experiments mentioned in the publications below along the first authors and PIs, and contributed to the final version of the manuscript.

- **Electronic decay of core-excited HCl molecules probed by THz streaking.**

  K. Wenig, M.Wieland, A.Baumann, S.Walther, A.Dimitriou, M. J.Prandolini, O.Schepp, I.Bermúdez Macias, M.Sumfleth, N.Stojanovic, S.Düsterer, J.Rönsch-Schulenburg, E.Zapolnova, R.Pan, M.Drescher, and U.Frühling. Struct. Dyn.6, 034301 (2019).

- **THz streak camera performance for single-shot characterization of XUV pulses with complex temporal structures.**

  T. Oelze, O. Kulyk, B. Schütte, U. Frühling, E. Klimešová, B. Jagielski, L. Dittrich, M. Drescher, R. Pan, N. Stojanovic, V. Polovinkin, K. P. Khakurel, K. Muehlig, I. J. Bermúdez Macias, S. Düsterer, B. Faatz, J. Andreasson, M. Wieland, and M. Krikunova. Opt. Express 28, 20686 − 20703 (2020)

Contents

A mi madre, quien creyó en mi desde un principio.

1

Introduction

X-ray Free electron lasers (FELs) produce uniquely brilliant, transversally coherent and extremely short laser-like photon pulses, allowing research of matter on both atomic time and length scales. The first soft X-ray FEL in Hamburg (FLASH) started user experiments in 2005 [1] and was followed by the construction and operation of other soft and hard X-ray FEL sources world-wide such as LCLS [2], SCSS [3], SACLA [4], FERMI [5], European XFEL [6], SwissFEL [7] and PAL-XFEL [8], to name some.

X-ray FEL facilities have opened exciting new opportunities for the investigation of ultrafast processes in atoms, molecules, clusters and nanoparticles, in condensed matter and matter in extreme conditions, including non-linear spectroscopy and single-shot single particle imaging [9, 10, 11, 12, 13, 14, 15, 16, 17].

Currently, the majority of X-ray FELs are based on self-amplified spontaneous emission (SASE). This amplification process starts from shot noise in the electron beam, and the emitted photon pulse consists of individual, independent, temporally coherent intensity spikes with positions and peak heights changing from pulse to pulse [18, 19]. Therefore, all the radiation properties of a SASE FEL such as the photon energy, spectrum, arrival time and duration vary for each pulse. The knowledge of all these radiation parameters on a single-shot basis is essential for the evaluation of the experimental data. Tremendous effort has been made to develop techniques and diagnostic tools in order to determine the different fluctuating radiation parameters for every pulse in a non-invasive way. Particularly, various photon temporal characterization methods have been developed [20, 21, 22, 23], since precise knowledge of the arrival time and pulse duration is important in time-resolved pump-probe experiments where one pulse is used to initiate a reaction and a subsequent pulse is used to probe the system. For example, optical cross-correlation methods [24, 25] can be used as a temporal diagnostic tool, however these techniques are not feasible at VUV and soft X-ray wavelengths as a timing tool due to the short absorption lengths in solids.

Up to now, the THz streaking technique [26, 27] is the only method which has demonstrated the capability to measure pulse duration and arrival time in a single-shot basis and for the wide range of pulse lengths and wavelengths that soft-Xray SASE FELs can generate. Furthermore, the streaking experimental setup can be installed in an almost non-invasive way and can potentially match the high repetition rate of some FELs [28]. At FLASH, the proof-of-principle of the THz streaking method was successfully demonstrated [26, 27], where the FEL pulse photoionizes a gas target and creates photoelectrons which have the temporal information of the ionizing pulse. The energy of the released photoelectrons is then modified (streaked) by an external electro-magnetic field depending on their time of ejection. For the pulse duration range provided at FLASH (on the order of tens of femtoseconds), a THz field is used to streak the photoelectrons. To this end, a single-cycle THz field is produced using an optical laser. After the implementation of the THz streaking experiment at FLASH and initial studies on how to use it as a temporal diagnostic tool [29], it was decided to dedicate a beamline (FL21) in order to study and commission the setup.

In this work, the commissioning of a permanently installed THz streaking tool for the diagnostics of pulse duration and arrival time at FLASH is presented. A brief description of the generation of SASE FEL pulses as well as streaking spectroscopy theory is discussed in chapter 2. In chapter 3, the FLASH facility is shortly described, with special attention given to the FLASH2 experimental hall and the FL21 beamline, where the THz streaking setup is currently installed. Furthermore, a detailed characterization of the streaking chamber is reported in section 3.3. In chapter 4, a summary and overview of the scientific contributions derived from my PhD work which resulted in peer-reviewed publications are presented. This encompasses the profound investigation of the application range and accuracy of the streaking setup as well as a statistical study of the photon properties both experimentally and theoretically. A preview of the most recent measurements and analysis of pulse duration and arrival time with novel FEL operation modes are also reported. These results will be part of future publications. Finally, the results of theoretical studies of post-collision interaction (PCI) effects in THz-assisted Auger decay are shown. Preliminary results of experiments using the streaking chamber to study PCI are also discussed. The conclusions and future perspectives are found in chapter 5.

2
Theory

2.1   SASE FREE ELECTRON LASER PRINCIPLE

The majority of FELs worldwide rely on the Self Amplified Spontaneous Emission (SASE) process [19, 30, 31] to produce radiation. This type of radiation is generated by passing a relativistic electron beam through an undulator, which is a periodic arrangement of dipole magnets of alternating polarity. A planar undulator produces a magnetic field in the vertical y-direction whose strength in the propagating z-direction varies as:

$$B_y(z) = B_0 sin(\frac{2\pi}{\lambda_u}z), \tag{2.1}$$

where λ_u is the undulator period (which is the distance between two equal poles of magnets), and B_0 is the peak magnetic field on the undulator axis. When traversing the undulator, the relativistic electron bunch is deflected on a sinusoidal trajectory in the propagating direction due to the Lorentz force. The electron acceleration causes spontaneous emission of radiation at the resonant wavelength [32]:

$$\lambda_r = \frac{\lambda_u}{2\gamma^2}(1 + \frac{K^2}{2} + \gamma\varphi^2), \tag{2.2}$$

where γ is the Lorentz factor,

$$K = \frac{eB_0\lambda_u}{2\pi m_e c} \tag{2.3}$$

is the dimensionless undulator parameter and φ is the observation angle to the undulator z-axis. Equation 2.3 shows that the resulting radiation is related to the magnetic field strength in the undulator and the energy of the electrons moving through it. Therefore, the emitted radiation

can be tuned by changing the electron bunch energy or, in the case of variable gap undulators, by adjusting the magnetic field. The radiation emitted in the forward direction $\lambda_1 = \lambda_r(\varphi = 0) = \lambda_u/2\gamma^2(1 + K^2/2) = 2\pi c/\omega_r$, where ω_r is the fundamental undulator frequency, co-propagates with the electron beam and may exchange energy with the electrons. Steady energy transfer is achieved if the difference of the propagated distance within one undulator period between the electron bunch and the radiation is equal to the resonant wavelength. Since the wavelength that meets the resonance condition is the same as that generated in the undulator in the forward direction, the spontaneously emitted radiation at the beginning of the undulator can be used as the initial input to start the FEL process, known as SASE process. Depending on the relative phase
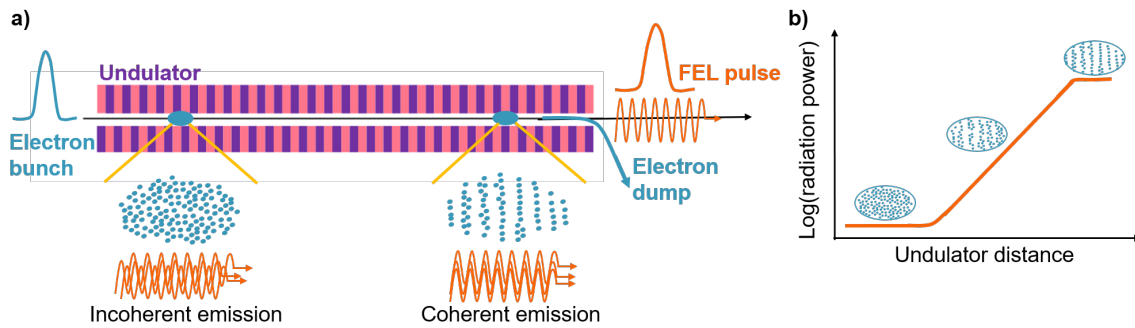

Figure 2.1: a) Schematic of a high-gain SASE free-electron laser, in which both the radiation power and the electron beam microbunching grow as a function of the undulator distance until saturation. b) Growth of the radiation power and evolution of the microbunching within the electron bunch as a function of the undulator distance. The microbunching process is illustrated at three different positions in the undulator.

of the electrons to the light wave, some of the electrons in the bunch will lose energy to the radiation while others will gain energy from it. If the interaction is continued over sufficient number of undulator periods, faster electrons (with higher energies) will catch up with slower electrons, and the electron beam will be periodically modulated in energy at the resonant wavelength λ_1 of the co-propagating radiation. As the beam propagates further in the undulator, the energy modulation results in a spatial modulation of the electron beam density at λ_1. This is the so-called "micro-bunching" shown in figure 2.1, where the electrons in each microbunch emit radiation in phase. The more the electron bunch propagates through the undulator, the more the emitted radiation increases, since it adds up coherently while the electron bunch loses energy, leading to an exponential growth and eventual saturation of the radiation power. For the described geometry, the resulting radiation is linearly polarized in the horizontal direction, perpendicular to both the magnetic field and the electron beam trajectory. Higher harmonic radiation, especially odd harmonics, also exist with reduced intensity [33].

The behavior of a SASE FEL in the one-dimensional (1D) limit can be well characterized by

the so-called FEL Pierce parameter ρ and the number of cooperating electrons N_c [34, 35]:

$$\rho = \left[\frac{\lambda_u^2 j_0 K^2 A_{JJ}^2}{16\pi I_A \gamma^3} \right]^{1/3} , \qquad N_c = I/(e\rho\omega_r) , \qquad (2.4)$$

where γ is the relativistic factor, j_0 is the beam current density, $I_A = mc^3/e \simeq 17$ kA, K is the rms undulator parameter, and λ_u is the undulator period. The coupling factor is $A_{JJ} = 1$ for a helical undulator, and $A_{JJ} = [J_0(Q) - J_1(Q)]$ with $Q = K^2/[2(1 + K^2)]$ for a planar undulator where J_0, J_1 are the Bessel functions. I is the electron bunch current and ω_r the frequency of the amplified wave, with $\omega_r/2\pi = c/\lambda_r$.

As explained earlier, the radiation power grows exponentially with the undulator distance z: $P(z) \propto exp(z/z_G)$, where the power gain length is [34]:

$$z_G \simeq \frac{\lambda_u}{4\pi\sqrt{3}\rho}. \qquad (2.5)$$

The exponential growth continues until the energy of the electron bunch is decreased to the point that the resonance condition is not fulfilled anymore, thus the FEL power achieves maximal saturation. Furthermore, the microbunching also reaches saturation, and the electrons in the microbunch start being accelerated by the light wave and gaining energy on average (the light wave loses energy). The effect of saturation in a high-gain FEL after passing the exponential growth regime is depicted on the right side of figure 2.1.

The saturation length is given by [36]:

$$z_{sat} \simeq \frac{\lambda_u}{4\pi\rho}\left(3 + \frac{ln(N_c)}{\sqrt{3}}\right). \qquad (2.6)$$

SASE FELs can have excellent transverse coherence, as the high-gain process selects a dominant fundamental mode. However, since the amplification process originates from fluctuations in the electron beam current, SASE FEL radiation has limited temporal coherence and exhibits shot-to-shot fluctuations in intensity. This gives rise to the importance of measuring the temporal properties for every pulse at a SASE FEL. Examples of simulated SASE FEL photon pulses can be found in figure 1 of A.2. The pulse is composed of individual intensity spikes, each with the duration of the coherence time τ_c [18]. At the saturation point τ_c^{sat} is given by [35]:

$$\tau_c^{sat} \simeq \frac{1}{\rho\omega_r}\sqrt{\frac{\pi ln(N_c)}{18}}, \qquad (2.7)$$

where ω_r is the resonance frequency. The coherence time is a measure of the temporal range over

which the electrons emit coherently and the shortest pulse duration accessible at a SASE FEL [37, 38, 39]. It grows at a rate of $\sqrt{z}$ in the exponential gain regime (also known as linear regime), reaches a maximum value just before saturation, and gradually drops down in the post-saturation regime [35, 36] (see dotted line in figure 2 of A.2).

2.1.1 STATISTICAL PROPERTIES OF SASE FEL RADIATION

The radiation from a SASE FEL operating in the linear regime holds properties of completely chaotic polarized light [35], and the probability distribution of the energy in the radiation E_r is a gamma-distribution [35, 36]:

$$p(E_r) = \frac{M^M}{\Gamma(M)} \left(\frac{E_r}{<E_r>}\right)^{M-1} \frac{1}{<E_r>} exp\left(-M\frac{E_r}{<E_r>}\right) \qquad (2.8)$$

where $\Gamma(M)$ is the Gamma function,

$$M = \left(\frac{<E_r>}{\sigma_{E_r}}\right)^2, \qquad (2.9)$$

and $\sigma_{E_r} = \sqrt{<(E_r - <E_r>)^2>}$ is the standard deviation of the radiation pulse energy.

The parameter M can be interpreted as the average number of "degrees of freedom" or "modes" (longitudinal and transverse) in the radiation pulse [36, 40, 41]. Furthermore, as demonstrated in reference [41], M can be linked to the dimensionless normalized electron pulse duration $\hat{\tau}_{el}$,

$$\hat{\tau}_{el} = \rho\omega_r\tau_{el}, \qquad (2.10)$$

where τ_{el} is the electron bunch pulse duration. There, it was shown that for $M > 2$, the number of modes M essentially equals the normalized electron pulse duration $\hat{\tau}_{el}$.

Using this information, it is possible to estimate the minimum rms radiation pulse duration at the end of the high-gain linear regime [41] (See also equation 8 in A.2):

$$\tau_{ph}^{min} \simeq \frac{M\lambda z_{sat}}{15c\lambda_u} \simeq \frac{M\tau_c^{sat}}{4}. \qquad (2.11)$$

Equation 2.11 allows a simple way to derive the minimum pulse duration by means of knowing the coherence time and number of radiation modes.

Streaking experiments have been widely used in the past decades to measure photon pulse duration [42, 43, 44]. The basic concept consists of mapping the temporal profile of the photon pulse onto an "easy-to-measure", energy distribution. This is achieved by creating an electron wavepacket, via photoemission, which has the same temporal profile as the ionizing photon pulse. The photoelectrons are accelerated depending on their time of release, by a laser field towards a detector which measures the time-of-flight of the electrons.
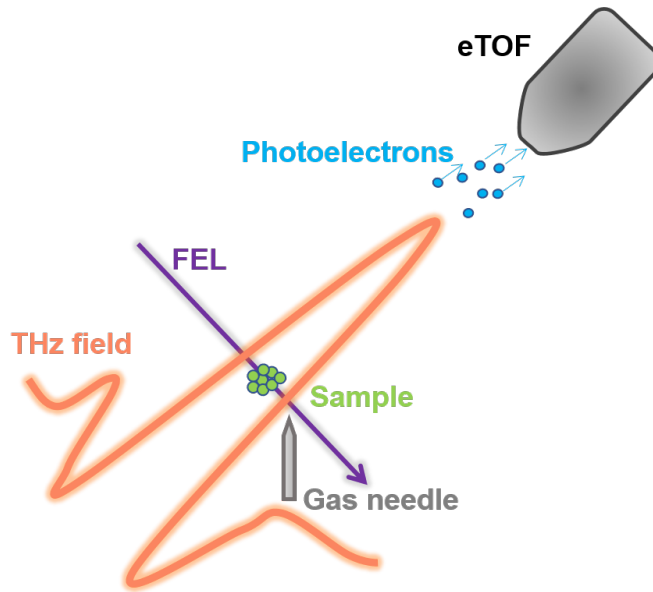

Figure 2.2: Geometric representation of the THz streaking experiment. A noble gas target is photoionized by an FEL, creating photoelectrons. Depending on the time delay between the linearly polarized THz field and the FEL pulse, the photoelectrons will interact with a different phase of the field which will accelerate or decelerate the photoelectrons. Finally, a time-of-flight spectrometer detects the ejected photoelectrons.

In recent years, an advanced streaking technique adapted from attosecond metrology [45, 46] has been developed and implemented at FELs. This technique [26, 27] uses the electromagnetic field of a laser pulse to streak the photoelectrons produced by the FEL. A condition for the field is that its oscillation period has to be significantly longer than the photon pulse to be measured. Due to the FLASH FEL pulse duration range of ~ 100 fs, the streaking field periods that fulfill this condition correspond to frequencies in the THz range.

In figure 2.2 a representation of the THz streaking principle is shown, where an XUV pulse

is focused into a noble gas target and collinearly overlapped in space and time with a linearly polarized THz field. The interaction between the XUV pulse and the gas creates photoelectrons via photoionization with the same temporal profile as the photon pulse. If this process occurs within one half-cycle of the THz field, the photoelectrons will be accelerated in the direction of the THz streaking field. The resultant change in momentum of the photoelectrons depends on the THz vector potential at the ionization time. A time-of-flight (TOF) spectrometer, placed along the polarization direction of both the XUV pulse and THz field, collects and measures the time-of-flight of the ejected photoelectrons.

Semi-classical description

Physically, the ionization of an atom by a femtosecond XUV pulse in the presence of a low-frequency strong laser field can be described as a two-step process, due to the difference in frequency between the XUV and the laser pulse. The first step is the photoionization, which generates an electron wavepacket in the continuum, and the second is the effect of the laser field on the energy spectrum of this wavepacket [47]. The semi-classical model uses classical mechanics to describe the second step [48, 49] and is briefly described below.

Consider an electron ejected from an atom to the continuum by an XUV pulse at a time t_0 with an initial kinetic energy of:

$$W_0 = \frac{m_e v_0^2}{2} = E_{xuv} - E_b, \tag{2.12}$$

where m_e is the electron mass, v_0 is the initial velocity, E_{xuv} is the energy of the absorbed photon and E_b is the binding energy of the atom. Assuming $E_b \ll E_{xuv}$, the influence of the ionic potential on the electron motion can be neglected as the electron rapidly escapes from the ion. Therefore, the motion of the freed electron will be driven by the strong laser pulse [50].

Consider a linearly polarized electric laser field

$$E_L(t) = E_0(t)cos(\omega_L t + \varphi_0), \tag{2.13}$$

where E_0 is the envelope of the laser pulse, ω_L is its angular frequency and φ_0 its phase at the moment of ionization. In this thesis, an electric laser field in the THz frequency range was used. The time-dependent momentum $\vec{p}(t)$ of the electron is given by [44, 50]:

$$\vec{p}(t) = e\vec{A}_L(t) + [m_e\vec{v_0} - e\vec{A}_L(t_0)], \tag{2.14}$$

with $\vec{A}_L(t)$ being the vector potential of the laser's electric field in the Coulomb gauge, such that $\vec{E}_L = -\partial \vec{A}_L/\partial t$ and is e the electron charge. Note that if there is no laser, equation 2.14 reduces to the motion of the free photoelectron $m_e\vec{v_0}$. The first term on the right side describes the
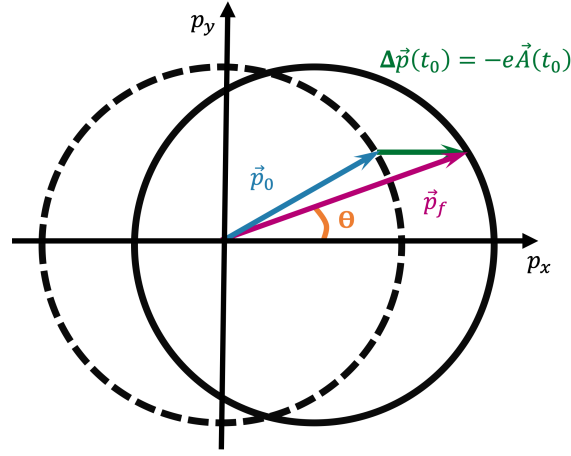
Figure 2.3: The dashed circle illustrates the initial photoelectron momentum distribution after ionization by the XUV pulse without laser field. The solid circle, translated by $-e\vec{A}_L(t_0)$, represents the momentum distribution under the influence of a streaking laser field polarized along the x-axis. Both, the electron kinetic energy and the direction of motion are altered. Figure adapted from [44].

electron quiver motion in the laser field and goes to zero as the laser pulse ends. The bracketed expression is the final momentum $p_f(t_0)$ of the electron, which is a constant and is determined by the initial momentum at the time of ionization $\vec{p}_0(t_0) = m_e\vec{v}_0$. The final momentum differs from the initial one by $e\vec{A}_L(t_0)$ and is measured experimentally after the laser pulse ends.

The momentum change $\Delta\vec{p}(t_0)$ after the end of the laser pulse is given by:

$$\Delta\vec{p}(t_0) = \vec{p}_f(t_0) - \vec{p}_0(t_0) = -e\vec{A}_L(t_0) \tag{2.15}$$

Considering photoelectrons with a fixed momentum amplitude $|\vec{p}|$ and uniform angular distribution, the effect of the laser field on the electron's momentum can be visualized by plotting $|\vec{p}|$ as a function of the observation angle θ in the x-y plane ($p_z = 0$) [44, 50, 51], as shown in figure 2.3. The final momentum of the photoelectrons in the absence of the laser field is independent of θ and the distribution is thus a circle of radius $\vec{p}_0(t_0)$ (dashed circle). In the presence of the laser field, for a given t_0, and assuming that the laser field $\vec{E}_L(t)$ is polarized in the $x-$direction, the distribution of the photoelectrons will remain a circle (solid circle) with the same radius but with its center translated by $-e\vec{A}_L(t_0)$ with respect to the dashed circle in the $x-$ direction. Therefore, as t_0 varies, this circle will oscillate along the polarization direction axis. This shows that besides changing the electron's final kinetic energy, the linearly polarized laser field deflects it from its initial propagation direction.

For a given observation angle θ and time of ionization t_0, one can determine the final momentum distribution $\vec{p}_f(t_0) = \vec{p}_0(t_0) + \Delta\vec{p}(t_0)$, and therefore calculate the final kinetic energy

$W_f = |\vec{p}_f|^2/(2m_e)$ for photoelectrons moving in the $x - y$ plane by solving the second-order polynomial equation $|\vec{p}_0(t_0)|^2 = |\vec{p}_f(t_0) - \Delta\vec{p}(t_0)|^2$:

$$|\vec{p}_f(t_0)|^2 - 2|\Delta\vec{p}(t_0)||\vec{p}_f(t_0)|cos\theta + |\Delta\vec{p}(t_0)|^2 - |\vec{p}_0(t_0)|^2 = 0. \qquad (2.16)$$

This leads, for a linearly polarized laser field and in the slowly-varying envelope approximation $(dE_0/dt \ll E_0\omega_L)$, to [44, 50]:

$$\begin{aligned} W_f(t_0) = W_0 &+ 2U_p(t_0)cos(2\theta)sin^2(\omega_L t_0 + \varphi_0) \\ &\pm cos\theta sin(\omega_L t_0 + \varphi_0)\sqrt{8U_p(t_0)W_0} \\ &\overline{\sqrt{1 - \frac{2U_p(t_0)}{W_0}sin^2\theta sin^2(\omega_L t_0 + \varphi_0)}}, \end{aligned} \qquad (2.17)$$

where the observation angle θ is the angle between $\vec{p}_f$ and the laser polarization direction, and $U_p(t_0)$ is the ponderomotive potential (cycle-averaged kinetic energy of a free electron oscillating in the electromagnetic field of the laser pulse) at time t_0. The latter is given by [50]:

$$U_p(t) = \frac{e^2 E_0^2(t)}{4m_e^2\omega_L^2}. \qquad (2.18)$$

For $U_p \ll W_0/2$, only the positive sign of equation 2.17 has a physical meaning. This equation shows how the energy change $W_f - W_0$ induced by the laser field is dependent on the ionization time t_0 and the observation angle θ.

For an observation angle perpendicular to the laser polarization direction $(\theta = \pi/2)$ where there is a maximum deflection, the final kinetic energy is given by:

$$W_{f_\perp}(t_0) = W_0 - 2U_p(t_0)sin^2(\omega_L t_0 + \varphi_0). \qquad (2.19)$$

At this observation angle, the laser field leads to a reduction of the kinetic energy of the photoelectrons with a periodic oscillation of double the laser frequency. This shift is negligible because $U_p \ll W_0/2$, and therefore the final kinetic energy measured is equal to the unperturbed initial energy $W_{f_\perp}(t_0) = W_0$.

At an observation angle along the polarization direction $(\theta = 0)$, the final kinetic energy is given by:

$$W_{f_\parallel}(t_0) = W_0 - 2U_p(t_0)sin^2(\omega_L t_0 + \varphi_0) + sin(\omega_L t_0 + \varphi_0)\sqrt{8U_p(t_0)W_0}. \qquad (2.20)$$

Here, the term in the middle can be neglected as in the case above. Taking this into account, the photoelectron detector for streaking experiments is usually placed along the laser polarization direction in order to have the largest energy shift effect. The measured kinetic energy change is therefore given by:

$$\Delta W_{\parallel}(t_0) = W_{f_{\parallel}} - W_0 \approx \sqrt{8 U_p(t_0) W_0} \sin(\omega_L t_0 + \varphi_0) \approx e\sqrt{\frac{2\omega_0}{m_e}} A_L(t_0). \qquad (2.21)$$

Note that around the zero crossing of the vector potential (when the argument $\omega_L t_0 + \varphi_0$ is small), the ionization time is projected onto the kinetic energy of the electrons. According to this model, the influence of the laser field depends on the time of ionization and leads to a periodic modulation of the kinetic energy of the photoelectrons ejected to the continuum by the XUV pulse. Furthermore, equation 2.21 shows that there is a linear dependence between the kinetic energy change of the photoelectrons and the vector potential of the laser field at their ionization time.

QUANTUM-MECHANICAL DESCRIPTION

The above formalism is valid for a point-like single electron. However, the released photoelectrons form a wavepacket, whose properties reflect the XUV pulse properties. At FELs, the XUV pulses have a spectral distribution. Therefore, the model has to be adapted to a distribution of electrons.

The effect of the streaking field on the initial time-momentum distribution $n_e(p_i, t)$ of the photoelectron's distribution is [51, 52]:

$$\sigma(p) = \int_{-\infty}^{\infty} n_e(p - eA(t), t)dt. \qquad (2.22)$$

Here, the width of the streaked photoelectron spectrum depends on the initial electron distribution, which depends on the XUV pulse properties. A quantum-mechanical description of atomic XUV photoionization in a laser field can be found for example, in references [44, 45, 46, 50]. This model uses the strong field approximation (SFA) [53] in addition to the single active electron approximation (where the ionization is described as a pure one-electron process in which all remaining non-ejected electrons act as frozen spectators). A comparison between the semi-classical and the quantum-mechanical treatment shows that both models are equivalent as long as the XUV pulse is significantly shorter than half the streaking field period.

The effect of the streaking field on an electron distribution with a finite temporal duration is briefly explained below.

The XUV spectrum in the presence of a linearly polarized electric field can be calculated quantum mechanically [44] and solved analytically in the special case of Fourier limited (also known as bandwidth-limited) XUV pulses with a Gaussian envelope

$$E_{XUV} = Ae^{-a(t-t_0)^2/2\sigma_{XUV}^2}, \tag{2.23}$$

where the full width at half maximum (FWHM) of the pulse duration is given as

$$\tau_{XUV} = 2\sqrt{ln2}\sigma_{XUV}. \tag{2.24}$$

For an observation angle along the polarization direction of the streaking field, the XUV spectrum has a Gaussian shape with a width determined by [29]:

$$\sigma_{streak} = \sqrt{\sigma_0^2 + s\sigma_{XUV}^2}, \tag{2.25}$$

where $s = \partial W_\parallel/\partial t$ is the streaking speed and σ_0 is the width of the pulse without the streaking field. In this thesis, σ_0 is termed "unstreaked" or "reference" width.
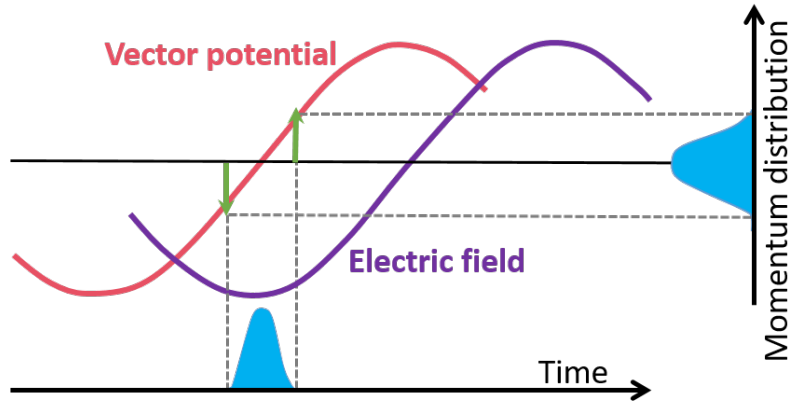

Figure 2.4: Streaking of a Fourier limited XUV pulse. The photoelectron distribution produced via photoionization by an XUV pulse is probed around the zero-crossing of the streaking vector potential. The photoelectrons emitted before and after the zero-crossing are decelerated and accelerated respectively by the streaking field. This results in a broader spectrum as compared to the field-free case.

Figure 2.4 shows the effect of the streaking field in the photoelectron distribution produced by a Fourier limited XUV pulse synchronized at the zero-crossing of the streaking vector potential. The electron distribution is a replica of the XUV pulse and thus has the same temporal

distribution. The momentum change of the photoelectrons depends on its time of ionization as they interact with a different phase of the streaking field - electrons produced before and after the zero-crossing of the vector potential are decelerated and accelerated respectively. Therefore, the width of the final momentum distribution is broader compared to the field free distribution. The broadening of the measured spectrum depends on the streaking speed s of the field, the pulse duration and bandwidth of the XUV pulse, as seen in equation 2.25.

In general, XUV pulses may have a chirp (time dependence of its instantaneous frequency) and this dependence is also present in the photoelectron distribution, resulting in a different behaviour of the streaked spectrum.

For the case of an XUV pulse with a linear chirp and a Gaussian envelope

$$E_{XUV} = \hat{E}_{XUV} cos(\omega t + ct^2),\qquad (2.26)$$

where $\hat{E}_{XUV}$ is the envelope of the pulse, ω is the central frequency of the XUV field and c is the linear chirp parameter, equation 2.25 becomes [54]:

$$\sigma_{streak} = \sqrt{\sigma_0^2 \pm \sigma_{XUV}^2(s^2 + 4cs)}.\qquad (2.27)$$

The sign $\pm$ depends on the slope of the vector potential. The sign is positive or negative for an observation direction parallel or antiparallel to the streaking field respectively. Therefore, for a linearly chirped XUV pulse, two measurements at opposite slopes of the vector potential are required to determine the duration of the pulse[54].

2.3 POST-COLLISION INTERACTION EFFECT.

The term Post-Collision Interaction (PCI) is used to describe the effects of the interaction of charged particles in the final state of the atomic collision process [55]. In particular, in the photoinduced Auger process, PCI is the interaction between the photoelectron, the Auger electron and the residual ion [56]. Here, the PCI effect distorts the shape of the Auger line in the spectrum and changes the mean energy. With the advent of time-resolved experiments to study atomic processes such as Auger decay, it was found that under certain conditions, PCI leads to a time-dependent Auger electron kinetic energy [57]. This temporal energy variation of the Auger spectrum was investigated experimentally by using the terahertz (THz) streaking technique described in the previous section, where atoms are ionized with an extreme-ultraviolet (XUV) pulse in the presence of a linearly polarized electric THz field. An accurate theoretical description of the THz-assisted photoinduced Auger process can be given by solving the time-dependent Schrödinger equation, where both the exciting XUV and streaking THz pulses are taken into account [58]. However, the long streaking THz pulse in comparison with the fast oscillations of the electronic wave functions makes a direct application of this method not feasible due to prohibitively long
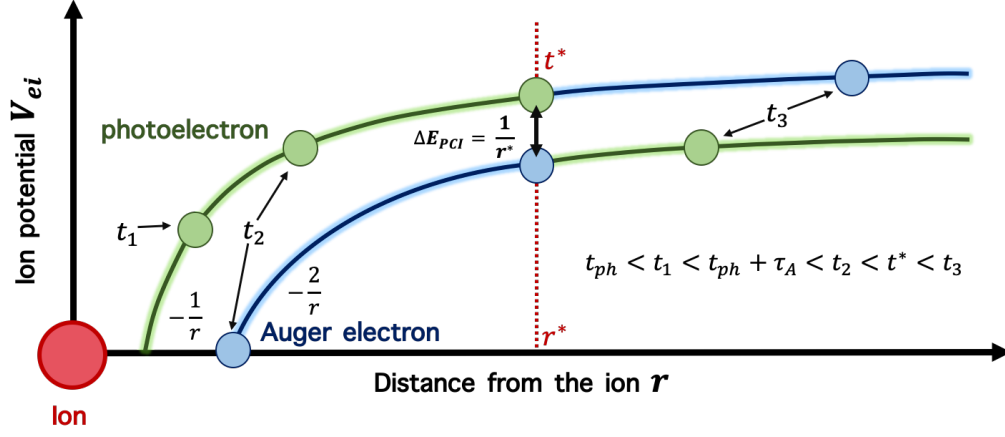
Figure 2.5: Scheme of the PCI effect. A photoelectron (emitted at t_{ph}) is overtaken by a faster Auger electron (emitted at $t_{ph} + \tau_A$) at the time t^* and distance r^* from the ion. The change of screening of the ion, results in an energy gain for the Auger electron and an energy loss for the photoelectron. Figure adapted from [57].

computation time. In reference [59], a new analytical semiclassical model was developed which incorporates both the streaking of photoelectrons in the presence of a THz field and the PCI effect. The model is based on the semi-classical description of the PCI effect (illustrated in figure 2.5): A slow photoelectron is overtaken by a fast Auger electron, causing a temporal change of the effective electron-ion interaction potential V_{ei} the two electrons experience. Therefore, when the Auger electron passes by the photoelectron at a distance r^* from the ion, the Auger electron gains (photoelectron loses) the energy $\Delta E_{PCI} = -1/r^* - (-2/r^*) = 1/r^* > 0$. Here, it is assumed that the energy exchange occurs instantaneously at t^* and the movement of both electrons is considered classically. Furthermore, this model predicts that the net amount of transferred energy depends on the distance from the ion - the closer the overtaking happens, the stronger is the effect.

This model was used for the calculations performed in A.3. Since a detailed explanation of the method is given in [57, 59] and A.3. Here, only a short description of the model and the most important equations are presented. Atomic units are used in the equations presented in this section.

Consider a photoelectron emitted at a time t_{ph} with momentum p_{ph} and an Auger electron released after the photoelectron at a time τ_A with a momentum $p_A > p_{ph}$ in the presence of a linearly polarized THz streaking field with vector potential $A_{THz}(t)$. Expanding in Taylor series the THz vector potential around the moment of the photoemission:

$$A_{THz}(\tau_A) = A_p + \dot{A}_p \tau_A + \vartheta(\tau_A^2) + \dots \tag{2.28}$$

15

where $A_p = A(t_{ph})$ and $\dot{A}_p = \frac{dA}{dt}(\tau_{ph})$ denotes the first time derivative of the vector potential. Considering the Auger electron spectra in two neighbouring zero-crossings of the vector potential ($A_p = 0$) and ignoring the higher order terms in 2.28, the energy shift for Auger electrons in the THz field is given by $p_A A(\tau_A) = p_A \dot{A}_p(\tau_A)$ and shows that the energy shift depends on the sign of the derivative $\dot{A}_p$.

For a positive derivative of the streaking electric field $\dot{A}_p > 0$, the PCI-distorted spectral line shapes of the Auger electron is given by [59]

$$f_+(\varepsilon) = \Gamma_4 \frac{k_+ - \varepsilon_-}{k_+} e^{-\Gamma_4(k_+ - \varepsilon_+)}, \qquad (2.29)$$

where $\Gamma_4 = |\alpha| \Gamma_A$ with $\alpha = (2 p_A \dot{A}_P)^{-1}$ and Γ_A is the Auger decay line-width (without THz field) so that the core-hole lifetime is Γ_A^{-1}.

For negative values of $\dot{A}_P < 0$, the Auger spectral line shape is:

$$f_-(\varepsilon) = 2\Gamma_4 e^{-\Gamma_4 \varepsilon_+} \left(\frac{\varepsilon_-}{k_-} \cosh \Gamma_4 k_- - \sinh \Gamma_4 k_- \right). \qquad (2.30)$$

In equations 2.29 and 2.30, $k_\pm = \sqrt{\varepsilon_-^2 \pm |\beta|}$, $\varepsilon_\pm = \varepsilon \pm \frac{\beta}{4} \delta r^*$ with $\beta = 4 p_A \dot{A}_P / p_r$. The parameters p_r and $\delta r*$ determine the classical distance from the ion at which the Auger electron overcomes the slower photoelectron $r^* = \tau_A p_r + \delta r^*$. Here $p_r = p_A p_{ph} / [p_A - p_{ph} + A(t_{ph}) - A(\tau_A)]$, and δr^* is a small correction to the initial distance of the two electrons from the ion.

Finally, due to the finite XUV pulse duration, the Auger spectrum generated by the XUV pulse in the THz field is given by the numerical convolution of the streaked energy spectrum $f_X(\hat{\varepsilon})$ with the PCI-distorted spectral line shapes $f_\pm(\varepsilon)$:

$$f_{X\pm}(\varepsilon) = \int_{-\infty}^{+\infty} d\hat{\varepsilon} f_X(\hat{\varepsilon}) f_\pm(\varepsilon - \hat{\varepsilon}). \qquad (2.31)$$

Where $f_X(\hat{\varepsilon}) = \frac{1}{\sqrt{\pi}\Gamma_X} \exp\left(-\frac{\hat{\varepsilon}^2}{\Gamma_X^2}\right)$, $\Gamma_X = p_A \dot{A}_P \tau_{XUV}$, and τ_{XUV} is the XUV pulse duration full-width at half-maximum (FWHM).

In [59] it was shown that as a result of the influence of PCI, the width of the Auger spectrum at $\dot{A}_P > 0$ (denoted as ω^+) is larger than at $\dot{A}_P < 0$ (denoted as ω^-) and the widths are equal if the PCI effect is negligible. Therefore, in A.3 PCI was characterized by the ratio of these widths

$$R_\omega = \omega^+ / \omega^-. \qquad (2.32)$$

<div style="text-align: right">

3

</div>

<div style="text-align: right">

Experiment

</div>

3.1 The Free electron LASer in Hamburg (FLASH)

FLASH is the world's first XUV and soft X-ray free-electron laser (FEL) facility and the only high repetition FEL in this wavelength regime so far. Figure 3.1 depicts the schematic layout of FLASH, which has been described in great detail in literature at its different development stages [60, 61, 62, 63]. Briefly, FLASH is composed of the laser injector based on a laser-driven normal conducting RF gun, which allows every 10 Hz the generation of up to 800 electron bunches with a repetition rate of up to 1 MHz and several ps duration, seven 12 m long TESLA-type superconducting accelerating modules that accelerate the electron bunches to energies from 0.35 to up to 1.25 GeV, bunch compressors that compresses the electron bunch longitudinally to $\sim 100\,\text{fs}$ duration, leading to a peak current range of $1 - 2.5\,\text{kA}$, and undulator structures, which are a series of permanent magnets. The FLASH1 undulator system consists of 6 undulators with a period of $\lambda_u = 27\,\text{mm}$, peak magnetic field of $B_0 = 0.47\,T$ and a fixed gap of 12 mm, whereas FLASH2 is equipped with 12 variable-gap undulators with a period of $\lambda_u = 31\,\text{mm}$ [64]. At the last stage, a dipole magnet deflects the electron beam into a dump, while the FEL radiation is sent to the experimental halls.

3.2 FLASH beamlines

The FLASH facility has two experimental halls, FLASH 1 and 2 [61, 62, 63, 65, 66], where two different experiments can be conducted in parallel. Up to 2021, FLASH1 has hosted five beamlines for users: BL1, BL2, BL3, PG1 and PG2 delivering short intense photon pulses from 4.2 to 50 nm. In addition, at the plane grating (PG) monochromator beamline [67, 68], there is a branch (PG0) that can be used in parallel to the PG beamlines. This configuration enables
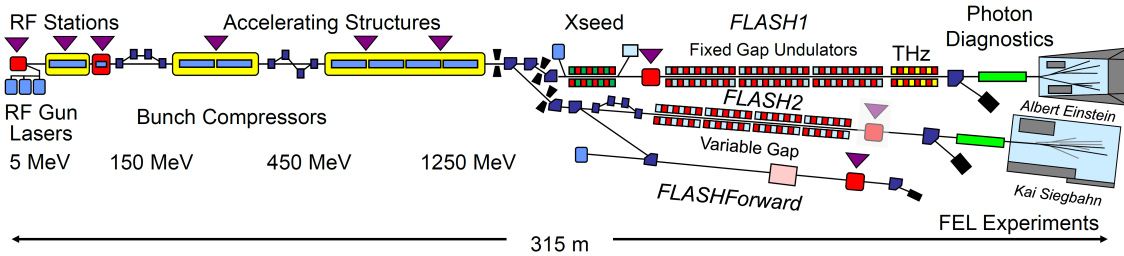
Figure 3.1: Schematic view of the Soft-Xray FEL FLASH in DESY. It shows the main components of an FEL, the electron bunch injector, acceleration cavities, undulator section to produce FEL radiation and the 2 experimental halls.

the utilization of the 0th diffraction order for experiments while the dispersed radiation is simultaneously used to measure the FEL spectrum. On the other hand, FLASH2 can be tuned to wavelengths from 4 to 90 nm and at present operates three beamlines: FL21, FL24 and FL26.

When the FEL radiation enters the experimental hall, it passes through a series of photon diagnostics [61] before the beam is sent to a specific beamline through ultra-high vacuum (UHV) pipelines. Currently, there are various photon diagnostic devices operating at FLASH. The pulse energy of the FEL radiation is measured on a single-shot basis at FLASH 1 and 2 using a gas monitor detector (GMD) [69, 70] with a precision of ±10 %. At FLASH 1 (BL beamline branch), the photon spectrum is determined using a pulse-resolving variable-line-spacing grating spectrometer (VLS) with a resolving power of 500 to 8000 depending on the FEL wavelength [71]. In addition, it is possible to measure the spectral distribution of pulses with a high resolution spectrometer using the PG beamline [67, 68]. At FLASH2, an online photoionization spectrometer (OPIS) [72, 73, 74] is available to measure the photon energy with an accuracy of 0.1 eV regardless of the FEL wavelength [74]. Furthermore, a mobile compact spectrometer [75, 76, 77], which can be set up at the endstation or behind user experiments of any beamline, can measure the spectrum with a spectral resolution in the 0.1–0.2% range [76]. At FLASH1, a transverse deflecting RF structure (TDS) [78] in combination with an energy "spectrometer" (which is composed of dipole magnets to disperse the electrons in the transverse direction and a detector screen) is used for electron bunch length, longitudinal phase-space and energy spread measurements [79]. The results are used to estimate the average photon pulse duration [41, 80]. On the other hand, at FLASH2, a Polarizable X-band (PolariX) TDS [81] and a kicker to deflect the beam onto an off-axis screen station are used for these type of measurements. Furthermore, the arrival time of the electron bunches with respect to the master optical clock is measured at FLASH 1 and 2 using the bunch arrival time monitor (BAM) with an accuracy of $\sim$ 10 fs rms [82, 83]. Experiments at FLASH1 with the THz-streaking setup showed that there is a good agreement between the BAM measurements and the arrival time fluctuations of the FEL pulses with respect to the pump-probe laser at the experimental end-station [29]. The results showed a very good correlation between
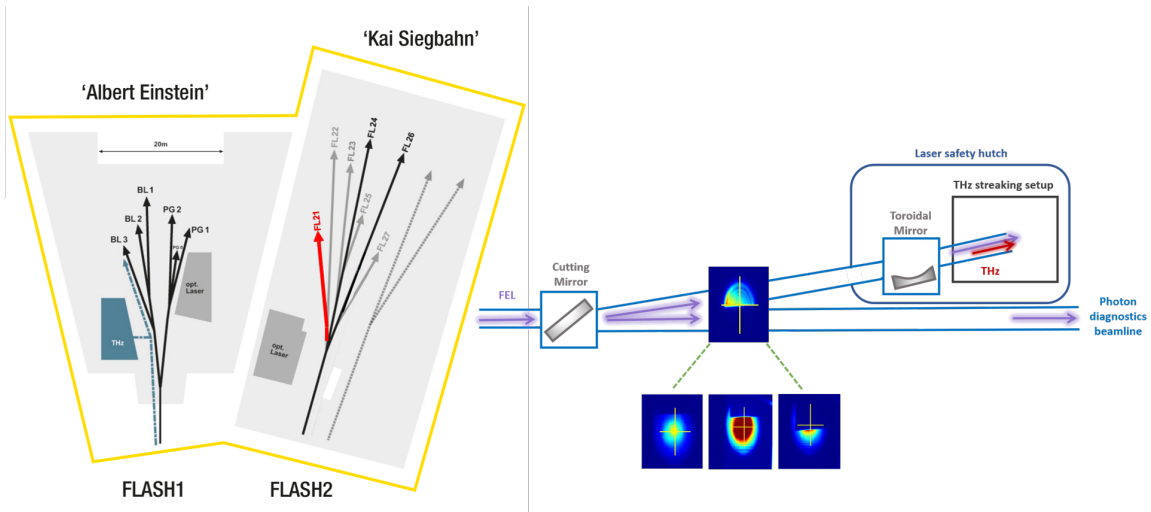
Figure 3.2: On the left side, FLASH 1 and 2 experimental halls with their respective beamlines. On the right side, an overview of the FL21 beamline at FLASH2, where the THz streaking experiment is currently installed. There is a cutting mirror that reflects the beam into the streaking beamline, where a 1030 nm laser generates THz radiation.

them with a correlation width of $\sim$ 15 fs, verifying the high precision of the BAM.

All these diagnostic tools are used together on a daily basis to provide feedback in order to fine tune the FEL parameters for user experiments as well as to evaluate and sort the experimental data. However, there is still no standard diagnostic tool for the direct measurement of photon pulse duration and arrival time. After a thorough experimental study of different temporal diagnostic techniques [20], where indirect and direct methods to measure pulse duration were compared, at FLASH it was decided that the THz streaking technique fulfills most of the requirements of a diagnostics tool for a SASE FEL, i.e. it can measure in a single-shot basis, it is wavelength independent and can be set up in an almost non-invasive way. Therefore, as a major effort to provide pulse duration and arrival time information, the FL21 beamline and a THz streaking setup was commissioned as part of this doctoral thesis.

3.2.1 FL21 BEAMLINE

The FL21 beamline is located in the FLASH2 experimental hall (see figure 3.2). After the photon beam enters FL21, there is a cutting mirror (CM) that can be moved in from top in order to reflect part of the beam to the THz streaking beamline. Images of the FEL beam taken with a fluorescence screen imaged by a CCD camera at different mirror positions are shown in figure 3.2. The covered part of the beam is reflected to the THz beamline and the remaining radiation continues along the straight pipeline downstream to the end of FL21. The FEL beam that propagates to

the THz streaking experiment is focused using a toroidal mirror (TM) with a 1.5 m focal distance before it enters the streaking interaction chamber. Both the CM and the TM are coated with gold and have an incidence angle of 86°. In addition, the photon beam that propagates through the straight beamline can be used for placing further diagnostic experiments like a compact spectrometer, wavefront sensor, etc, or an experiment that does not need a focused beam. This beamline was designed with the purpose of conducting THz streaking experiments in parallel to experiments at the end of the straight FL21 beamline and thus mimic and test the functionality of a temporal diagnostics experiment that measures reliably while keeping a minimum disturbance to the FEL beam.

3.3   Terahertz streaking setup

The THz streaking setup used for the experiments presented in this thesis is based on the experiments described in references [26, 27, 84, 85]. Figure 3.3 depicts the layout of the THz streaking setup, which was first installed and tested at the PG0 beamline in FLASH1 and later on moved to FLASH2, where it is currently part of the FL21 beamline. It consists of two parts: the THz production and transport and the UHV chamber.
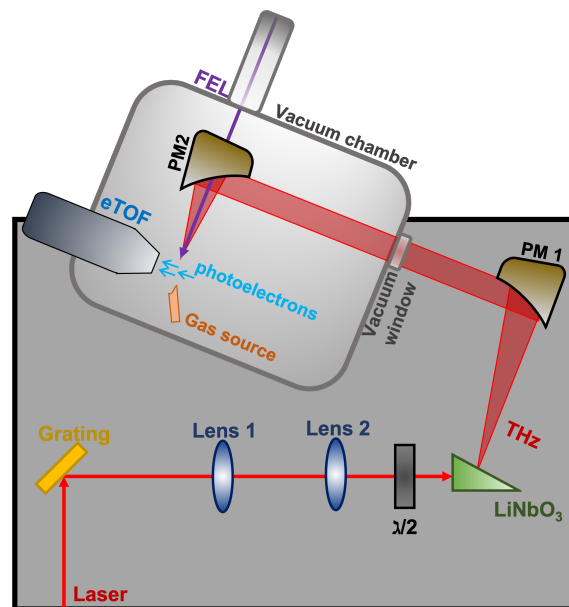

Figure 3.3: Schematic layout of the THz-streaking setup installed at the FL21 beamline of FLASH2. It consists of two parts, the THz production via tilted pulse-front in a $LiNbO_3$ crystal using an IR laser and the UHV chamber located above the optical table, where the FEL and THz beams are collinearly overlapped and focused in the interaction region.

1) The THz production and transport is achieved using a 1030 nm, $\sim$ 3.5 mJ, $\sim$ 1 ps laser
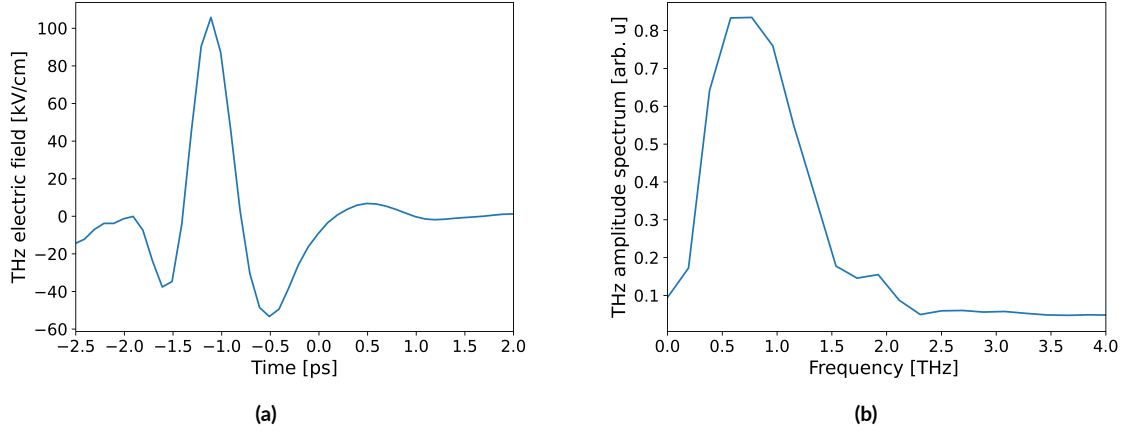
(a) (b)

Figure 3.4: (a) Electric field in the interaction region measured by THz streaking at the FL21 beamline. The measured photo-electron's kinetic energy is used to deduce the THz vector potential by employing equation 2.21 as described in section 2.2. The THz electric field is calculated by integrating the vector potential. The electric field strength estimated was ~ 150 kV/cm. (b) Spectrum of the electric field calculated by a Fourier transform. The maximum of the spectrum is at ~ 0.7 THz.

at FL21 (800 nm, 6.5 mJ, 80 fs at PG0 [29]), both operating with a 10 Hz repetition rate. The pulse-front of the IR laser pulse is tilted by a diffractive grating 1500 grooves mm^{-1} (2000 grooves mm^{-1} at PG0) and imaged using $4f$ two lenses telescope with a focal length of $f_1 = 200$ mm and $f_2 = 125$ mm ($f_1 = 150$ mm and $f_2 = 75$ mm at PG0) onto the LiNbO_3 crystal that creates THz radiation by satisfying the phase-matching condition for optical rectification [86, 87, 88].

A single-cycle THz pulse is produced with a slope of ~ 600 fs (see figure 3.4), centered at 0.7 THz, with an energy of $\sim 3.5\,\mu$J and electric field strength of up to 150 kV/cm at FL21 (0.6 THz, energy of $10 - 15\,\mu$J and electric field strength of up to 300 kV/cm at PG0 [29]).

The resulting THz beam is linearly polarized in the vertical direction and transported to the interaction chamber located above the THz production optical table. First, a flat gold coated mirror (M1) reflects the THz beam into a parabolic mirror (PM1) that collimates the beam, which together with a second mirror (M2) form a periscope in order to rotate the polarization into the horizontal direction and transport the beam upwards. The linearly polarized collimated THz beam enters the chamber through a Zeonex 480 vacuum window with 5 mm thickness (50 mm diameter clear aperture).

2) The UHV chamber (Cube 250 CF) is mounted on a three-axis movable support structure. It is equipped with a parabolic mirror (PM2) with a focal distance of 101.6 mm that focuses the THz beam and serves to collinearly overlap the THz and FEL beams in the interaction region, the latter passing through a 3 mm central hole in PM2. A gas needle that can be moved in the x-y-z-direction, introduces gas into the interaction region. A commercial electron time-of-flight (eTOF) spectrometer Kaesdorf ETF11, is installed on a three-axis manipulator to optimize the

21

position of the eTOF with respect to the interaction region.

The following subsections discuss the calibration and characterization of the THz streaking setup, including the eTOF, space charge effects and the possible effects of the cutting mirror (described in 3.2.1) on the FEL pulse duration.

3.3.1   THE ELECTRON TIME OF FLIGHT DETECTOR

The eTOF consists of a grounded field-free drift tube with a conical entrance aperture, shielded by μ−metal. The spectrometer is optimized for a distance of 3 mm between the interaction region and the entrance cone. Situated after the aperture, there is a lens which collimates the electron beam by applying voltages from 0 to up to +3000 volts. Negative voltages down to a minimum of −500 and positive, up to a maximum of +500 volts can be applied to the drift tube, in order to decelerate (retard) or accelerate high or low-energy electrons, respectively. At the end of the driftube there is a micro-channel plate (MCP) which detects the photoelectrons, where a voltage of up to +2300 volts can be applied. The output current of the MCP is then converted into a digital signal by an analog to digital converter (ADC), ADQ412 by Teledyne SP Devices with 4 Gsample/s and 12 bit dynamic range, and recorded in the FLASH data acquisition (DAQ) system. The acceptance angle of the spectrometer is on the order of 45° if the interaction zone is smaller than 200 μm (see figures 2 and 10 in A.1).

Simulations with SIMION using a model of the geometry of the spectrometer were performed in order to understand the photoelectrons' trajectories along the eTOF. SIMION is an electrostatics and particle optics simulation suite widely used for designing spectrometer components and lens systems such as eTOF detectors. It calculates electrostatic fields and the trajectories of charged particles through those fields of a given electrode configuration. Figure 3.5 shows an ex-
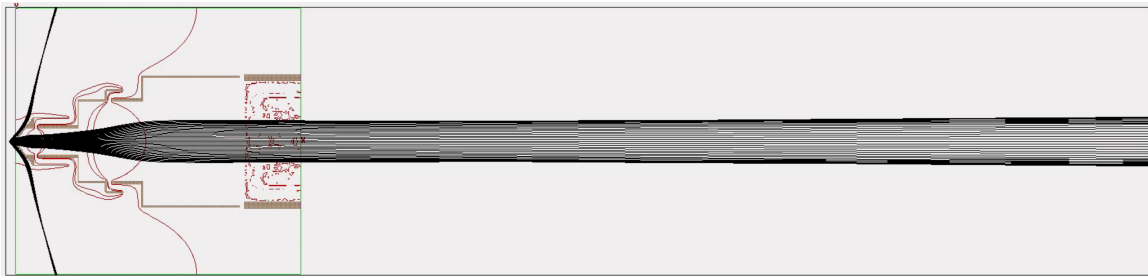

Figure 3.5: SIMION screenshot of electron trajectories in the eTOF spectrometer. The electrons (black lines) enter the eTOF on the left side and arrive to the MCP detector at the end of the right side. The photoelectrons' kinetic energy was set to 64 eV, the lens voltage to 430 V and the retardation voltage to 30 V.

ample of 100 photoelectrons' trajectories (shown as black lines) along the eTOF. The simulation was done for a photoelectron's energy of 64 eV, lens voltage of 430 V and a retardation voltage
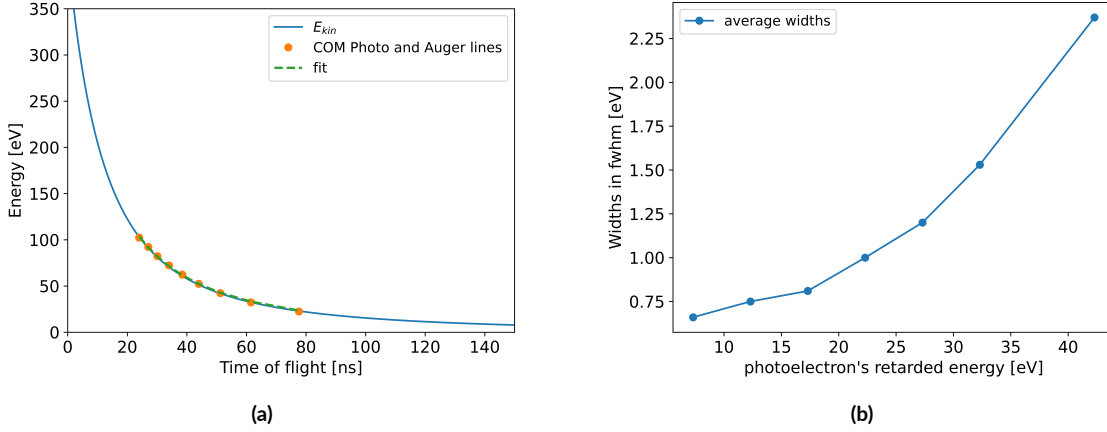
Figure 3.6: (a) Relation between the photoelectron's time of flight and its kinetic energy. The experimental values measured with the eTOF (points) were fitted using equation 3.1 in order to obtain the calibration parameters. The fit curve is shown as a dashed line. For these measurements the FEL was set to an energy of 126 eV and there was no retardation voltage in the drift tube. (b) Average widths of the measured photolines in FWHM as a function of the photoelectron's remaining energy (after being decelerated with the retardation voltage). A retarded energy of $\sim$ 10 eV results in the best resolution. For these measurements the FEL was set to an energy of 62 eV.

in the drift tube of 30 V. In an experiment, one has to adjust the lens and retardation voltages depending on the photoelectron's energy in order to produce a "collimated" beam of photoelectrons travelling through the eTOF as the one depicted in figure 3.5.

In order to experimentally calibrate the eTOF, neon 2p and 2s photoemission, as well as xenon Auger unstreaked spectra (without the external THz field) were taken at a fixed FEL photon energy.

Given a measured time-of-flight Δt and a flight path of length L, the kinetic energy of a free electron can be calculated by:

$$E_{kin} = \frac{1}{2} m_e{}^2 \frac{L^2}{\Delta t^2}, \qquad (3.1)$$

where m_e is the electron mass. Equation 3.1 can be used to map the time of flight of photoelectrons travelling through the eTOF drift tube into kinetic energy.

Figure 3.6 (a) shows the experimental average time-of-flight values over hundreds of shots for neon 2p and 2s photoemission lines and xenon Auger spectra for an FEL energy of 126 eV (9.8 nm) with no retardation voltage in the drift tube (0 V). These data points were fitted with the time to energy equation 3.1 in order to extract the fit parameters: t_0, (from $\Delta t : t - t_0$) the temporal offset between the instant of ionization and the data acquisition starting point and L, the effective time-of-flight path length. With those parameters, one can calculate the kinetic energy of any photoelectron that passes through the eTOF as a function of its time-of-light. This type of

energy calibration was done for various retardation voltages which resulted in similar calibration parameters.

The time-of-flight resolution of the photolines measured by the eTOF can be improved by changing the retardation voltages of the drift tube, depending on the photoelectron's kinetic energy (FEL energy). Usually, for streaking experiments, one has to find the best suited retardation voltage according to the FEL energy that one is working with. Figure 3.6 (b) shows the widths of unstreaked photoemission lines in FWHM as a function of the photoelectron's retarded energy. For an FEL wavelength of 20 nm (62 eV), a neon 2p photoelectron's remaining energy of ~ 10 eV results in a better-resolved breadth of the spectrum than with no retardation (~ 40 eV) due to the longer flying time of the photoelectrons caused by the deceleration voltage. However, relatively high retardation voltages compared to the photoelectron's energy can lead to background noise, since the same number of electrons is distributed over more samples in the ADC.

Similar measurements were performed at different FEL wavelengths and it was concluded that for the standard FLASH2 wavelengths ($\sim 4 - 40$ nm), the best retardation in the drift tube is the one that leaves the photoelectrons with a remaining kinetic energy of around 30 eV. With this setup, there is a compromise between a well resolved photoline and low background noise present in the signal.

3.3.2 SPACE-CHARGE EFFECTS

Space-charge effects in the interaction region, caused by the high FEL radiation intensity, could lead to shifts and broadening of the photoelectron spectrum depending on the FEL energy, modifying the eTOF measurements in an undefined way. During the photoionization process, the accumulated positive charge of the ions can decelerate the photoelectrons, leading to an additional broadening of the photoline. There are different variables that can be changed in the streaking experiment to prevent from space-charge effects, such as the amount of sample gas in the interaction chamber (gas pressure) and the FEL intensity. In order to understand the influence of these variables and successfully avoid these unwanted effects, measurements of the unstreaked photoelectron spectrum were done, varying the type of filters (FEL intensity) upstream the experimental chamber as well as the target gas pressure at a fixed FEL energy.

Figure 3.7 shows single-shot measurements of the widths of the 2p neon unstreaked photoline (σ_0 from equation 2.25) at an FEL energy of 64 eV (20 nm) for different FEL intensities. The FWHM of the photolines are plotted against the amplitude of the signal. The pulse widths stay almost constant until a threshold value (~ 1500 counts), where the widths start broadening linearly. After ~ 2000 counts the broadening becomes exponential, where space-charge effects are fully present. It is clear that lowering the FEL intensity using filters prevents from space-charge (see brown and purple points of figure 3.7), but the amplitude of the signal is not as high. A low-amplitude signal increases the signal-to-noise ratio which leads to statistical errors. In the experiments, therefore, it is important to compromise between these 2 parameters by having the
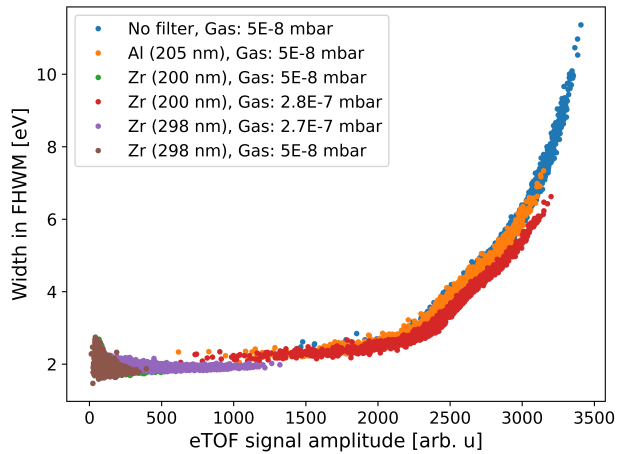
Figure 3.7: Correlation between the widths in FWHM of the unstreaked pulses and the amplitude of the detected signal. Space-charge effects emerge at around 2000 counts and develop differently depending on the filter used or the pressure in the interaction chamber. The number next to the element in the caption corresponds to the thickness of the filter in nm. The transmission values at the measured FEL wavelength (20 nm) are the following: Al (205 nm): 0.63, Zr (200 nm): 0.05, Zr (298 nm): 0.01.

highest signal possible without the presence of space-charge ($\sim$ 2000 counts from figure 3.7). Furthermore, the number of electrons calculated in the signal was on the order of hundreds of electrons in a single-shot measurement. It is relevant to mention that these results are only valid for the specific amplifier, MCP voltage and ADC used during the experiment when measuring the 2p neon photoline, and that they may vary if any of these variables change. However, these results were important to understand how space-charge works in the streaking experiment and to develop an analysis tool that is used onsite during the experiment in order to avoid space-charge.

3.3.3 Towards a minimal invasive temporal diagnostics tool

The aim of the THz streaking pulse duration and arrival time measurements is to perform the diagnostic experiments in parallel to the users experiments, while disturbing the FEL beam as little as possible. The FL21 beamline described in section 3.2.1 was designed to fulfill these requirements in a smaller scale, in order to commission the THz streaking chamber. Since streaking experiments do not need a high FEL intensity ($\sim 1\,\mu$J is enough to measure pulse duration) and usually filters are used to decrease the FEL energy, then having a small fraction of the beam might be sufficient to measure with THz streaking. The question to answer is: is the FEL pulse duration affected when only part of the beam is reflected into the streaking experiment?. This is important to know since the photon pulse duration may vary over the spatial distribution of the pulse due to the presence of higher order spatial modes [89]. However this question is not straightforward to

predict theoretically. The question was addressed experimentally by performing measurements of pulse duration at different cutting mirror positions (see figure 3.8) for different FEL settings.
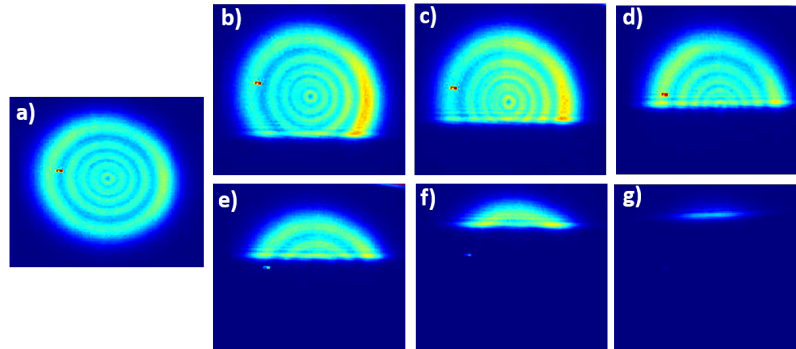

Figure 3.8: Images of the FEL beam profile sent to the streaking beamline for different cutting mirror positions. a) All the mirror is in the beam, therefore 100% of the FEL beam is reflected to the streaking beamline (no beam is sent to the straight beamline). b) $\sim 80\%$ of the beam is reflected to the streaking beamline and $\sim 20\%$ continues to the straight FL21 beamline. c), d), e), f) and g) correspond to $\sim 70\%, \sim 50\%, \sim 30\%, \sim 15\%$ and $\sim 5\%$ of the beam being reflected to the streaking beamline, respectively. The diffraction rings observed in the images result from an upstream aperture.
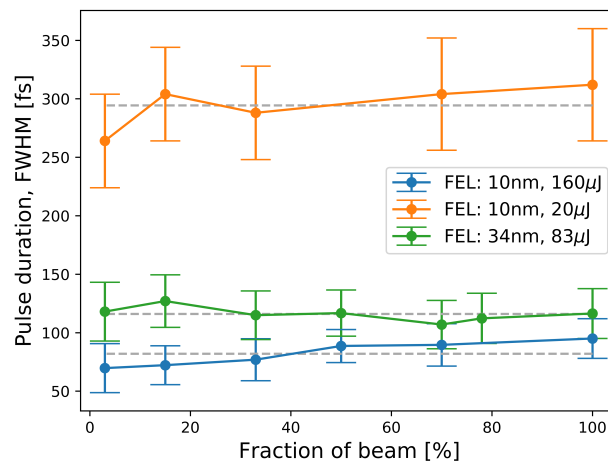
Figure 3.9: Average pulse duration measurements over $\sim$3000 shots at different mirror positions for different FEL settings. The bar in each point indicates the distribution of the measurement. The dotted line depicts the average value of all measurements for a fixed FEL setting.

Figure 3.9 displays the results of the average pulse duration over $\sim$ 3000 pulses when using different portions of the beam. The FEL pulse energy was kept constant for all measurements

(mirror positions) by adjusting the FEL filter in order to obtain the same signal level. The bars in figure 3.9 indicate the distribution of each measurement. The results show that when less than 3% of the beam is used for the experiment, there is a small apparent decrease in the pulse duration. Nevertheless, all the measurements agree with the average pulse duration of all the results (shown as a dotted line in figure 3.9). These results strongly indicate that the THz streaking beamline can measure pulse duration using only $\sim 3\%$ of the total FEL beam, making simultaneous measurements with users experiments feasible.

4

Overview of scientific contributions

This chapter is intended to give a general overview of the scientific contributions resulting from the work of this cumulative thesis. A more detailed explanation can be found in the corresponding publications provided in Appendix A. The publications are referred to as A.1, A.2, A.3 and A.4 in the text.

4.1 Single-shot pulse duration measurements at FLASH, towards a temporal diagnostics tool

As mentioned in chapter 3.1, FLASH produces photon pulses through the SASE process, and therefore every pulse is different from one another. Thus arises a very important task: to reliably measure all the photon properties of each pulse delivered to users. Currently, there are various photon diagnostics operating at FLASH. However, so far there is no direct photon pulse duration diagnostic tool available which can measure on a single-shot basis and at the high repetition rate of FLASH. The streaking technique described in section 2.2, is a powerful method that has proven to measure pulse duration and arrival time for every photon pulse. Previous proof-of-principle experiments performed at SASE FELs [26, 27, 85, 84] demonstrated that THz streaking can be used to characterize the temporal properties of the photon pulses. Furthermore, compared to other direct or indirect photon pulse duration measurement techniques [20], THz streaking is able to measure in a non-invasive way, for every pulse and, potentially, at the high repetition rate of some SASE FELs. Therefore it is a very promising candidate to be used as a temporal diagnostics tool at SASE FEL facilities such as FLASH.

The main goal of this thesis was to commission a THz streaking setup to study the technique in more detail and potentially become the temporal diagnostics tool for tuning the FEL as well as for users. In order to explore the applicability of the technique, the wide range of pulse duration

that FLASH can produce (from sub 10 fs to $\sim$ 350 fs) at different wavelengths was measured and investigated using the THz streaking setup described in section 3.3. The thorough study, published in A.1, showed an accuracy of $\pm 20\%$ including the various possible error sources: SASE fluctuations, Gouy phase broadening, eTOF spectrometer resolution and acceptance angle, signal-to-noise ratio (SNR) and the non-linearities of the THz vector potential. In addition to the experimental analysis, simulations of the streaking mechanism were performed using a novel and numerically fast approach for FEL pulse retrieval [90]. The method is based on a quantum mechanical approach within the strong-field approximation (SFA) and allows the reconstruction of linearly polarized FEL pulses from streaked photoelectron spectra, taking into account the angular distribution of the photoelectrons as well as the shape of the vector potential of the streaking field (see figure 2 in A.1). Furthermore, the limits of the technique were tested and analyzed. For the upper limit, long pulses that are as long as the slope of the THz streaking vector potential were measured. In such cases, the broadening due to streaking is so strong that one can obtain information of the pulse shape. In this case, the pulse shape is a convolution of the reference line and the actual FEL shape and it was retrieved using the previously mentioned method (see figure 7 in A.1). For the other cases (pulses shorter than half the slope of the vector potential), a Gaussian distribution is assumed as the streaked FEL shape. To investigate the lower limit, FLASH was operated in the single-spike mode [37, 38], and for the short wavelengths used, an average pulse duration of $\sim$ 10 fs was expected from spectral measurements. The THz field strength produced with the setup described in section 3.3 was $\sim$ 300 kV/cm and not sufficient to resolve the FEL pulses, since the detailed analysis resulted in error bars of $\pm 100\%$ (see figure 10 in A.1). Finally, it was concluded that the commissioned setup can measure single-shot-pulse duration for the range of 30 to 150 fs with an accuracy of $\pm 20\%$, which is well suited for the standard operation at FLASH.

4.1.1 TWO-COLOR OPERATION MODE AT FLASH2

Using the THz streaking setup, measurements of pulse duration and arrival time were conducted for the two-color operation mode of FLASH2, where two XUV pulses with two different wavelengths are produced by the same electron bunch. Such scheme can be achieved by different methods [63, 91, 92] and enables XUV-XUV pump-probe experiments with different (XUV) colors at the facility. For the results shown here, FLASH2 was set to the two-color operation as described in reference [92]. Briefly, in order to create the two wavelengths from the same electron bunch, FLASH2 uses the advantage that the gap between each pair of undulators can be adjusted independently. The odd pairs of undulators are tuned to λ_1 and the even pairs to λ_2.

In figure 4.1 (a), kinetic energy spectra of 2p neon photoelectrons created by the two FEL wavelengths (λ_1: 15 nm (83 eV) and λ_2: 18.7 nm (66 eV)) in the presence of the THz field as a function of the time delay between the FEL and THz pulse are shown. The spectra were measured simultaneously using the eTOF detector. The single-shot measurements show that the duration of the
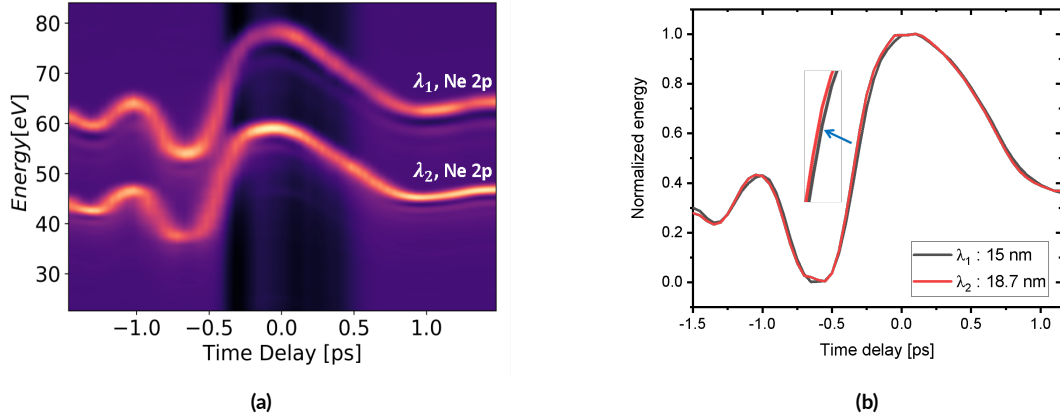
Figure 4.1: (a) Kinetic energy of neon 2p photoelectrons in the presence of the THz field as a function of the time delay between the FEL and THz pulses. The spectra were taken simultaneously for the two colors delivered at FLASH2 (λ_1: 83 eV and λ_2: 66 eV). (b) Streaking traces of the two colors normalized to their maximum. It reveals that the relative average arrival time between the two photoelectrons is shifted by ~ 15 fs.

pulses with higher energy is slightly shorter than those with lower energy (longer wavelength). The average pulse durations measured were 110 ± 20 fs for λ_1 and 120 ± 20 fs for λ_2. In addition, one can derive the relative arrival time between the two pulses averaging over thousands of FEL pulses. Having a closer look at the THz streaking vector potential taken from the scan (figure 4.1 (a)), one can observe that the pulses produced at longer wavelengths arrive on average slightly earlier than the ones at shorter wavelengths. This arrival time difference is depicted in figure 4.1 (b).

Furthermore, since both photon pulses are created by the same electron bunch, it is possible to determine the arrival time jitter between the two colors (pulses), which is induced only by the SASE process (see section 4.3 of A.2). In paper A.2 (described in the following section), the arrival time fluctuations of SASE pulses were studied theoretically, where a scaling law was derived from the simulations (equation 4.1). However, the experimental results in A.2 did not have sufficient resolution in order to verify the model since in those measurements, additional jitter contributions e.g. due to the synchronization with the optical laser were present. The measurements described here (section 4.1.1) enable the direct measurement of SASE fluctuations in the arrival time and the results verify the theoretical model derived in A.2 (see also figure 8 in A.2). For the present results, a jitter of 19 fs rms was measured. This important result shows that for XUV-XUV pump-probe experiments using the described two-color operation mode, one has to take into account the jitter due to SASE as it can be significant, especially in comparison to experiments using e.g. a split-and-delay unit (SDU), which has a resolution of < 1 fs [93]. The

above results are the first single-shot pulse duration measurements ever taken at a SASE FEL with such two-color operation mode and demonstrate the wide application range, capability and possibilities of the THz streaking setup. A publication discussing these results is currently being prepared.

4.2 STATISTICAL ANALYSIS OF SASE FEL RADIATION PARAMETERS

An important result of this thesis is the thorough study of the different fluctuating SASE FEL radiation parameters such as pulse length, arrival time, energy and spectral distribution, which were measured simultaneously on a single-shot basis. In A.2, it was analyzed how these four SASE pulse properties vary for every shot as well as on average for a wide pulse length range from $\sim$ 20 fs to up to $\sim$ 300 fs and various FEL wavelengths. The experimental results were compared to simulations of SASE pulses using two different approaches: employing the partial coherence method [94] and the FAST code [95].

The partial coherence method is an algorithm that generates pulse shapes in time and energy domain by filtering random electro-magnetic phases spectrally and temporally. This algorithm can be easily implemented in a few lines of code in contrast to the FAST algorithm, which is a complex three-dimensional, time-dependent SASE pulse simulation code. The results of the simulations were used to identify the fluctuations that occur only due to SASE and the ones resulting from other sources, which cannot be distinguished in the measurements. The analysis showed that on average, the major contribution to the fluctuations (at least 60%) in all the radiation parameters are primarily related to SASE, and depending on the parameter (energy, pulse duration, arrival time or spectral distribution), there is a varying contribution from the machine operation side (figures 6, 7 and 8 in A.2).

Furthermore, by analyzing the simulation results (figure 3 in A.2), it was deduced that the SASE fluctuations of the pulse duration and arrival time radiation parameters scale as $\frac{1}{\sqrt{M}}$, where M is the number of spectral modes (equation 2.8). The scaling law for the arrival time fluctuations σ_{ar} deduced was:

$$\frac{\sigma_{ar}}{\tau_{ph}} \simeq \frac{\alpha_{ar}}{\sqrt{M}}, \tag{4.1}$$

and for the pulse duration fluctuations σ_{ph}:

$$\frac{\sigma_{ph}}{\tau_{ph}} \simeq \frac{\alpha_{ph}}{\sqrt{M}}, \tag{4.2}$$

where τ_{ph} is the photon pulse duration, the scaling parameter α_{ar} ranges from $\sim$ 0.7 in the linear regime to $\sim$ 0.4 in saturation and α_{ph} from $\sim$ 0.4 to $\sim$ 0.2 respectively (see also equations 11 and 12 in A.2). This result enables a fast rough estimation of the magnitude of SASE fluctuations in pulse duration and arrival time. In addition, the result is useful for users, since it predicts

approximately how the fluctuations of the photon parameters depend on the pulse duration, without having to perform complex simulations that only experts can execute.

Furthermore, the mutual dependence between the different radiation parameters was investigated experimentally as well as theoretically. Using the large amounts of data taken for various FEL settings, it was shown that on average there is a linear relation between the pulse duration and number of spikes present in the spectral distribution N_{spect} (see figure 11 in A.2). These results have been predicted by theory [18] in the linear regime ($N_{spect} \sim 0.7M$, equation 9 in A.2), but were for the first time tested experimentally when the FEL is operated in saturation. It is also shown that the linear relation between these two radiation properties is only valid for the average over thousands of pulses, and not for single-shot values (figure 12 in A.2). This result means that the measurement of one single-shot spectrum cannot be used to calculate the pulse duration using the derived scaling law. On the other hand, the direct approach to Fourier-transform the spectrum in order to calculate the temporal profile is also not feasible due to the missing phase information.

Finally, it was shown experimentally and verified by simulations that the pulse energy, duration and number of spectral spikes fluctuate independently, since there was no correlation found between these properties (see figure 9 in A.2). This result emphasises the need for dedicated pulse-resolved diagnostics for each of the radiation parameters and enables SASE FEL users to freely sort their data by any of these radiation parameters without accidentally introducing systematic errors.

4.2.1 DEVELOPMENT OF THE RADIATION PROPERTIES DURING THE SASE AMPLIFICATION

As mentioned in 3.1, FLASH2 is equipped with 12 variable gap undulator segments, each of 2.5 m length and 31.4 mm period [64]. Using the streaking setup, the pulse duration was measured while varying the number of undulators contributing to the lasing. For this experiment, FLASH2 was set to 3 different wavelengths: 8, 12 and 16 nm, with an electron energy of 1 GeV and an electron bunch charge of 0.19 nC.

For each wavelength, the photon pulse duration and energy were measured for several undulator configurations. First, all 12 undulators were closed (thus contributing to the lasing), and one pair of undulators was systematically opened at a time, down to only 7 undulators closed (5 opened), where no measurable XUV pulse energy was detected anymore. Since only the downstream (closest to the experimental hall) undulators were opened, the trajectory in the first (lasing) undulators was kept constant. The energy of the photon pulses was simultaneously measured using the GMD.

The experimental results were compared to simulations performed by M. Yurkov using the FAST code. These types of energy gain curve simulations are well established and have been experimentally tested [41, 64, 96]. The simulations were performed for two different normalized electron bunch durations $\hat{\tau}_{el} = 8, 16$ (equation 2.10) and are presented in figure 4.2.

In order to compare the various measurements taken at different FEL wavelengths with each other and to the simulations, the experimental results were normalized to the parameters used in the simulations. As a first step, the number of undulators was scaled to the undulator length z, such that the onset of measurable SASE ($> 0.5\,\mu$J) coincides with the z-range in which the energy gain becomes visible in the simulated energy gain curve (solid line in figure 4.2). This determines the scaling for the undulator z-axis and fixes the saturation length z_{sat}. As a second step, the measured pulse energy was scaled such that the pulse energy at saturation length z_{sat} was defined as the saturation pulse energy E_{sat}.

The main parameters that were derived from the analysis of the gain curves (figure 4.2) are summarized in table 4.1. The normalized electron pulse duration $\hat{\tau}_{el}$ was calculated using the known coherence time at saturation τ_c^{sat} (from table 1 in A.2) and equation 2.10 for every measured wavelength. Since the FEL wavelengths (8, 12 and 16 nm) were produced at the same electron energy by changing the undulator gap, then the achievable saturation energy E_{sat} increases for longer wavelengths [1, 63, 64] as shown in table 4.1. The minimal pulse duration τ_{ph}^{min} increases slightly, while the needed number of undulators to reach saturation (z_{sat}) decreases.

Table 4.1: Relevant parameters to compare the experimental data to the theoretical model. The parameters were deduced from the analysis of the experimental data. The normalized electron pulse duration $\hat{\tau}_{el}$ was calculated for all measured wavelengths using equation 2.10 and the coherence time at saturation τ_c^{sat} (from [97] and table 1 in A.2).

Wavelength	$\hat{\tau}_{el}$ |M	E_{sat}	τ_c^{sat}(FWHM)	τ_{ph}^{min}(FWHM)	z_{sat}
8 nm	22	80 μJ	7 fs	80 fs	12
12 nm	16	140 μJ	9 fs	80 fs	10.5
16 nm	16	170 μJ	12 fs	100 fs	9.5

Figure 4.2 shows the experimental (points) and simulation (lines) results of pulse duration and pulse energy as a function of the undulator length z for different FEL wavelengths. The undulator coordinate z is normalized by the saturation length z_{sat}, meaning that values where $z/z_{sat} < 0.8$ are in the linear regime and values $z/z_{sat} = 1$ on the onset of saturation. The measured pulse energy is normalized to the saturation point E_{sat}. In order to normalize the pulse duration measurements, the experimental data was scaled to the minimum pulse duration τ_{ph}^{min} at $z/z_{sat} \sim 0.8$. The pulse energy increases exponentially until it reaches saturation at $z/z_{sat} = 1$ as expected, whereas the pulse duration grows at a lower rate. The maximum value of the photon energy and pulse duration are reached at different stages of z/z_{sat}: while the maximum pulse energy is achieved at $z/z_{sat} = 1$, for the pulse duration this point is reached at $z/z_{sat} = 1.2$. The shortest pulse duration for a fixed wavelength is at around 80% of saturation and it increases even after reaching saturation. These results are important, especially for tuning the FEL for users, since they show that operating in deep saturation by using all the undulators provides more pulse

energy - but on the other hand this will lengthen the photon pulse duration, which is undesirable for time-resolved experiments.
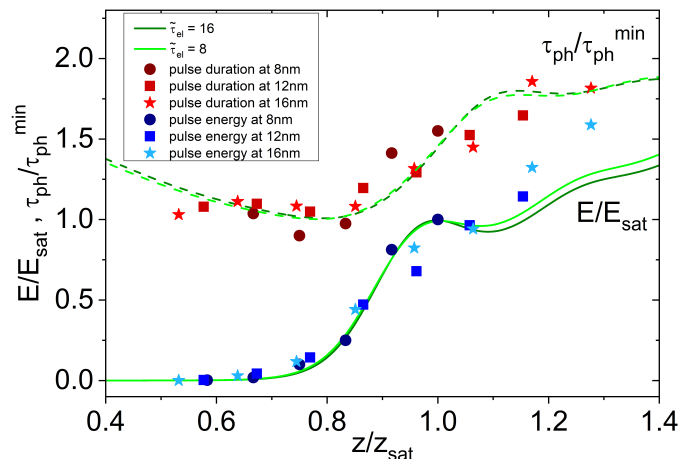

Figure 4.2: Evolution of the pulse duration and energy along the undulator. The undulator distance z is normalized by the saturation length z_{sat}. The pulse energy is normalized to the energy at the saturation point E_{sat} and the pulse duration to the minimum pulse duration τ_{ph}^{min}. The experimental results (shown as points) were measured at the FEL wavelengths of 8, 12 and 16 nm, which correspond to normalized electron bunch lengths $\hat{\tau}_{el}$ of 22, 16 and 16 respectively. The error bars of the pulse duration measurements are on the order of $\pm 20\,\%$ according to A.1 while for the energy are $\sim 10\,\%$. The simulations were performed for normalized electron pulse durations $\hat{\tau}_{el}$ of 8 and 16. The simulations for the photon energy are shown as solid lines and for the photon pulse duration as dashed lines.

Furthermore, figure 4.2 shows how well the experimental results (points) agree with the simulations (lines). This verifies experimentally the strong capability of the FAST code, which considers Gaussian electron bunch shapes to predict the actual behaviour of SASE photon pulse duration and energy. In reality, the electron bunch profile depends on the FEL setup and it is not necessarily Gaussian.

A similar plot can be found in A.2 (figure 2), where only the simulations are presented without the comparison to the experimental measurements. The results shown in figure 4.2 are part of a paper that is currently under preparation.

4.2.2 High harmonics

FLASH can produce FEL pulses in a wavelength range from $4 - 90$ nm. However, depending on the system under study, one might need shorter wavelengths. In SASE FELs, there are naturally occurring harmonics of the fundamental ($2\hbar\omega$, $3\hbar\omega$, ...$n\hbar\omega$), generated through non-linear energy modulations of the electron bunch [33, 98, 99].

The generation of higher harmonics is useful to extend the short-wavelength reach of SASE FEL facilities such as FLASH. Analogously to the two-color measurements, THz streaking can simultaneously measure the pulse duration of the fundamental wavelength as well as the first few non-linear harmonics produced. Figure 4.3 (a), shows the streaking spectra of the fundamental
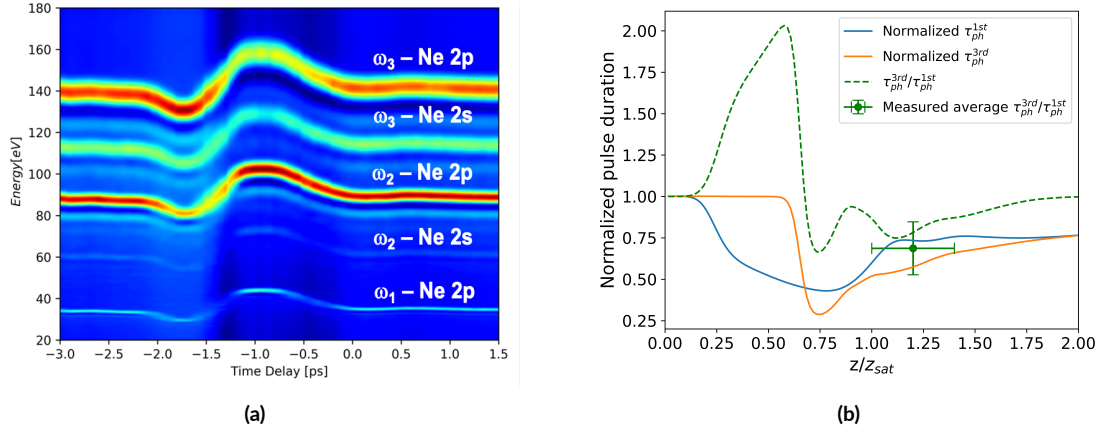

Figure 4.3: (a) Kinetic energy of 2p and 2s neon photoelectrons created by the fundamental, second and third harmonics in the presence of the THz field as a function of the time delay between the FEL and THz pulses. The fundamental FEL wavelength was set to 24 nm. (b) Simulations of the pulse duration of the fundamental (blue line) and third harmonic (orange line) normalized to the electron bunch length $\hat{\tau}_{el}$ as a function of the normalized undulator z/z_{sat} distance using the code FAST. The dashed line is the ratio between these two results. The dot is the ratio of the averaged pulse duration measured experimentally.

FEL wavelength (ω_1), the 2nd (ω_2) and 3rd (ω_3) harmonics for the 2s and 2p neon photolines. The FEL was set to a fundamental energy of 51 eV (24 nm). The analysis of the measurements resulted in an average pulse duration of $\tau_{ph}^{1st} = 170 \pm 21$ fs, $\tau_{ph}^{2nd} = 108 \pm 40$ fs and $\tau_{ph}^{3rd} = 85 \pm 40$ fs for the fundamental, 2nd and 3rd harmonics respectively. It is important to mention that the higher harmonics are about two orders of magnitude less intense compared to the fundamental [33] and thus filters have to be used to partially suppress the intensity of the fundamental wavelength. These results were compared to simulations performed by M.Yurkov using the code FAST. Figure 4.3 (b) shows the simulation of the photon pulse duration normalized to the electron bunch length ($\hat{\tau}_{el}$) as a function of the undulator distance z, where $z/z_{sat} = 1$ (from equation 2.6) denotes the onset of saturation. The simulation shows that τ_{ph}^{3rd} is almost constant in the linear regime ($z/z_{sat} < 0.8$) and longer than τ_{ph}^{1st}. Towards the end of the linear regime ($z/z_{sat} \sim 0.8$), τ_{ph}^{3rd} drops and becomes even shorter than τ_{ph}^{1st}. At the onset of saturation, both pulse durations increase but τ_{ph}^{3rd} stays shorter than τ_{ph}^{1st} until deep saturation is reached. This difference in pulse duration was also present in the measurements as shown earlier. Since the spectral distribution of the pulses was not measured for this experiment and the photon pulse duration was measured

at only one undulator configuration, the experimental results of the photon pulse duration cannot be normalized in the same way as in the simulations (see equations 8, 9 and 10 in A.2 and the normalization of figure 4.2). Therefore, in order to compare the experimental and the simulation results, a ratio between τ_{ph}^{3rd} and τ_{ph}^{1st} is presented. The green dotted line in figure 4.3(b) shows the simulation results of this ratio as a function of the normalized undulator distance. The experimental result, shown as a dot, is the ratio between the averaged pulse duration over ~ 3000 pulses of τ_{ph}^{3rd} and τ_{ph}^{1st} measured with THz streaking and agrees with theory within its respective error bars. This novel result is the basis of a future paper which is currently under preparation.

4.3   Study of the post-collision interaction effect in Auger decay using THz streaking

In previous sections, results demonstrating the strong potential of the THz streaking experiment as a pulse duration measurement diagnostic tool at FLASH have been presented, as well as statistical studies of the temporal properties of the pulses and their relation to the energy and spectral properties, which was the main focus of this dissertation. However, streaking is a powerful technique that can be used to look at dynamic processes in atoms and molecules. Within this thesis, experiments at FLASH1 at the THz undulator (BL3 beamline) were also performed using a streaking setup. The results were published in the papers [100] and [101].

Furthermore, in the scope of this thesis, the post-collision interaction (PCI) effect in Auger decay of noble gas atoms was investigated theoretically and experimentally. Firstly, theoretical studies were performed by using a semi-classical model [59] to study the PCI effect for different experimental parameters (A.3). Subsequently, a new quantum-mechanical model was proposed and compared to the semi-classical model (A.4). The results of the theoretical studies were vital in defining the design of experiments at FLASH2 using the THz streaking setup described in section 3.3. The preliminary results of the PCI experiments are presented at the end of this section.

4.3.1   Post-Collision interaction effect in Auger decay of noble gas atoms.

The ionization of an atom may, under certain conditions and depending on the excitation process, be influenced by an effect termed post-collision interaction (PCI). This effect is associated with the Coulomb field interaction of slowly receding charged particles [102]. In particular, PCI effects were observed in near-threshold inner shell photoionization of atoms followed by Auger decay [56]. In this case, the interaction with the slow photoelectron shifts the energy of the Auger electron and considerably distorts the Auger spectral line-shape. A semi-classical theory was first developed [102] in order to understand this effect and, later on, a quantum mechanical approach was established [103]. The development of time-resolved experiments enabled the study of atomic processes directly in the time domain, particularly Auger decays [104, 105]. A

first THz-assisted time-resolved study of the Auger process in atoms revealed that PCI leads to a time-dependent (chirped) Auger electron energy [57].

In reference [57], it was experimentally demonstrated - and verified by theory for the Xe (NOO) and Kr (MNN) Auger decays - that when the kinetic energy of Auger electrons is larger than that of the promptly emitted photo-electrons, the Auger electrons are chirped (the spectral shape within the pulse changes as a function of time) due to energy exchange between them. When the fast (more energetic) Auger electron overtakes the earlier emitted slower (less energetic) photo-electron, there is a screening of the electrons-ion potential, causing the Auger electron and photo-electrons to gain and lose energy respectively (see figure 2.5 in section 2.3). For that experiment, Xe (NOO) and Kr (MNN) Auger decays were initiated by ultrashort (femtosecond) XUV pulses. The atoms were ionized in the presence of a co-propagating, linearly polarized THz field which streaked the electrons. The time evolution of the Auger decay was investigated by changing the time delay between the XUV and THz pulses. A significant difference in the widths of the kinetic energy spectra for opposite THz field gradients (positive and negative slopes) was observed in reference [57], indicating an energetic chirp. The theoretical interpretation of the results was acheived using the semi-classical approach developed in reference [59].

While reference [57] found evidence of the presence of PCI effects in Auger spectra under specific conditions, the effect was studied in more detail as part of this thesis using the analytical semi-classical model developed in [59]. In A.3, the PCI effect was studied for the following noble gas atoms: Ne(KLL), Ar (LMM), Kr (MNN) and Xe (NOO), under various experimental conditions. The aim of the investigation was to understand how PCI behaves as a function of the photoelectron's energy, photon pulse duration, THz streaking field's strength and the atom's core-hole lifetime, in order to optimize the experimental parameters for future experiments at high harmonic generation (HHG) or FEL sources. In A.3, Auger electron spectra in the presence of a THz streaking field were simulated to study PCI effects in the time-evolution of photoinduced Auger decays. The PCI effect was quantified by the ratio of the widths of the Auger lines (R_ω, equation 2.32) calculated at the zero crossing and at the positive and negative (rising and falling) slopes of the THz vector potential.

The results of the simulations showed that the longer the pulse duration of the ionizing XUV pulse, the weaker the PCI effect for all atoms analyzed (see figures 1-4 in A.3); therefore, in order to measure the effect, the XUV pulse duration must be shorter than ~ 50 fs. Furthermore, the effect is stronger for transitions with a core-hole lifetime longer than 4 fs (see figure 7 in A.3). The PCI effect also exhibits a dependence on the streaking electric field strength; the smaller the field, the stronger the effect (figure 5 a) in A.3). These results were of great importance in order to prepare experiments at FLASH2 to measure PCI with the THz streaking setup.

4.3.2 Post-collision interaction effects in time-dependent theory of field-assisted Auger decay.

An analytical quasi-classical model which describes PCI effects in THz-assisted Auger transitions was developed in reference [59]. However, this model is only valid at the extrema of the THz electric field (corresponding to zero values of the vector potential) where the electron does not acquire a net kinetic energy shift.

In A.4, a simple, yet more rigorous quantum mechanical description of the PCI effects in the time-resolved Auger process is presented. It is based on the time-dependent theory of the Auger process induced by an ultra-short XUV pulse in the presence of an external laser field [58]. In addition, it uses a quasi-classical approach [106] in order to include PCI. An advantage of this model is that it can be used for any time delay between the exciting XUV and THz pulses (see figure 1 in A.4), in contrast to the semi-classical one [59]. Using the model, Auger Kr (MNN) spectra were simulated for different experimental conditions. The dependence of the PCI-distorted Auger spectra on the energy and duration of the exciting XUV pulse was studied (figures 2 and 3 in A.4), and this effect was calculated for different time delays between the XUV and the THz field (See figure 4 in A.4). It shows that the closer to the maximum of the THz vector potential, the stronger the effect (figure 5 in A.4). In addition, the PCI effect was determined for different frequencies of the THz streaking field. The results show no significant difference for the various frequencies analyzed (figure 6 in A.4). Finally, the quantum mechanical results were compared to the results of the analytical semi-classical model presented in A.3, and it was found that the latter model predicts considerably larger PCI effects in THz streaking spectra as compared to the quantum model developed in A.4. These results are expected to encourage further theoretical efforts, as well as new experiments dedicated to the investigation of the time evolution of PCI effects.

4.3.3 The experiment

As mentioned in section 3.1, FLASH2 is equipped with variable-gap undulators, and thus the FEL wavelengths can be changed relatively easily within certain boundaries. Using this feature, the PCI effect as a function of the photoelectron's energy can potentially be studied experimentally. In order to do these experiments, a second eTOF was installed in the streaking setup described in section 3.3. The new eTOF was placed in an opposing direction to the spectrometer already installed (opposite to the THz polarization direction). This upgrade enables simultaneous measurements of electrons that are accelerated and decelerated by the THz streaking field [26, 54]. Therefore, the spectrum of the Auger and photoelectrons at positive ($\dot{A}_{THz} > 0$, equation 2.28) and negative ($\dot{A}_{THz} < 0$) slopes of the vector potential was measured at the same time for every FEL pulse (figure 4.4).

As a first experiment, Kr (MNN) spectra were measured at an FEL wavelength of 13 nm (95.4 eV).
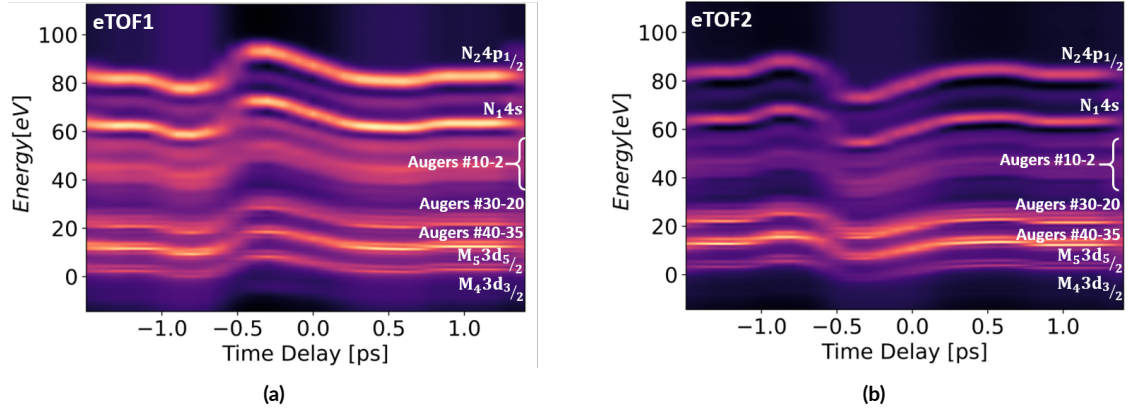
Figure 4.4: Streaking spectra of the Auger as well as the photo-electrons of krypton at an FEL wavelength of 13 nm (95.4 eV) for different time delays between the FEL and THz pulses. (a) Electrons detected with the eTOF along and (b) opposite to the THz field direction. The various photolines and Auger lines are labeled, where Augers$\#10 - 12$ denotes the $M_5N_{2,3}N_{2,3}(S_0^1), M_4N_{2,3}N_{2,3}(S_0^1), M_5N_{2,3}N_{2,1}(D_2^1), M_4N_{2,3}N_{2,1}(D_2^1), M_5N_{2,3}N_{2,1}(P_2^3), M_4N_{2,3}N_{2,1}(P_0^3, P_1^3)$ Auger transitions. Augers$\#30 - 20: M_5N_1N_{2,3}(P_1^1), M_4N_1N_{2,3}(P_1^1), M_5N_1N_{2,3}(P_1^3)$ and $M_4N_1N_{2,3}(P_2^3)$. Augers$\#40 - 35: M_5(S_0^1)$ and $M_4(S_0^1)$.

At this XUV energy a strong PCI effect in the Auger electrons is expected (as shown in A.3), since the energy of the photoelectrons $3d_{5/2}$ is almost zero. Using the photolines $N_24p_{1/2}$, the measured FEL pulse duration was ~ 40 fs FWHM. Furthermore, they were used to verify that there was no linear chirp in the XUV pulse. The single-cycle THz field strength for the experiment was ~ 120 kV/cm. The PCI effect is characterized by the ratio R_ω (equation 2.32) as described in section 2.3 and A.3. With this XUV pulse duration, XUV wavelength and THz streaking field strength, a ratio of $R_\omega \sim 2$ is expected according to the simulations presented in A.3.

Figure 4.4 shows the kinetic energy spectra of Kr 3d photoelectrons and ($M_{4,5}$NN) Auger electrons created by the FEL in the presence of the THz field as a function of the time delay between the FEL and THz pulse. The measurements were taken along the THz field direction ($\dot{A}_{THz} > 0$) with eTOF1 (figure 4.4 (a)) and opposite to the THz field direction ($\dot{A}_{THz} < 0$) with eTOF2 (figure 4.4 (b)).

In order to investigate the influence of PCI on the Auger electrons, Auger spectra were taken close to the zero-crossing of the vector potential (at ~ -0.45 ps). Figure 4.5 shows the measured reference spectra (without THz field) taken with the two eTOFs. The reference spectra show an average of ~ 200 FEL pulses and were used to identify the Auger peaks and to calculate the resolution of the eTOF detectors. There are 19 Kr (MNN) Auger transitions in the range between 36 eV and 44 eV [107]. In figure 4.5, five Auger peaks are plotted assuming a Lorentzian distribution, using the data from reference [107] and considering a width of 88 meV (since the natural width of the spectral line determined by the decay of the $M_{4,5}$ vacancy is 88 meV [108]). Due to
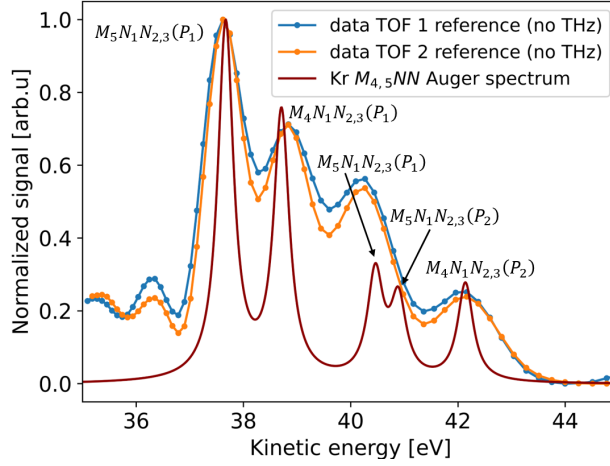
Figure 4.5: Reference spectra (without THz field) measured simultaneously with TOF1 and TOF2. Each spectrum consists of an average of ~ 200 FEL pulses. Five Kr (MNN) Auger transitions are plotted in red using the data from [107, 108] in order to identify the Auger peaks.

the limited eTOF resolution, only four peaks are resolved, where one peak (at ~ 40 eV) can be attributed to two Auger transitions. The third measured peak (from left to right, at ~ 40 eV) consists of two underlying Auger peaks and, most likely, a contribution from a background photoelectron line that may be associated with the ionization of O_2.

For the analysis of PCI first, a $4-$Gaussian fit was performed on the reference spectra. The reference widths were then convoluted with the theoretical widths ω^+, ω^- determined in A.3 for the specific parameters of the experiment. Due to the additional broadening, this resulted in an expected ratio of $R_\omega \sim 1.6$ (including the detector response), as compared to 2 from the simulations using the natural line widths. Figure 4.6 shows the streaked spectra (with THz field on) taken close to the zero-crossing of the vector potential with eTOF1 (at $\dot{A}_{THz} > 0$) and eTOF2 (at $\dot{A}_{THz} < 0$). Each streaked spectrum is composed of ~ 10 XUV pulses. A change in the width and shifting of the streaked spectra from the reference spectrum is observed.

Figure 4.7 shows the streaked spectra measured with eTOF2, including its statistical error band (shaded area) due to the limited number of electrons in a single shot (~ 70 electrons in the energy range of the shown Auger transitions - see also error discussion in A.1). The averaged streaked spectra measured with eTOF1 and eTOF2 were fitted to a 4-Gaussian function in order to obtain the widths of the peaks ω^+ and ω^-, respectively. The results are shown in table 4.2. As seen in figure 4.7, the first peak from left to right (Auger transition $M_5N_1N_{2,3}(P_1)$) is the best defined and has the smallest statistical error, whereas the last peak (Auger transition $M_4N_1N_{2,3}(P_2)$) is the least prominent and has the largest statistical error. This is reflected in the results shown in
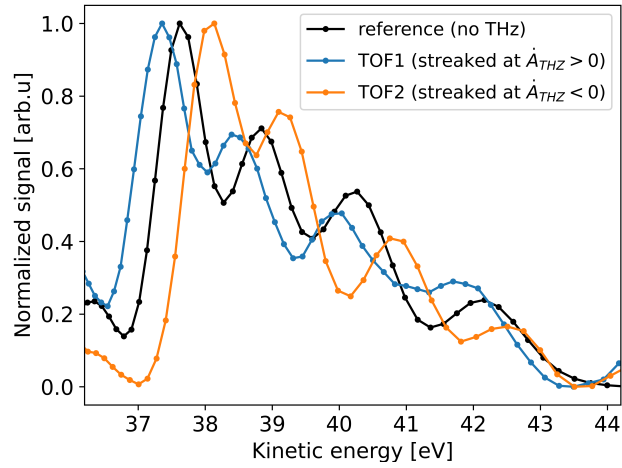
Figure 4.6: Kr (MNN) Auger spectra measured with (streaked) and without (reference) THz field close to the zero-crossing of the THz vector potential. The blue line is the streaked spectrum taken along the THz polarization direction (TOF1) and the orange line opposite to it (TOF2). A change in the width and shifting of the streaked spectra from the reference spectrum is observed.
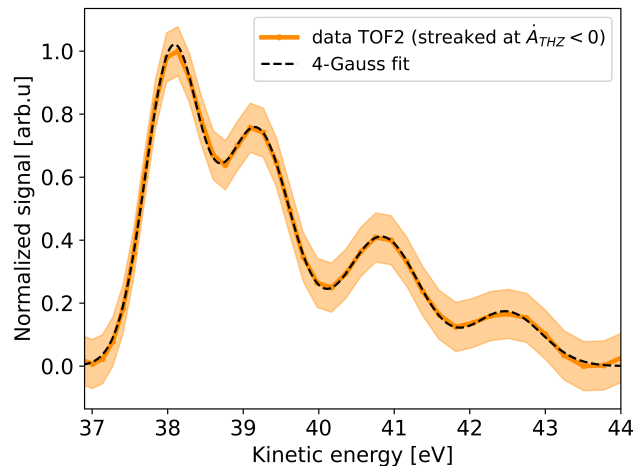

Figure 4.7: Streaked Kr (MNN) Auger spectra measured with eTOF2. The spectrum shows the average of ~ 10 FEL pulses. The shaded area depicts the error band $\pm\sigma$ caused by Poisson statistics due to the limited number of electrons in a single spectrum. The 4-Gauss fit to the data in order to obtain the widths of the peaks is shown as a dashed line. The same analysis was performed on the data measured with eTOF1.

Table 4.2: Ratio of the widths of the peaks measured along the polarization direction (ω^+) with eTOF1 and opposite to it (ω^-) with eTOF2. The widths were calculated by fitting a 4-Gaussian function to the streaked spectra (as shown in figure 4.7). Note that the ratio R_ω predicted by the semi-classical model (A.3) is ~ 1.6 and the predicted by the quantum-mechanical model (A.4) is ~ 1.1.

Auger transition	Ratio, $R_\omega = \omega^+/\omega^-$
$M_5 N_1 N_{2,3}(P_1)$	1.2 ± 0.2
$M_4 N_1 N_{2,3}(P_1)$	1.2 ± 0.4
$M_5 N_1 N_{2,3}(P_2)$	1.3 ± 0.3
$M_4 N_1 N_{2,3}(P_2)$	1.4 ± 0.6

table 4.2. The experimental results lie in between the theoretical predictions - the semi-classical model (A.3) calculated a ratio R_ω of ~ 1.6 and the quantum-mechanical model (A.4) a ratio of ~ 1.1. Unfortunately, the experimental resolution is not sensitive enough to determine which model is more suitable to describe PCI. However, these results favor the quantum-mechanical approach developed in A.4. A challenge faced in the analysis of this experimental data was the temporal jitter between the XUV and THz pulses. Since not all XUV pulses were measured at the exact same time-delay (slightly shifting the spectrum in energy) due to the temporal jitter, then averaging over many pulses causes a false shape of the spectrum as compared to an averaged spectrum with no jitter. Furthermore, as shown in A.3, the longer the FEL pulse, the smaller the PCI effect (i.e. the ratio R_ω decreases). For the experiment, an FEL pulse duration of 20 fs FWHM was requested but ~ 40 fs FWHM was achieved, decreasing the resolution of the experiment.

5

Conclusion and outlook

This cumulative thesis documents the successful implementation and commissioning of a permanent streaking setup for pulse duration and arrival time measurements at the FL21 beamline of FLASH2. This involved the thorough characterization of the experimental chamber, including the eTOF spectrometer. Furthermore, it was demonstrated that measurements of pulse duration and arrival time are feasible using only a small fraction ($\sim$ 3%) of the total FEL beam, facilitating simultaneous measurements with another beamline. Following the pioneering proof-of-principle experiments, the streaking setup presented here has been permanently installed and used as a photon pulse diagnostic tool for the wide range of FEL energies and pulse durations available at FLASH, and will remain in operation. For the pulse duration range of $\sim$ 30 fs to $\sim$ 150 fs, the streaking setup measures pulse duration with an overall precision of $\pm 20\%$. It has already been used to measure pulse duration for users, either before or after the users' beamtime, verifying if the machine setup delivered the expected pulse duration. This task is especially important when the time scales of the processes under study are close to (or strongly dependent on) the FEL pulse duration. Furthermore, the results of the streaking measurements were used to provide feedback to the machine operators, and were given to users that need to know the FEL pulse duration for the interpretation of their experimental data.

In addition, single-shot measurements of various SASE photon parameters (energy, arrival time, pulse duration and spectrum) were recorded at the same time for different FEL settings. The experimental data was used to investigate in detail how these radiation properties fluctuate and if there are correlations between the different parameters. The experimental results were compared to simulations; the comparison showed that more than $\sim$ 60% of the fluctuations in the photon properties are due to SASE physics, with the remaining fluctuations caused by technical fluctuations and measurement uncertainties. These results demonstrate that the experimental measurements agree very well with the FEL theory for the various SASE photon properties. Addi-

tionally, the results were used to derive scaling parameters that can be used to easily estimate SASE FEL fluctuations for different radiation properties without performing complex simulations. A useful result for SASE FEL users is the possibility to sort SASE FEL data by either photon energy or pulse duration, since there was no correlation predicted by theory or experimentally found between them.

Furthermore, the THz streaking setup successfully measured pulse duration and arrival time in new SASE FEL schemes, such as the two-color operation mode at FLASH2, higher order harmonics and double pulses. The results show the applicability and versatility of the streaking chamber and encourage the development of novel FEL schemes supported by THz streaking as a powerful temporal diagnostics tool.

In order to further exploit the extensive capabilities of the THz-streaking technique, the PCI effect in Auger decay was studied both theoretically and experimentally. Following the experiment that found evidence that Auger electrons may have an energetic chirp due to the PCI effect[57], this effect was studied in more detail theoretically using a semi-classical model, and a new quantum mechanical approach was developed. The results served to find the optimal experimental parameter ranges for which the PCI effect can be measured at FLASH2 using the THz-streaking setup. After comparing both theoretical models, it was found that the PCI effect predicted by the semi-classical model is up to five times as strong as that predicted by the quantum-mechanical approach. These results encouraged further experiments. The preliminary results of a PCI experiment performed at FLASH2 showed that this effect can be measured with the THz-streaking setup and favors the quantum-mechanical model. However, due to some experimental limitations such as the FEL pulse duration during the beamtime, the experimental results are not precise enough to determine which theoretical approach describes the PCI effect more accurately until more experiments are performed.

In the near future, the THz streaking setup presented in this thesis will be modified in order to extend its measurement capability range down to sub-20-fs pulses. As a first step, two new eTOFs were already installed. One was placed in front of the existing detector (anti-parallel to the THz electric field), similar to the setup in references [26, 54], and the other eTOF was installed parallel to the first one and a few ten centimeters upstream (out of the THz focus) in order to measure the reference spectrum independently for each XUV pulse. This update enables the measurement of the photon pulse chirp [26, 54], for which there was no existing direct measurement tool available at FLASH2, and which is an important parameter for some experiments.

In the future, the angular streaking technique [109] could be implemented as a complementary method to enable the characterization of even shorter pulses. Here, a circularly polarized IR field is used to streak the photoelectrons instead of a linearly polarized streaking field. Using this technique would enable measurements from the attosecond range to ~ 30 fs, which together with THz streaking would cover the full range of the pulse duration capabilities at FLASH.

In summary, the results presented in this cumulative thesis show a substantial step towards a

single-shot temporal diagnostic tool at a SASE FEL, which is highly desired in the FEL scientific community. Furthermore, the results published and the ones under preparation exhibit the potential and versatility of the THz streaking technique. Although the technique was established years ago at FELs, there is still a lot to discover, particularly with the new possibility of regularly measuring the photon pulse duration along with other FEL electron and photon parameters. These measurements, in combination with simulations of the SASE process provide a more detailed understanding of the SASE FEL mechanism, which in addition can help to improve the tuning of the FEL. This enables not only a better understanding of the SASE FEL operation and tuning, but enables user experiments to further push towards the yet unreached limits of FEL physics.

A

Peer-reviewed publications

A.1   Single-shot temporal characterization of XUV pulses with duration from ~10 fs to ~350 fs at FLASH

Single-shot temporal characterization of XUV pulses with duration from ~10 fs to ~350 fs at FLASH

Rosen Ivanov[1] , **Ivette J Bermúdez Macias**[1], **Jia Liu**[2] , **Günter Brenner**[1],
Juliane Roensch-Schulenburg[1], **Gabor Kurdi**[3], **Ulrike Frühling**[4,5],
Katharina Wenig[4], **Sophie Walther**[4,5], **Anastasios Dimitriou**[4,5], **Markus
Drescher**[4,5], **Irina P Sazhina**[6], **Andrey K Kazansky**[7,8,9], **Nikolay M
Kabachnik**[1,2,6] **and Stefan Düsterer**[1]

[1] Deutsches Elektronen-Synchrotron (DESY), Notkestrasse 85, D-22603 Hamburg, Germany
[2] European XFEL GmbH, Holzkoppel 4, D-22869 Schenefeld, Germany
[3] Elettra-Sincrotrone Trieste, 34149 Basovizza, Trieste, Italy
[4] Institute for Experimental Physics, University Hamburg, Hamburg, Germany
[5] The Hamburg Centre for Ultrafast Imaging, Luruper Chaussee 149, Hamburg, Germany
[6] Skobeltsyn Institute of Nuclear Physics, Lomonosov Moscow State University, Moscow 119991, Russia
[7] Departamento de Fisica de Materiales, University of the Basque Country UPV/EHU, E-20018 San
Sebastian/Donostia, Spain
[8] Donostia International Physics Center (DIPC), E-20018 San Sebastian/Donostia, Spain
[9] IKERBASQUE, Basque Foundation for Science, E-48011 Bilbao, Spain

E-mail: rosen.ivanov@desy.de

CrossMark

Abstract
Ultra-short extreme ultraviolet pulses from the free-electron laser FLASH are characterized
using terahertz-field driven streaking. Measurements at different ultra-short extreme ultraviolet
wavelengths and pulse durations as well as numerical simulations were performed to explore
the application range and accuracy of the method. For the simulation of streaking, a standard
classical approach is used which is compared to quantum mechanical theory, based on strong
field approximation. Various factors limiting the temporal resolution of the presented terahertz
streaking setup are investigated and discussed. Special attention is paid to the cases of very
short (~10 fs) and long (up to ~350 fs) pulses.

Keywords: temporal diagnostic, XUV pulses, SASE FEL, FLASH, THz streaking, single
cycle terahertz pulse

(Some figures may appear in colour only in the online journal)

1. Introduction

Free-electron lasers (FELs) working in the extreme ultraviolet (XUV) and x-ray region deliver unrivalled intense pulses of fs-duration [1–6]. They allow the investigation of basic light–matter interactions at high photon intensities such as multiphoton ionization of atoms and molecules. The most promising application of the XUV FELs is the investigation of the time evolution of electronic processes by applying pump-probe techniques. For the realization of this method it is crucial to know the temporal characteristics of the XUV pulses delivered by the FEL such as arrival time, pulse duration and—at best—the temporal shape of the pulses.

Most FELs in the XUV and x-ray range operate in the self-amplified spontaneous emission (SASE) regime relying on stochastic processes, resulting in pulses varying on a shot-to-shot basis [7, 8]. Each pulse is composed of independent, temporally coherent spikes, with the duration of these spikes ranging from hundreds of attoseconds to tens of femtoseconds depending on the wavelength and coherence length of the FEL process. The stochastic nature of the FEL radiation leads to large shot-to-shot fluctuations in the temporal characteristics of the pulses. Most of the known temporal characterization methods are based on averaging over many pulses [9], which strongly limits the accuracy of the pump-probe experiments. The necessity to know the duration and temporal profile of each individual pulse stimulated the development of different methods that are suitable for single-shot temporal characterization. Besides terahertz (THz) streaking, there are mainly three different techniques available: (1)—the observation of optical properties changes in solid thin films upon XUV pumping (e.g. [10, 11]). This method however only works within a very limited dynamic range in the XUV and it is questionable how the method can be scaled to the MHz high-repetition rate of FLASH. (2) A different approach investigates the temporal profile modulation of the electron bunch during the XUV/x-ray creation process using a radiofrequency transverse deflector device [12]. It has been shown that these measurements can provide photon pulse durations with very high temporal resolution, however, currently cannot be scaled to the burst mode structure of FLASH. (3) A similar approach using an optical replica of the electron bunch modulation ('optical afterburner') [13] is potentially also able to deliver single-shot pulse duration information but has so far not been demonstrated experimentally.

THz streaking [14–19] on the other hand can overcome these limits and has the potential to deliver single-shot pulse duration information basically wavelength independent and over a large dynamic range (in pulse duration and FEL energy). It can be operated with repetition rates up to several hundred kHz (potentially even MHz). In addition, it can provide arrival time information of the FEL pulse with respect to the laser driving THz generation for each single pulse with an accuracy well below 10 fs [18]. Due to its wide working range the concept can not only be used at soft x-ray FEL like FLASH, but also at hard x-ray FELs [17, 20].

Recently a THz-field driven streaking setup has been installed at FLASH1 [18] delivering photon pulse duration as well as arrival time information for each individual XUV pulse. In this paper, we report on measurements performed with this streaking setup and theoretical simulations devoted to the investigation of its accuracy and limitations. Previous THz streaking experiments [14, 15, 17, 19] have been performed at fixed FEL settings where the average XUV wavelength, pulse duration and pulse energy were essentially stable. Here, for the first time, a comprehensive collection of measurements recorded at various FEL parameters governing the pulse duration are presented. From shortest possible FLASH SASE pulses in the sub 10 fs range (single longitudinal mode) with

only few μJ of pulse energy to intense >100 μJ pulses containing a large number of longitudinal modes extending to pulse durations >300 fs (FWHM) have been investigated.

The paper structure is as follows: the next section is devoted to the theoretical description of the streaking process which is used in the simulations and the reconstruction of the temporal profiles from the electron time-of-flight (eTOF) measurements. In section 3 the experimental setup at FLASH1 is briefly described providing necessary information about the parameters of the XUV and the THz fields. In subsection 3.2 the analysis of the possible error sources as well as limitations of the described streaking setup is given. Section 4 presents experimental results for different XUV pulse durations and various parameters of the THz field. Finally, we conclude in section 5.

2. Theoretical background

2.1. Streaking principle. Classical description

We consider the photoionization of an atom by a short (femtosecond) XUV pulse in the presence of a co-propagating THz radiation field. Both fields are linearly polarized in the same direction. In the scope of the current paper, we assume a single-cycle THz pulse with duration much longer than that of the XUV pulse [15]. The XUV pulse produces a distribution of photoelectrons via ionization that carries the temporal information of the ionizing XUV pulse. The kinetic energy of the photoelectrons is modified by the interaction with the THz electric field, and their final energy is determined by the instant THz-field vector potential at the moment of ionization. Thus, the temporal structure of the electron wave packet is mapped onto the kinetic energy distribution of the photoelectrons.

Classically, one can write the final energy W of photoelectrons emitted at the instant of time t as (atomic units (a.u.) are used in this section unless otherwise indicated)

$$W(t) = W_0 + qA_{\text{THz}}(t)\cos\theta - (A_{\text{THz}}(t))^2/2, \qquad (1)$$

where W_0 is the initial energy of the ejected electron without THz field, $q = \sqrt{2W}$ is its final linear momentum directed at angle θ to the polarization direction of both pulses, and $A_{\text{THz}}(t) = -\int_t^\infty E_{\text{THz}}(t')dt'$ is the THz-field vector potential, with $E_{\text{THz}}(t')$ being the THz electric field. Note that the THz field is weak and the quadratic term in equation (1) can be ignored. One can further simplify the THz field-induced photoelectron energy modulation to $\Delta W_{\text{streak}} = W - W_0 \cong qA_{\text{THz}}(t)$ by assuming $\theta = 0$ (detecting only electrons along the polarization direction). Thus, the shift of the kinetic energy peaks provides the arrival time of the XUV pulse.

The relation between the time interval δt and the energy interval $\delta(\Delta W_{\text{streak}})$ is as follows:

$$\delta(\Delta W_{\text{streak}}) = s\delta t = q\frac{dA_{\text{THz}}(t)}{dt}\delta t, \qquad (2)$$

where s is the so-called streaking speed. As a first approximation, the value s may be set to be a constant proportional to the derivative of the vector potential at the center of the slope. The pulse duration τ_{XUV} can thus be extracted from the broadening

of the photoelectron spectrum due to the presence of the THz field. For a Fourier limited Gauss-shaped peak the following equations apply:

$$\sigma_{streak}^2 = \sigma_{ref}^2 + s^2 \tau_{XUV}^2, \tag{3a}$$

$$\tau_{XUV} = s^{-1}\sqrt{\sigma_{streak}^2 - \sigma_{ref}^2}, \tag{3b}$$

with σ_{streak} and σ_{ref} being the widths of the peak with and without the THz field, respectively.

If the XUV pulse has a linear chirp, e.g. $E_{XUV}(t) = \tilde{E}_{XUV}(t)\cos(\omega t + ct^2)$ where $\tilde{E}_{XUV}(t)$ is the envelope and ω is the center frequency of the XUV field, equation (3a) becomes $\sigma_{streak}^2 = \sigma_{ref}^2 + \tau_{XUV}^2(s^2 + 4cs)$ which may be used for experimental determination of the chirp [14, 19, 21].

As the THz pulse is focused the phase of the THz field changes continually along the propagation direction. This effect, often called Gouy phase, changes the phase by 180° across the Raleigh range. Thus, electrons generated at different positions within the interaction region are accelerated by a slightly different THz field and therefore experience a different energy modulation. This leads to an additional broadening σ_{Gouy} of the photoelectron line independent of the XUV pulse duration [21]. The broadening can, at least approximately, be determined from the THz focusing geometry and the acceptance volume from which the electrons are collected. This Gouy phase broadening has to be subtracted from the actually measured width:

$$\tau_{XUV} = s^{-1}\sqrt{\sigma_{streak}^2 - \sigma_{ref}^2 - \sigma_{Gouy}^2}. \tag{4}$$

2.2. Quantum mechanical simulation

A more accurate description of the streaking process can be achieved by a quantum mechanical approach. For calculations of the double differential cross section of the photoionization (in energy and angle), the strong field approximation (SFA) can be used [22] since it is valid for medium strong streaking fields and relatively fast electrons (kinetic energies of more than 1 a.u. (27.2 eV)). Realization of the SFA in the context of streaking was discussed in references [23–26]. Within this approximation, pulse duration, temporal profile, kinetic energy, target gas, streaking field and strength can be independently varied to study the role of each parameter in the streaking process. As a result, the simulation provides the energy and angular resolved double differential cross sections for the streaked photoelectrons. Several examples will be discussed later.

The SFA approach, however, is computationally rather demanding limiting its applicability in fast (on-line) shot-to-shot analysis of experimental spectra. The description of the process can be significantly simplified within a quasi-classical approach using the stationary phase method as suggested in [24, 25]. Recently, a very simple and fast method of FEL pulse retrieval from the THz streaking spectrum has been suggested in reference [26]. The method is based on SFA and uses the stationary phase approximation. As shown in reference [26] the double differential cross section (DDCS) for XUV ionization

in the presence of the THz field can be presented as:

$$\frac{d\sigma}{dWd\Omega}(W,\theta) = \frac{2\pi E_{XUV}^2(t_s)}{E_{THz}(t_s)\sqrt{q_0^2 - 2W\sin^2\theta}}\frac{d\sigma^{(0)}}{dWd\Omega}\left(\tilde{W}_s,\tilde{\theta}_s\right), \tag{5}$$

where the last factor is the common DDCS of photoionization of the l_0 shell of the atom by the XUV pulse alone which can be presented in a standard form:

$$\frac{d\sigma^{(0)}}{dWd\Omega}(\tilde{W}_s,\tilde{\theta}_s) = \frac{\sigma_{l_0}^{(0)}\left(\tilde{W}_s\right)}{4\pi}(1 + \beta\left(\tilde{W}_s\right)P_2(\cos\theta_s)), \tag{6}$$

here $\sigma_{l_0}^{(0)}(\tilde{W}_s)$ and $\beta\left(\tilde{W}_s\right)$ are the cross-section and anisotropy parameter for the photoionization of the l_0 shell of the atom by the XUV pulse alone, $P_2(x)$ is the second Legendre polynomial. The energy $\tilde{W}_s$ and angle $\tilde{\theta}_s$ are defined as:

$$\tilde{W}_s = \frac{1}{2}\left|\vec{q} - \vec{A}_{THz}(t_s)\right|^2, \tag{7}$$

$$\tilde{\theta}_s = \arccos\left(\cos\theta - A_{THz}(t_s)/q\right). \tag{8}$$

They have the meaning of the electron energy and emission angle before entering the THz field. The stationary point t_s (the time of ionization providing the final energy ($W = q^2/2$) is given by the equation:

$$(q\cos\theta - A_{THz}(t_s))^2 + q^2\sin^2\theta - q_0^2 = 0, \tag{9}$$

with $q_0 = \sqrt{2W_0}$ and W_0 being the initial energy of the photoelectrons.

Equation (9) has two solutions $q\cos\theta - A_{THz}(t_s) = \pm\sqrt{q^2\sin^2\theta - q_0^2}$. The experiment implies that the momenta q_0 and q involved are substantially larger than the magnitude of the vector potential of the THz field A_{THz}. Thus, if one considers the case $\cos\theta > 0$, the solution with the plus sign should be chosen while the solution with the minus sign should be chosen for $\cos\theta < 0$. If only complex roots t_s of equation (9) exist, for computation of the SFA amplitude the saddle point method should be used instead of the stationary phase method. The saddle point method allows one to obtain the Airy function representation for the SFA amplitude which exponentially decreases with increase of the absolute value of the imaginary part of t_s. For the present problem this case is not relevant.

The expression (5) can be directly used to retrieve the temporal XUV pulse profile from a measured electron energy spectrum:

$$E_{XUV}^2(t_s) = \frac{E_{THz}(t_s)\sqrt{q_0^2 - 2W\sin^2\theta}}{2\pi}$$

$$\times \frac{d\sigma}{dWd\Omega}(W,\theta)\left[\frac{d\sigma^0}{dWd\Omega}\left(\tilde{W}_s,\tilde{\theta}_s\right)\right]^{-1}. \tag{10}$$

The retrieval strategy is the following: for each energy $W = q^2/2$, angle θ and a given time-dependence of the THz vector potential $A_{THz}(t)$, the emission moment t_s is found from the relation (9). Then the energy $\tilde{W}_s$ and angle $\tilde{\theta}_s$ are calculated according to equations (7) and (8), respectively. Finally using
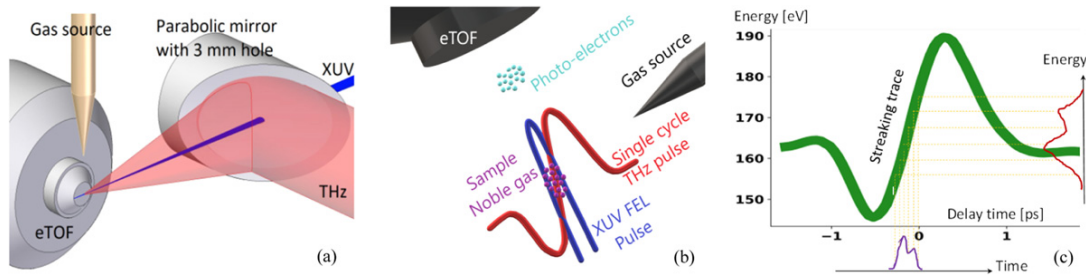
Figure 1. (a) Geometry of the THz streaking setup used at the PG0 beamline of FLASH. (b) THz streaking principle. Photoelectrons are emitted from free (noble gas) atoms ionized by short XUV pulses in the presence of a strong linearly polarized THz field, thus modifying the momentum component of the photoelectrons. (c) Mapping of the temporal information to the kinetic energy distribution from the THz vector potential (streaking trace).

equation (10) the XUV pulse is evaluated, provided the cross section $d\sigma^0/dWd\Omega$ is known.

Since expression (10) is algebraic, the pulse retrieval is as fast as using the classical expression (1) with linear approximation of the vector-potential. The former expression (10) has the advantage that it can be used for any shape of the vector potential and therefore is suitable also for comparatively long XUV pulses. The only limitation is that the THz vector potential must be a monotonous function in time during the XUV pulse duration.

3. Experiment

3.1. THz-streaking setup and data acquisition

The experiments were performed at the plane grating (PG) monochromator beamline [27, 28] of the free-electron laser in Hamburg (FLASH) [1]. The PG beamline was operated in the so-called parallel configuration. This configuration enables the utilization of the 0th diffraction order (at the PG0 beamline branch) for experiments or diagnostics (THz streaking in our case) while the dispersed radiation is simultaneously used to measure the XUV FEL spectrum with high resolution.

Various settings of the accelerator were used to test the applicability of the streaking diagnostic over a wide range of FEL parameters. The FEL was operated in single bunch mode at 10 Hz, with electron bunch charges altered from 0.08 nC up to 0.44 nC, leading to different XUV pulse durations from ∼10 fs to ∼350 fs (FWHM) as well as to XUV pulse energies ranging between only a few μJ at 7 nm to >100 μJ per pulse at 20 nm.

An 80 fs, 800 nm, 6.5 mJ, 10 Hz Ti:Sapphire laser [29] with a sub 10 fs synchronization to the optical master oscillator [30] was used to generate single-cycle THz streaking pulses based on pulse front tilt optical rectification in a lithium niobate (LiNbO$_3$) crystal [31]. The obtained THz pulse energy was on the order of 15 μJ leading to a THz field strength up to 300 kV cm^{-1} (see figure 3 in [18]). A detailed description of the experimental setup and the working principle can be found in reference [18]. In brief, the XUV pulses are focused into a noble gas target (see figure 1) and create photoelectrons via ionization. The XUV focus size is chosen to be sufficiently smaller (∼300 μm diameter (FWHM)) as compared to the THz

focus size of 2.1 mm (FWHM). A Ce:YAG screen and fast photodiode were used to find the coarse spatial and temporal overlap between the XUV and THz pulses [32].

Neon was chosen as the target gas providing the 2p and 2s photoelectron spectral lines in the energy range of interest. The electron binding energies are 21.7 eV (2p) and 48.5 eV (2s), respectively [33]. At the FEL wavelength of 6.8 nm (182.3 eV), two single, well separated spectral lines with kinetic energies of 160.6 eV and 133.8 eV were measured. At 20 nm (62.0 eV) XUV wavelength the photoelectron kinetic energies are 40.3 eV and 13.5 eV, respectively.

As will be shown below, the range of XUV pulse durations from 30 fs $< \tau_{XUV} <$ 150 fs can be evaluated for XUV wavelengths up to about 30 nm. For longer wavelengths, pulse durations of 30 fs approach the few-mode operation and have to be treated more carefully. Furthermore, the photoelectron kinetic energy gets smaller, thus making it increasingly more difficult to reach sufficient streaking strength (see equation (2)). Nevertheless, pulse duration measurements using a similar setup have been successfully measured at 34 nm seeded VUV radiation [19].

The mapping between the streaked kinetic photoelectron energy and the time is given by $\Delta W(t) \approx eA_{THz}(t)\sqrt{2W_0/m_e}$. The right-hand side of this equation is usually called 'streaking trace' and provides the maximum energy shift of photoelectrons for a given THz field. By fitting the linear part of the vector potential we can evaluate the streaking speed 's' which relates the energy shift and emission time [14, 21].

3.2. Possible sources of errors and limitations

One of the main challenges of pulse duration diagnostics is the determination of measurement error bars. There are several different sources of inaccuracy that have already been discussed in [14–16, 34]. Here we summarize the factors that limit the accuracy and the temporal resolution of THz streaking in general. In section 4 we focus on the specific influence of the error sources for the different pulse duration ranges and provide experimental results from FLASH.

3.2.1. Spectral fluctuations of the SASE FEL pulse.
As follows from equation (2) the shorter the XUV pulses are, the smaller the broadening induced by the streaking for a certain THz field is. Ultimately, for the shortest pulses available at

Table 1. Broadening of the streaking signal in fs (FWHM) calculated for 300 kV cm^{-1} THz field and different horizontal positions (along the FEL propagation) of the eTOF with respect to the THz focus and for different acceptance volumes-source size (horizontal length) of the eTOF [18].

eTOF position (mm)	Source size (mm)	Phase (rad)	Gouy broadening FWHM (fs)
0	0.25	0.023	6.2
0	0.5	0.047	13
0	0.75	0.071	19
6	0.25	0.017	4.7
6	0.5	0.033	10
6	0.75	0.053	14

FLASH the broadening approaches the spectral width fluctuations caused by the SASE process (see e.g. figure 6). In addition, for short pulses only a few or eventually one spectral mode is present [35]. Thus, the spectral distribution changes significantly from shot to shot while the influence of the broadening due to streaking is decreasing, leading to a more challenging data analysis. For this work it is mandatory to use the information of reference spectra from each XUV pulse measured either by a second eTOF [14] or by an XUV spectrometer. In the present case, the XUV spectral distribution is measured for each FEL pulse simultaneously to the THz streaking by the PG monochromator beamline operating in spectrometer mode [27]. These spectra can then be used to provide the reference energy width on a single-shot basis with significantly higher resolution as compared to an eTOF [27]. In order to crosscheck the approach, a set of un-streaked photoelectron spectra were recorded and the determined width of these eTOF spectra were found to correlate well with the spectral width determined by the XUV spectrometer. Since the few-spectral-mode substructure is also visible in the eTOF spectra an analysis based on a single-peak Gaussian approximation has severe limitations and the analysis has to be adapted individually for each pulse as has been shown in [14, 15].

An alternative way to cope with the spectral fluctuations of the SASE pulses is the utilization of Auger emission processes. Here the SASE pulses eject an inner shell electron of noble gas atoms. The excited ions will later decay via the emission of Auger electrons. The energy of the Auger electrons only depends on the involved atomic states and is independent of the energy of the ionizing photons. The spectral width of the Auger electrons is determined by the lifetime of the excited state and is typically about 100 meV or smaller [36]. Thus, the spectra of the Auger electrons are extremely narrow and stable as compared to direct photoelectron spectra at SASE FELs. The measured temporal distribution of the Auger-electron wavepackets is a convolution of the temporal profile of the ionizing light pulse and the exponential Auger decay. The XUV pulse duration can be extracted from the streak-measurements by a simple deconvolution. The Auger lifetimes are usually well known and typically lie in the range of a few femtoseconds. Therefore they do not pose a severe limit for the target pulse duration range.

3.2.2. Gouy phase broadening. The THz phase shift before and after the focus leads to an additional broadening of the eTOF signal resulting in a longer retrieved XUV pulse. Our eTOF spectrometer has a ∼0.5 mm FWHM acceptance range [18]. In table 1 we present the Gouy broadening calculated for our THz source [18] for different acceptance volumes, source size (horizontal length) and interaction point position regarding the THz focus. In order to reduce the Gouy phase induced broadening, one can either move the interaction point away from the THz focus position or minimize the interaction volume. The latter could be achieved by using a more narrow gas target and a restricted eTOF acceptance range.

3.2.3. eTOF spectrometer resolution, acceptance angle and signal to noise ratio (SNR). The energy resolution of the used eTOF (Kaesdorf ETF11) is approximately 1% of the initial electron kinetic energy similar to the photon energy bandwidth of the XUV pulse. Thus, in the case of 7 nm XUV wavelength, the un-streaked peak width is on the order of 1.0–1.5 eV. It should be noted that for a given eTOF spectrometer, the temporal resolution can be improved either by applying a more intense THz field or by streaking more energetic photoelectrons.

Nevertheless, the increased energy resolution usually leads to a reduced collection efficiency, and it is challenging to achieve high energy resolution and high collection efficiency simultaneously. The single-shot streaked photoelectron signal has to be intense enough to determine the streaking for each single XUV pulse, i.e. to collect a sufficient number of electrons per pulse while avoiding unwanted spectral broadening due to space charge resulting from too many ions created in the FEL focal volume [37]. By increasing the target gas pressure until a significant broadening of the un-streaked photo-line was observed, we could determine that a total number of collected electrons in the range of few hundred per XUV pulse does not lead to significant space charge broadening. Considering the 45° collection angle this corresponds to a total number of a few ten thousand electrons within the FEL focus volume.

The collected electrons are distributed by the time-of-flight principle of the spectrometer to a certain time interval which is typically few times longer than the signal produced by a single electron (1.2 ns (FWHM) for the used setup).

Thus the recorded amplitude of an eTOF trace at a certain point is typically composed of a few tens of electrons only.

The finite number of electrons contributing to the signal leads to a statistical uncertainty of the signal shape [21]. In the case of a Gaussian distribution the uncertainty due to the Poisson statistics can be easily calculated. For n electrons contributing to the amplitude of the photoelectron signal, the uncertainty of the amplitude is given by Poisson statistics: $\sqrt{n}$. Thus the uncertainty range for the normalized amplitude is $1 \pm 1/\sqrt{n}$ as shown in figures 5, 7 and 9.

A simulation of the streaked eTOF signal dependence on the acceptance angle was performed to verify the additional broadening due to the rather large acceptance angle of the used eTOF spectrometer. Using equation (5) the DDCS was calculated for the model case of six 5 fs XUV pulses in three pairs
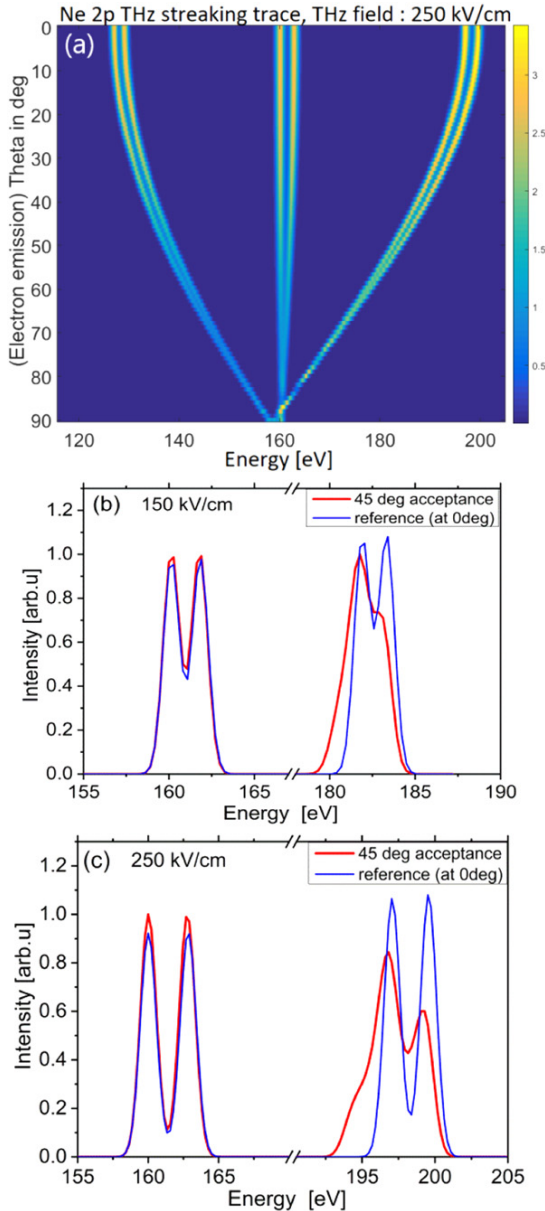
Figure 2. SFA simulation according to equation (5). The 2D figure shows the double differential cross-section simulated for the neon 2p ionization (at an incident photon energy of 182 eV/6.8 nm) using three pairs of 5 fs (FWHM) XUV pulses which are spaced by 15 fs while the pairs are 200 fs separated. A 250 kV cm^{-1} streaking field was chosen. The middle pair was set at the zero crossing of the vector potential. The streaking field acts strongest at 0 degrees (electrons emitted parallel to the THz polarization) and its effect is decreasing for higher angles. In the angular range of ±22.5 degrees for the used spectrometer there is already a certain change visible in the angular distribution. The lineouts (b) and (c) show the integrated photoelectron signal for the angular acceptance of ±22.5 degrees (red) and for the reference signal taking only the emission at 0 degrees into account—(blue). Two cases are shown: for a THz field of (b) 150 kV cm^{-1} and (c) 250 kV cm^{-1}. While there is a significant difference in the resolution for the temporally shifted peaks ($\sim$190 eV), the difference between the large acceptance angle and the reference is almost negligible for the streaked signals at the zero crossing of the vector potential ($\sim$160 eV). One can also see the better resolution at 250 kV cm^{-1} compared to 150 kV cm^{-1}.
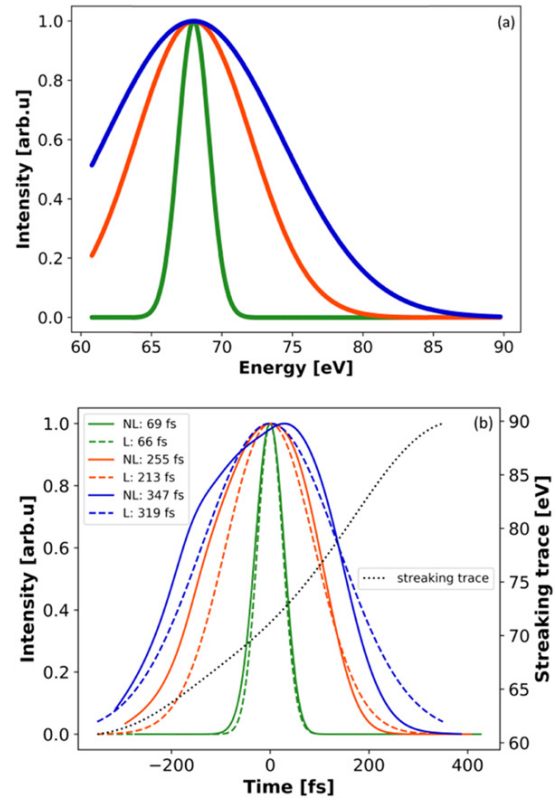

Figure 3. XUV pulse retrieval simulations using equation (10). Figure 3(a) shows three streaked Gaussian pulses of different XUV durations in the energy domain (with a central energy of 68 eV). The lower panel figure 3(b) displays the corresponding retrieved XUV pulses. The dashed lines denote the linear (L) reconstruction of the pulse (assuming a linear behavior of the main slope of the vector potential); the solid lines denote the reconstruction of the same streaked pulse but using equation (10) (NL) with a measured THz potential (streaking trace). The streaking trace is shown in black dots. For pulses <150 fs, the reconstruction gives a Gaussian-like pulse. As the pulse duration increases, the shape of the THz vector potential has a greater influence, leading to a considerable change in the shape of the XUV pulse.

spaced by 200 fs and each of the pairs separated by a 15 fs interval. The calculation was performed for neon 2p ionization at an XUV wavelength of 6.8 nm (electron energy 160 eV) in a THz field of 250 kV cm^{-1}. As shown in figure 2(a) the strongest effect of the streaking field is for electrons moving along the polarization direction (theta = 0 degrees).

For electrons moving perpendicular to the THz field (90 degrees) there is practically no energy shift. It is interesting to note that the photoelectron lines do not cross the initial photoelectron energy of 160 eV but the electrons not emitted at the zero crossing of the streaking trace end up with less kinetic energy at 90 degrees than the un-streaked electrons. In equation (1) there are two terms depending on the field ($pA_{THz}(t)\cos\theta$) and ($A_{THz}(t)^2$). The term ($A_{THz}(t)^2$) is typically very small and can be neglected, however, it causes the asymmetric shift at 90 degrees.

The angular distribution at the zero crossing of the THz vector potential has almost no angular dependence. Therefore, a

larger acceptance angle does not limit the resolution significantly. On the other hand, at streaking positions outside the zero crossing (yielding an energetic shift at 0 degrees), a significant effect of the acceptance angle can be observed (see figures 2(b) and (c)).

In our case, the acceptance angle of 45 degrees (full solid angle) shows only an additional broadening of <1 fs at the zero crossing of the vector potential and <5 fs measured 200 fs away from the crossing. Reducing the field to 150 kV cm^{-1}, the two pulses located 200 fs away from the crossing cannot be resolved anymore showing the importance of the correct setting of the relative timing between XUV and THz fields.

3.2.4. Influence of the non-linearities of the THz vector potential. Usually the analysis of the streaking spectra is performed assuming a linear slope in the THz vector potential (constant streaking speed). However, the vector potential is non-linear and the streaking speed depends on the arrival time. For very short pulses and for arrival times close to the zero-crossing of the THz field vector potential the difference is negligible. Nevertheless, for longer pulses this difference may be considerable. We investigated the influence of the non-linear ramp by retrieving Gaussian streaked XUV pulses using equation (10) for different pulse durations. The results are shown in figure 3. When the pulses are almost as long as the range of the vector potential slope, the non-linearity is reflected as a change in the shape of the pulse as well as a small shift in the arrival time.

3.2.5. SASE induced error sources. Another source of uncertainty results from radiation properties of the SASE pulse itself. Measurements of the electron phase space and the spectral width of the XUV radiation give strong hints that the SASE radiation can be chirped due to the influence of space charge and radio frequency (RF) slopes [38–41]. The energy chirp results in an SASE pulse whose leading part has a slightly different average wavelength as compared to the trailing part. This leads to different measured pulse durations depending on the relative sign of the THz streaking field and the chirp as explained e.g. in [21]. To estimate the influence of the effect, one can compare the pulse durations retrieved from the positive and negative THz slopes (compare streaking trace shown in figure 1(c), if only one eTOF is used. For two eTOFs facing each other see [14, 21]) the chirp can be derived for each measured XUV pulse.

4. Measurements and discussion

4.1. Streaking in the 'standard' XUV pulse range (30 fs < τ_{XUV} < 150 fs)

Before focusing on the limits of the method, we have investigated the 'standard' pulse duration regime of FLASH. Note that the error sources discussed above are in a tolerable range and the pulse duration can be determined rather accurately. A detailed investigation of the pulse duration fluctuations and their correlations to other pulse parameters such as pulse energy and spectral distribution was discussed in [42]. For this pulse duration region the influence of the different error sources is comparatively small.
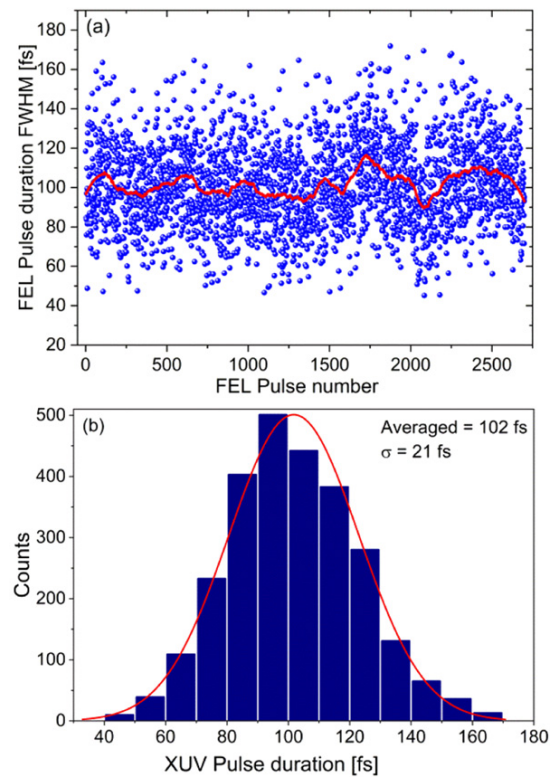

Figure 4. (a) Single-shot pulse duration measurements shown for three thousand FLASH pulses. The red line indicates the mean value of ~102 fs FWHM. The error bars of each measured pulse duration (not shown in the plot) is ±20% including all different contributions discussed in the text. (b) Histogram of pulse durations.

Figure 4 shows the single-shot pulse duration with the unavoidable and expected fluctuations due to the SASE process pointing again on the need to provide a single-shot diagnostic for SASE based FELs.

4.1.1. Reference spectra-SASE fluctuations. For the used experimental setup, the streaked photoelectron spectra are significantly broadened as compared to the un-streaked ones (figures 5 and 6(b)). We therefore can simplify the analysis by recording the averaged un-streaked reference spectral width by blocking the THz beam every few minutes.

Since the eTOF resolution is not good enough to resolve the temporal sub-structure in the streaked spectrum, we used a Gaussian fit to determine the line width (FWHM) of both streaked and un-streaked spectra. In order to get an estimate of the error introduced by taking the averaged reference, the resulting XUV pulse duration was calculated by using the smaller and larger FWHM values of the reference spectrum width histogram. The widths of the reference spectra histogram shown in figure 6(b) is 0.9 ± 0.1 eV which leads (using equation (3b)) to an uncertainty of <1% for determination of the pulse duration and therefore negligible.

4.1.2. Gouy phase broadening. The influence of the Gouy phase was taken into account for the THz beam shape around the interaction point (see also figure 4 in reference [18]).
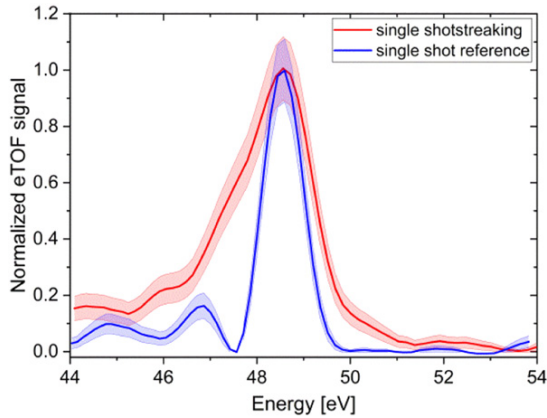
Figure 5. Streaked (red) and un-streaked (blue) photoelectron spectra of ∼60 fs (FWHM) XUV FEL pulses are shown (thick lines) including the $1/\sigma$ error bars (shaded area) caused by the Poisson statistics due to the limited number (about 80–100 electrons in the peak) of electrons in the spectrum. The streaking speed s was 0.05 eV fs^{-1}. FEL photon energy was 70.2 eV (wavelength 17.6 nm). Streaked spectrum for Ne 2p was taken at the 0-crossing of the THz-vector potential.

According to table 1, the Gouy broadening is $(13 \pm 2$ fs$)$ for the THz focus position and ∼0.5 mm source size (horizontal length). The uncertainty in the Gouy broadening stems from the not precisely known source size. Due to the quadratic dependence, the influence on the acquired pulse duration is rather small (see equation (3)) and the uncertainty in the knowledge of the Gouy phase leads to an error of <5%.

4.1.3. eTOF spectrometer resolution, acceptance angle and signal to noise ratio (SNR). As shown in figure 2 the broadening by a larger angular acceptance is (at the zero crossing of the vector potential) only a few fs and thus leads, in the considered pulse duration range, to an error of less than 5%.

The photoelectron peak width/shape has an uncertainty due to the limited number of electrons in a shot (∼200–500 electrons). The finite number of electrons contributing to the signal, leads to a statistical uncertainty of the signal shape. The statistical error of the width determination together with the Gaussian fitting leads to an uncertainty of 10%–25% as illustrated in figure 5. Typically, the eTOF resolution in combination with counting statistics shows an error that is too large for a detailed analysis of the pulse shape. Thus, only the pulse duration is analyzed. However, for longer pulses some information about the rough overall pulse structure can be determined as shown in section 4.2.

4.1.4. Influence of the non-linearities of the THz vector potential. In the considered pulse duration range, the SASE pulses consist of several sub pulses which cannot be resolved by the current eTOF spectrometer, thus we only apply a Gaussian fit. As shown in figure 3 the influence of the non-linear THz field is only a few percent and thus for the standard analysis, the linear approach (equation (4)) can be applied.

4.1.5. SASE induced error sources. Potentially, a strong energy chirp in the electron bunch generating the XUV pulse,

can lead to a corresponding frequency chirp of the XUV pulse which is not detectable on a single shot basis with the present setup due to the given statistical uncertainty. However, the average amount of frequency chirp was determined by comparing the average streaking width on the positive and negative vector potential slope, similar to how it was done in reference [19]. Interestingly, we did not find an indication of chirp (larger than the error bars) for the whole large range of measured FEL parameters.

In summary, for pulse durations in the range 30 fs $< \tau_{\mathrm{XUV}}$ < 150 fs we can state a typical uncertainty of $\pm 20\%$ for the determination of the single-shot pulse duration.

4.2. Exploring the upper limit: 'long' ($\tau_{\mathrm{XUV}} > 150$ fs) XUV pulses

For pulses that cover a significant fraction of the streaking slope, the THz streaking induced broadening is so large that the XUV pulse shape deviates from the initial Gaussian shape and shows a convolution of the reference line shape with the actual XUV pulse shape (see figure 6(c)). In this case, we can determine not only a value (FWHM) for the pulse duration but reconstruct the pulse shape of the individual XUV pulses, making a deconvolution of streaked and reference spectra using the non-linear equation (10) (see figure 7). Note, that here the influence of the various error sources is different as compared to the standard streaking case (section 4.1).

4.2.1. Reference spectra-SASE fluctuations. One can see from figure 6(c) that the width distribution of the reference spectra (no THz) and of the actual streaked spectra are sufficiently well separated. Thus, the SASE fluctuations show almost no contribution to the pulse duration uncertainties (<0.1%).

4.2.2. Gouy phase broadening. Gouy correction leads to <1% change of the pulse duration and does not have to be considered.

4.2.3. eTOF spectrometer resolution, acceptance angle and signal to noise ratio (SNR). The maximum streaking field strength has to be adjusted to provide sufficient streaking strength to clearly broaden the photoelectron peaks in comparison to the reference width. This allows one to determine the actual XUV pulse shape, while keeping the signal level still large enough within the time bins of the eTOF signal. If the streaked photoelectron line is broadened too much, there are only few electrons per time bin left leading to a large Poisson uncertainty and thus a large error in the determination of the pulse shape.

We found that 30–40 electrons contributing to the maximum signal are sufficient to reduce the error for the signal amplitude to <20%. Figure 7 shows the retrieved XUV pulses including the statistical error bands.

4.2.4. Influence of the non-linearities of the THz vector potential. The reconstruction of the XUV pulse shape from the measured photoelectron distribution needs to take the measured vector potential into account if the pulses cover large parts of the slope. The XUV pulses were reconstructed using
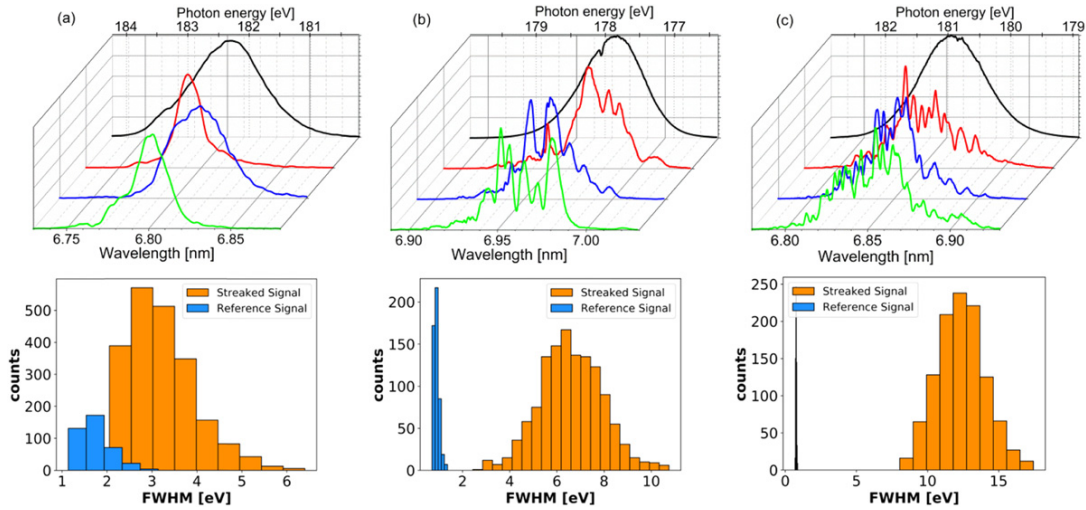
Figure 6. Upper row: XUV spectra for different pulse duration settings. Column (a): represents the case $\tau_{\mathrm{XUV}} < 30$ fs; (b): 30 fs $< \tau_{\mathrm{XUV}} <$ 150 fs; (c): $\tau_{\mathrm{XUV}} > 150$ fs. Green, blue and red lines are examples of single-shot spectra measured with the PG spectrometer. Black curves represent the average spectra. One can clearly see the different number of spectral spikes/modes for the different settings. The lower row shows the corresponding histograms for the eTOF spectral width (FWHM in eV) for streaked and un-streaked (reference) spectra. While for the long pulse duration (column (c)) the width fluctuations of the reference (un-streaked) spectra is negligible, for the short pulses (column (a)) there is a significant overlap showing the need of a careful consideration of the reference pulses.
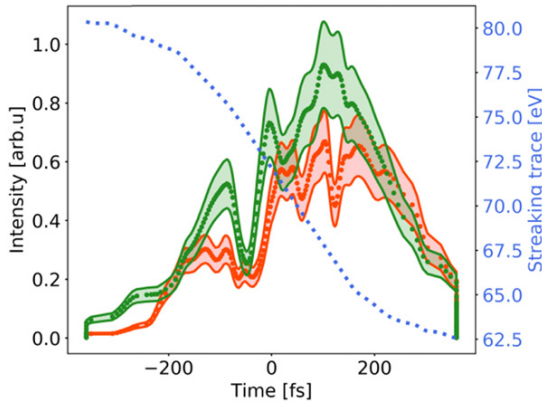

Figure 7. Reconstruction of the XUV pulse shape for pulses that are almost as long as the ramp of the THz vector potential. Red and green curves represent two examples of measured eTOF spectra with a pulse duration of ∼350fs (FWHM). The error envelope takes into account the statistical uncertainty. The dotted line represents the THz streaking trace. The streaking speed s was ∼0.043 eV fs^{-1}.

equation (10), taking the quantum mechanical nature of the interaction into account. In addition, the acceptance angle of the eTOF was included in the simulation. The differences in pulse reconstruction between the linear and nonlinear approaches are in the same range as the statistical errors (see figures 3 and 7).

4.2.5. SASE induced error sources. Using only one eTOF, no single-shot information about the chirp can be acquired. Unfortunately, the comparison of the pulse durations acquired from the positive and negative slope as shown in [19] is not applicable here since the XUV pulses are too long to be properly be measured by the 'shorter' side slope (see figure 1(c)).

4.3. Exploring the lower limit: 'short' ($\tau_{\mathrm{XUV}} < 30$ fs) XUV pulses

Up to date, higher frequency streaking fields in the infrared or near infrared ranges have been applied to measure XUV pulses down to attosecond pulse duration [43–45]. Shorter wavelength streaking fields usually provide more intense streaking strength while restricting the temporal window of the measurement. Thus, one has to be sure that both temporal jitter and the pulse duration are shorter than the streaking slope.

THz generation based on lithium niobate (LiNbO$_3$), centered around 0.6 THz with a field strength of ∼300 kV cm^{-1} (maximum achieved streaking speed s of ∼0.11 eV fs^{-1} in the THz focus), is ideally suited for the main working range of FLASH, providing XUV pulse durations of ∼30 fs to ∼150 fs (FWHM). The achievable streaking speed is rather low (as compared to e.g. IR streaking) and thus the ability to measure few fs pulse duration is rather poor. Nevertheless, we want to explore the resolution limit for measuring short pulse durations with the present setup.

In order to experimentally test the limits of the presented technique, we employed a new option of FLASH to produce sub 10 fs pulses [35]. As FLASH operates in the SASE mode, the generated XUV pulses consist of a stochastically fluctuating sequence of sub spikes [7, 40, 46]. Thus, the shortest pulse that can be generated by an SASE FEL without additional beam modulation is a single spike [35, 47]. Each temporal spike has a duration of roughly the coherence time τ_c. For the experimental wavelength of 6.8 nm, the coherence time is about 6 fs (FWHM) [35, 47]. Reference [35] provides a detailed description of how to achieve single mode operation at FLASH by using a dedicated photocathode laser with an about ten times shorter pulse duration as compared to the standard laser used. This configuration produces low charge
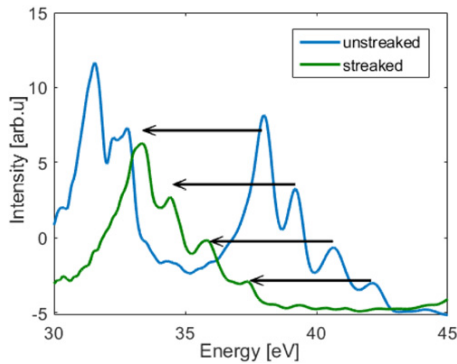
Figure 8. Measured Kr MNN-Auger spectra with (green) and without (blue) THz field.

Figure 9. Calculated photo- (blue) and Auger- (orange) electron emission rates assuming a Gaussian intensity distribution of the ionizing XUV pulse with an FWHM duration of 10 fs and a 7.9 fs Auger lifetime.

electron bunches (∼80 pC) that can be compressed to below 30 fs (FWHM) leading, in the nonlinear amplification process, to sub 10 fs XUV pulses. This results in strongly fluctuating XUV pulses with average pulse energies of about 1 μJ. Measurements of the XUV spectral distribution show that about 50% of the produced XUV pulses have only one single spectral spike. In the following section we present a detailed analysis of the error sources in pulse duration determination for such single spike short pulses.

4.3.1. Spectral fluctuations of the SASE pulse. Looking at figure 6(a) one notes that the width distributions of the reference spectra (no THz) and of the streaked spectra are partially overlapping. Thus, without a precise knowledge of the individual reference pulses the analysis is strongly limited.

In order to test the resolution of the streaking setup, we used the option of recording a high resolution XUV spectrum for each FEL pulse and a streaked electron spectrum simultaneously. To make sure that only the shortest XUV pulses are analyzed, we selected in a first step the XUV pulses showing only one single spectral peak and thus only one temporal spike. The spectral width of the single spike still varies in width by ±15% due to SASE fluctuations. The Fourier limit of the narrowest spikes was calculated to be below 5 fs (FWHM). To determine the resolution of the streaking setup, a selection of single spike pulses has been used while in general few spike pulses require iterative reconstruction algorithms to determine the most likely pulse duration shape [14, 48, 49].

Here, we also want to emphasize that there is an alternative approach which can be used to determine the small differences between streaked and un-streaked spectra for ultrashort pulses without the need of precise knowledge of the actual reference XUV-spectrum. If Auger lines are used for streaking, the analysis is independent of energy fluctuations of the incident XUV pulse. Any energetic shift of the streaked lines can directly be ascribed to a shift of the arrival time. In the present case, krypton MNN-Auger electrons emitted after ionization of the Kr 3d shell have been investigated. Figure 8 shows streaked and un-streaked Auger spectra. The Auger spectrum consists of several narrow lines. The line width is determined by the resolution of the electron spectrometer which was ∼1 eV. The
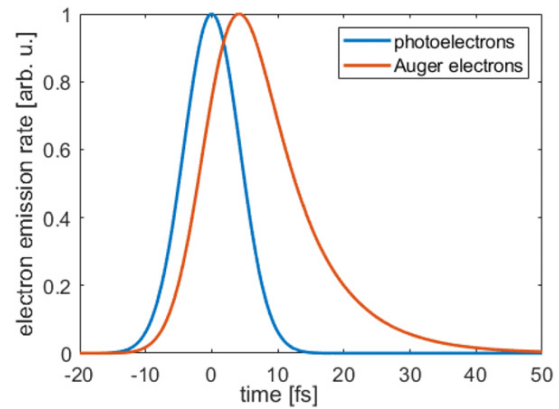
THz field shifts and broadens the spectra. The shift is proportional to the THz-vector potential at the instance of ionization and thus a measure for the chosen XUV/THz arrival time.

To determine the shortest XUV pulse durations within this approach we have again chosen XUV shots with only single modes in the simultaneously measured XUV-spectra. After averaging 50 spectra with the same relative XUV/THz arrival time, the widths of the streaked and un-streaked spectral lines were fitted by four Gaussian functions. After the deconvolution of the streaked and un-streaked spectra as in equation (3b) an FWHM duration of the Auger-electron emission of 10–15 fs has been determined whereby the streaking speed *s* was 0.05 eV fs^{-1}.

For Auger electrons the emission rate is not proportional to the XUV intensity profile but consists of a convolution of the XUV intensity distribution with the exponential Auger decay rate. In case of krypton the lifetime of the M-shell vacancy is 7.9 fs [50]. Plotted in figure 9 are calculated electron emission rates for direct photo- (blue) and krypton MNN-Auger-electrons (orange) ionized by an XUV pulse with Gaussian envelope and 10 fs FWHM duration. The FWHM width of the Auger emission is 15 fs and thus significantly larger than the XUV pulse duration.

However, since the Auger-lifetime is well known it is possible to reconstruct the XUV pulse duration from the measured Auger emission rates. The here observed FWHM Auger emission widths of 10–15 fs correspond to XUV pulse durations of 5–10 fs which is in good agreement with the values inferred from spectral analysis and photoelectron streaking.

4.3.2. Gouy phase broadening. For the short XUV pulses, the Gouy broadening is on the order of the pulse duration and thus of uttermost importance. Here the uncertainty of the knowledge of the Gouy phase has a severe impact on the error bars of the retrieved XUV pulse. In order to reduce the Gouy phase induced broadening, we moved the interaction point (eTOF spectrometer and gas source) out of the THz focus by ∼6 mm. The corresponding effective broadening is on the order of 10 fs (see table 1).
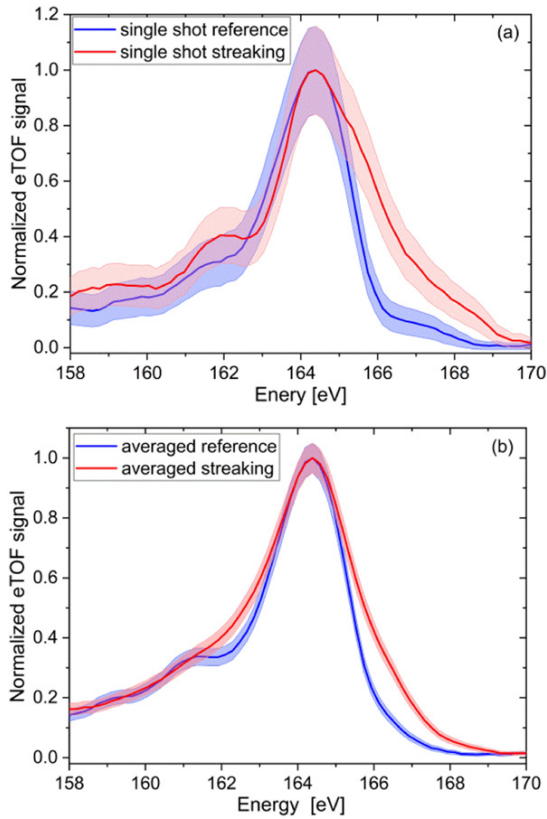
Figure 10. Streaked (red) and un-streaked (blue) photoelectron spectra are shown (thick lines) including the $1/\sigma$ error bars (shaded area) caused by the Poisson statistics due to the limited number of electrons in the spectrum. (a) A single-shot spectra for an XUV pulse containing single spectral spike (wavelength 6.8 nm). (b) The average over ten streaked and ten reference pulses from similar single spectral spike pulses. The streaking speed s was 0.09 eV fs^{-1}.

4.3.3. eTOF spectrometer resolution, acceptance angle and signal to noise ratio (SNR). To determine the small differences between the streaked and un-streaked spectra the Poisson statistics is very important to be considered. In order to keep the signals below the space charge limit, the signal amplitude of the individual pulses was on the order of 100–200 electrons leading to the contribution of about 40–80 electrons in the peak of the signal. Figure 10(a) shows the rather large error bars ($>15\%$) for a single shot spectrum (red: streaked, blue: reference). As one can see, the reference and streaked confidence bands overlap. Thus, for single-shot spectra the uncertainty of the pulse duration measurement is on the order of 100% due to counting statistics.

Having the set of sorted data as described above we can average 10 spectra leading to a $\sim$3 times smaller error due to Poisson statistics. The confidence bands shrink to a level that the pulse duration can be determined with $<50\%$ error.

For ultra-short pulses the angular acceptance of the eTOF spectrometer has to be taken into account as well. Figure 2 shows that only spectra measured at the zero-crossing of the vector potential are not affected for eTOF spectrometers having a large collection angle, while additional broadening is

observed for delay times far away from the zero-crossing. Indeed, after correcting for the different eTOF resolutions at different kinetic energies and streaking strength, we see a slight trend of broader spectra as the delay is moved away from the zero-crossing. The effect is however within the error bars.

4.3.4. Influence of the non-linearity of the vector potential. Since the streaking for ultrashort pulses uses only a small fraction of the streaking slope, the linear approximation of the streaking slope is sufficient.

4.3.5. SASE chirp. For the present setup the resolution is not good enough to tell anything about the chirp of singles-spike XUV SASE pulses.

In summary, the main limiting factors of the present streaking setup at the short pulse limit are the counting statistics and the uncertainty in the knowledge of the Gouy phase broadening. Summarizing the errors discussed above we can state that a measured pulse duration for the single-shot single spectral spike SASE pulses (at 6.8 nm) relying on the streaking data is $10\ \mathrm{fs}^{+7\ \mathrm{fs}}_{-10\ \mathrm{fs}}$. Using the Fourier limit derived from the spectral information as additional constrain (the lower bound is more confined), we can state for a single shot measurement $10\ \mathrm{fs}^{+7\ \mathrm{fs}}_{-7\ \mathrm{fs}}$. By averaging pulses with similar XUV spectra we can reduce the pulse duration value and the error range to $8\ \mathrm{fs}^{+4\ \mathrm{fs}}_{-4\ \mathrm{fs}}$ [35].

5. Conclusion

Terahertz-field-driven streaking is a powerful tool for measuring the duration and (to a certain extent) time-structure of ultrashort XUV pulses on a single-shot basis. We investigated the applicability of the method by using the large parameter range of FLASH delivering pulse durations from $\sim$10 fs to $\sim$350 fs at different XUV wavelengths.

We show that the streaking technique relying on laser based THz generation in LiNbO$_3$, yielding a field strength of 300 kV cm^{-1}, is ideally suited to measure the pulse duration in the range of 30 fs to 150 fs with an overall precision of typically $\pm20\%$. The individual error contributions are discussed in detail. In addition, for the precise analysis of the spectra and the simulation of the influence of different parameters, the theoretical description of the streaking process based on quantum mechanical principles is presented. Here, a novel approximation of the common SFA approach allows the fast reconstruction of XUV pulses from measured photoelectron spectra including the angular distribution of the photoelectrons as well as the nonlinear vector potential of the streaking field.

To determine the limits of the method we explored the long pulse limit where the XUV pulses extend over essentially the whole streaking slope, as well as sub-10 fs pulses to determine the resolution limit. In the present setup, pulse durations down to about 20 fs can be measured reliably while for even shorter pulses higher streaking fields are required. In principle, this can be achieved using higher THz frequencies [20] or even using IR radiation [45]. However, in this range the jitter between THz (IR) and XUV easily becomes larger than the streaking slope and new methods have to be applied [48].

Acknowledgments

ORCID iDs

Rosen Ivanov ⬡ https://orcid.org/0000-0002-6716-5104
Jia Liu ⬡ https://orcid.org/0000-0003-0073-4998
Nikolay M Kabachnik ⬡ https://orcid.org/0000-0003-4458-7643
Stefan Düsterer ⬡ https://orcid.org/0000-0003-4379-1327

References

[1] Ackermann W *et al* 2007 *Nat. Photon.* **1** 336
[2] Emma P *et al* 2010 *Nat. Photon.* **4** 641
[3] Ishikawa T *et al* 2012 *Nat. Photon.* **6** 540
[4] Allaria E *et al* 2012 *Nat. Photon.* **6** 699
[5] Kang H S *et al* 2017 *Nat. Photon.* **11** 708
[6] Milne C J *et al* 2017 *Appl. Sci.* **7** 720
[7] Saldin E L, Schneidmiller E A and Yurkov M V 2000 *The Physics of the Free Electron Laser* (Berlin: Springer)
[8] Krinsky S and Gluckstern R L 2003 *Phys. Rev. STAB* **6** 050701
[9] Düsterer S *et al* 2014 *Phys. Rev. STAB* **17** 120702
[10] Riedel R *et al* 2013 *Nat. Commun.* **4** 1731
[11] Maltezopoulos T *et al* 2008 *New J. Phys.* **10** 033026
[12] Behrens C *et al* 2014 *Nat. Commun.* **5** 3762
[13] Saldin E L, Schneidmiller E A and Yurkov M V 2010 *Phys. Rev. STAB* **13** 030701
[14] Frühling U *et al* 2009 *Nat. Photon.* **3** 523
[15] Grguras I *et al* 2012 *Nat. Photon.* **6** 852
[16] Gorgisyan I *et al* 2017 *Opt. Express* **25** 2080
[17] Juranić P N *et al* 2014 *Opt. Express* **22** 30004
[18] Ivanov R, Liu J, Brenner G, Brachmanski M and Düsterer S 2018 *J. Synchrotron Radiat.* **25** 26
[19] Azima A *et al* 2018 *New J. Phys.* **20** 013010
[20] Hoffmann M C *et al* 2018 *New J. Phys.* **20** 033008
[21] Frühling U 2011 *J. Phys. B: At. Mol. Opt. Phys.* **44** 243001
[22] Keldysh L V 1965 *Sov. Phys. -JETP* **20** 1307
[23] Kazansky A K, Sazhina I P and Kabachnik N M 2010 *Phys. Rev. A* **82** 033420
[24] Itatani J, Quéré F, Yudin G L, Ivanov M Y, Krausz F and Corkum P B 2002 *Phys. Rev. Lett.* **88** 173903
[25] Itatani J, Quéré F, Yudin G L and Corkum P B 2004 *Laser Phys.* **14** 344
[26] Kazansky A K, Sazhina I P and Kabachnik N M 2019 *Opt. Express* **27** 12939
[27] Gerasimova N, Dziarzhytski S and Feldhaus J 2011 *J. Mod. Opt.* **58** 1480
[28] Martins M *et al* 2006 *Rev. Sci. Instrum.* **77** 115108
[29] Redlin H *et al* 2011 *Nucl. Instrum. Methods Phys. Res.* A **635** 88
[30] Schulz S *et al* 2015 *Nat. Commun.* **6** 5938
[31] Hebling J *et al* 2002 *Opt. Express* **10** 1161
[32] Radcliffe P *et al* 2007 *Nucl. Instrum. Methods Phys. Res.* A **583** 516
[33] Thompson A *et al* 2009 *X-Ray Data Booklet* (Berkeley, CA: University of California)
[34] Oelze T *et al* 2020 *Opt. Express* **28** 20686–703
[35] Rönsch-Schulenburg J *et al* 2020 unpublished
[36] Jurvansuu M, Kivimäki A and Aksela S 2001 *Phys. Rev. A* **64** 012502
[37] Braune M *et al* 2018 *J. Synchrotron Radiat.* **25** 15
[38] Li Y, Lewellen J, Huang Z, Sajaev V and Milton S V 2002 *Phys. Rev. Lett.* **89** 234801
[39] Ferrario M *et al* 2012 *Appl. Phys. Lett.* **101** 134102
[40] Krinsky S and Huang Z 2003 *Phys. Rev. STAB* **6** 050702
[41] Saldin E L, Schneidmiller E A and Yurkov M V 2006 *Phys. Rev. STAB* **9** 050702
[42] Bermudez I *et al* 2020 *Phys. Rev. STAB* accepted
[43] Drescher M, Hentschel M, Kienberger R, Tempea G, Spielmann C, Reider G A, Corkum P B and Krausz F 2001 *Science* **291** 1923
[44] Gaumnitz T, Jain A, Pertot Y, Huppert M, Jordan I, Ardana-Lamas F and Wörner H J 2017 *Opt. Express* **25** 27506
[45] Helml W *et al* 2017 *Appl. Sci.* **7** 915
[46] Pfeifer T, Jiang Y, Düsterer S, Moshammer R and Ullrich J 2010 *Opt. Lett.* **35** 3441
[47] Roling S *et al* 2011 *Phys. Rev. STAB* **14** 080701
[48] Hartmann N *et al* 2018 *Nat. Photon.* **12** 215
[49] Heider R *et al* 2019 *Phys. Rev. A* **100** 053420
[50] Drescher M *et al* 2002 *Nature* **419** 803

A.2 Study of temporal, spectral, arrival time and energy fluctuations of SASE FEL pulses

Study of temporal, spectral, arrival time and energy fluctuations of SASE FEL pulses

IVETTE J. BERMÚDEZ MACIAS,[1] **STEFAN DÜSTERER,**[1,*] **ROSEN IVANOV,**[1] **JIA LIU,**[2] **GÜNTER BRENNER,**[1] **JULIANE RÖNSCH-SCHULENBURG,**[1] **MARIE K. CZWALINNA,**[1] **AND MIKHAIL V. YURKOV**[1]

[1]*Deutsches Elektronen-Synchrotron, Notkestrasse 85, D- 22603 Hamburg, Germany*
[2]*European XFEL GmbH, Holzkoppel 4, D- 22869 Schenefeld, Germany*
*stefan.duesterer@desy.de

Abstract: Self-amplified spontaneous emission (SASE) pulses delivered by free electron lasers (FELs) are inherently fluctuating sources; each pulse varies in energy, duration, arrival time and spectral shape. Therefore, there is strong demand for a full characterization of the properties of SASE radiation, which will facilitate more precise interpretation of the experimental data taken at SASE FELs. In this paper, we present an investigation into the fluctuations of pulse duration, spectral distribution, arrival time and pulse energy of SASE XUV pulses at FLASH, both on a shot-to-shot basis and on average over many pulses. With the aid of simulations, we derived scaling laws for these parameters and disentangled the statistical SASE fluctuations from accelerator-based fluctuations and measurement uncertainties.

1. Introduction

Free-electron lasers (FELs) working in the extreme ultraviolet (XUV) and X-ray region deliver photon pulses with few-femtosecond (fs) duration and unrivalled intensity [1–7]. The majority of X-ray FELs operate in the self-amplified spontaneous emission (SASE) regime, meaning that each pulse is characterized by a unique combination of pulse energy, XUV spectrum, arrival time and pulse duration (see e.g. Figure 1). For a detailed analysis of experimental data taken during FEL experiments it is essential to determine as many SASE pulse radiation properties as possible, at best on a shot-to-shot basis. A variety of pulse-resolved methods have been developed and are used to determine, e.g. the pulse energy [8,9], the spectral distribution [10,11] and arrival time of the electron bunches [12], but the XUV pulse duration still lacks a standard detection scheme. Providing accurate pulse length information would enable experimentalists to sort their experimental data according to all pulse properties. Furthermore, it would allow one to identify whether there are correlations between different parameters, such as pulse energy and duration. So far, many studies have examined the fluctuations in pulse energy [13–17] or XUV spectrum [17–21] separately. Due to the shortcomings of available pulse-resolved XUV pulse duration diagnostics, the influence of the SASE process on the temporal properties and the dependence of other parameters on the pulse duration have yet to be investigated in detail. In this paper, we present pulse-resolved measurements of the XUV pulse duration at the free-electron laser FLASH in Hamburg [1], achieved using THz streaking [22–24], in addition to measurements of the XUV spectrum and pulse energy of all individual pulses. The fluctuation of these parameters, as well as the correlations and dependencies between them are studied. Furthermore, simulations using a fast three dimensional, time-dependent simulation code FAST [25] and the partial coherence method [26], support our experimental findings and are used to disentangle the influence of the physics of the SASE process and its fluctuations from measurement uncertainties.
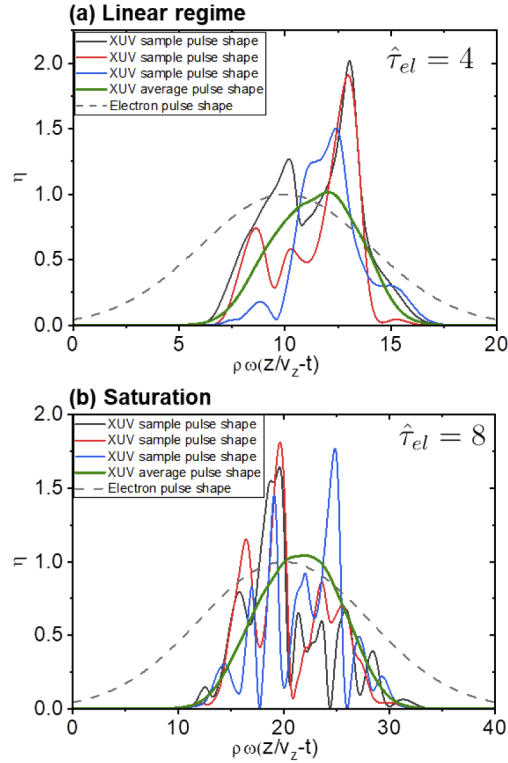
Fig. 1. The temporal distribution of a SASE pulse is illustrated with a simulation result using FAST. The x-axis, is the scaled time coordinate along the bunch where v_z is the longitudinal velocity of the electrons. Fig. (a) shows photon pulses generated in the linear regime ($\hat{\tau}_{el} = 4$) and Fig. (b) at the onset of saturation ($\hat{\tau}_{el} = 8$) . The dashed line denotes the electron bunch pulse shape.

A theoretical overview of the statistical properties of the SASE FEL radiation, as well as the methods and results of the numerical simulations, are presented in Sec 2. The experimental setup is described in Sec 3. In Sec 4 we discuss the experimental results and compare them to simulations. Furthermore, the average and shot-to-shot fluctuations of the FEL photon pulse duration, energy, and arrival time are presented in Sec 4.

2. Statistical properties of the SASE FEL radiation

The amplification process in a SASE FEL develops from the shot noise in the electron beam, and amplifies a narrow band of density modulations around the resonance wavelength $\lambda = \lambda_u(1 + K^2)/(2\gamma^2)$. In the one-dimensional model's framework, the operation of a SASE FEL is described by the FEL parameter ρ and the number of cooperating electrons N_c [13,27] in the SASE process:

$$\rho = \left[\frac{\lambda_u^2 j_0 K^2 A_{JJ}^2}{16\pi I_A \gamma^3} \right]^{1/3} , \qquad N_c = I/(e\rho\omega) , \tag{1}$$

where γ is the relativistic factor, j_0 is the beam current density, $I_A = mc^3/e \simeq 17$ kA, K is the rms undulator parameter, and λ_u is the undulator period. The coupling factor is $A_{JJ} = 1$ for a helical undulator, and $A_{JJ} = [J_0(Q) - J_1(Q)]$ with $Q = K^2/[2(1 + K^2)]$ for a planar undulator. I is the electron bunch current and ω the frequency of the amplified wave.

In this section, we assume that the electron bunch has a Gaussian longitudinal profile and its rms pulse duration is τ_{el}. We extend the results of Refs. [14,17] by in addition studying the statistical properties of the photon pulse duration and arrival time. We perform a series of numerical simulations of the FEL process using the simulation code FAST [25] for a wide range of electron bunch durations τ_{el}, and trace the FEL amplification process from the start-up of the shot noise to the deep nonlinear regime. Then, we apply similarity techniques [13] to the results of the numerical simulations and derive general statistical properties of the radiation.

The output of a specific simulation run is an array of radiation fields $\tilde{E}(t)$, from which we can calculate the temporal profile of the radiation power $P(t) \propto |\tilde{E}(t)|^2$ and the radiation pulse energy $E_r = \int P(t)dt$ as shown in Fig. 1. The center of mass of the photon pulse, which we also associate with the photon pulse arrival time τ_{ar}, and its rms duration τ_{ph} are derived from numerical simulations as follows:

$$\tau_{ar} = \frac{\int tP(t)\mathrm{d}t}{E_r} \, , \qquad \tau_{ph}^2 = \frac{\int (t - \tau_{ar})^2 P(t)\mathrm{d}t}{E_r} \, . \tag{2}$$

The energy, duration, and arrival time of the radiation pulses fluctuate from shot-to-shot. These fluctuations can be described with their standard deviations:

$$\sigma_{ph}^2 = \langle (\tau_{ph} - \langle \tau_{ph} \rangle)^2 \rangle \, ,$$
$$\sigma_{ar}^2 = \langle (\tau_{ar} - \langle \tau_{ar} \rangle)^2 \rangle \, , \tag{3}$$
$$\sigma_E^2 = \langle (E_r - \langle E_r \rangle)^2 \rangle / \langle E_r \rangle^2 \, .$$

As a next step of the analysis, applying similarity techniques, we translate the results of a specific numerical simulation onto a map of physical parameters [13]. The typical temporal scaling factor in FEL physics is the coherence time τ_c, defined as $\tau_c = \int |\gamma_c(t)|^2 dt$, with γ_c as the complex degree of coherence [28]. On the other hand, the relevant scaling parameter for the variables having a dimension of time is $\rho\omega$ leading to the following dimensionless expressions (the relation to experimental parameters can be found in Table 1):

$$\hat{\tau}_{el} = \rho\omega\tau_{el} \, , \qquad \hat{\tau}_{ph} = \rho\omega\tau_{ph} \, ,$$
$$\hat{\sigma}_{ar} = \rho\omega\sigma_{ar} \, , \qquad \hat{\sigma}_{ph} = \rho\omega\sigma_{ph} \, . \tag{4}$$

Table 1. The table shows the relation between normalized electron pulse durations $\hat{\tau}_{el}$, that were used in the simulation and the corresponding expected XUV pulse durations in fs (FWHM) at the onset of saturation. Note that $\hat{\tau}_{el}$ is equivalent to the number of modes M (for $\hat{\tau}_{el}>2$). τ_{ph} was calculated according to Eq. (9). We used $\tau_{cFWHM}(6.8\text{nm}) \sim 6$ fs and $\tau_{cFWHM}(20\text{nm}) \sim 15$ fs (FWHM).

$\hat{\tau}_{el}$ | M	$\tau_{ph,FWHM}(6.8nm)$	$\tau_{ph,FWHM}(20nm)$
4	17 fs	40 fs
8	35 fs	85 fs
16	70 fs	170 fs
32	140 fs	340 fs

Then scaling the parameters with the normalized electron pulse duration $\hat{\tau}_{el}$, we obtain:

$$\bar{\tau}_{ph} = \tau_{ph}/\tau_{el} \, , \qquad \bar{\sigma}_{ph} = \hat{\sigma}_{ph}/\hat{\tau}_{el}^{1/2} \, ,$$
$$\bar{\sigma}_{ar} = \hat{\sigma}_{ar}/\hat{\tau}_{el}^{1/2} \, , \qquad \bar{\sigma}_E = \sigma_E \hat{\tau}_{el}^{1/2} \, , \tag{5}$$
$$\bar{\eta} = E_r/(\rho E_{eb}) \, ,$$

where E_{eb} is the kinetic energy of the electron bunch.

Figure 2 shows the evolution of the main characteristics of the SASE FEL electron and radiation pulse along the undulator. Using Eq. (5), the average values and fluctuations of the electron pulse energy and duration, as well as the arrival time of the radiation pulses' fluctuations, are shown. For radiation pulse durations $\hat{\tau}_{\mathrm{el}} \gtrsim 4$, the scaled parameters (5) show a common behavior. The longitudinal coordinate z along the undulator in Fig. 2 is scaled to the saturation length z_{sat} [13,29]:

$$z_{\mathrm{sat}} \simeq \frac{\lambda_{\mathrm{u}}}{4\pi\rho}\left(3 + \frac{\ln N_{\mathrm{c}}}{\sqrt{3}}\right), \qquad \tau_{\mathrm{c}}^{\mathrm{sat}} \simeq \frac{1}{\rho\omega}\sqrt{\frac{\pi \ln N_{\mathrm{c}}}{18}}. \tag{6}$$
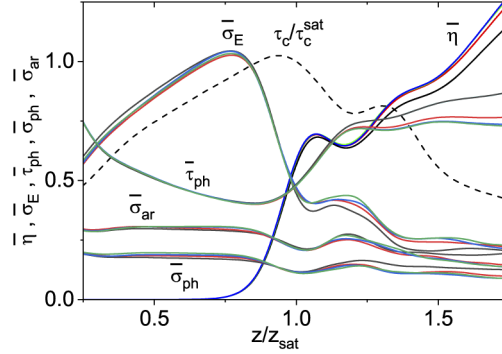

Fig. 2. Evolution along the undulator of the scaled FEL efficiency $\bar{\eta}$, scaled rms fluctuations of the radiation pulse energy $\bar{\sigma}_{\mathrm{E}}$, scaled rms photon pulse duration and its scaled rms deviation, $\bar{\tau}_{\mathrm{ph}}$ and $\bar{\sigma}_{\mathrm{ph}}$, as well as the scaled rms deviation of the photon pulse arrival time $\bar{\sigma}_{\mathrm{ar}}$. The notations of the scaled parameters are given by Eq. (5). The black, red, blue and green curves correspond to the normalized electron pulse durations $\hat{\tau}_{\mathrm{el}}$ of 4, 8, 16, and 32, respectively. The dashed line shows the coherence time scaled to the coherence time at saturation. The calculations are plotted as function of the undulator coordinate z normalized by the saturation length z_{sat}. Thus, values $z/z_{\mathrm{sat}}<0.8$ denote the linear regime while $z/z_{\mathrm{sat}} = 1$ is the saturation point.

The brilliance of the radiation, which is proportional to the product of the radiation power and the coherence time, reaches a maximum value at the saturation point. The coherence time at the saturation point $\tau_{\mathrm{c}}^{\mathrm{sat}}$ is given by Eq. (6). It grows at a rate of $z^{1/2}$ in the exponential gain regime (also called linear regime), reaches a maximum value just before saturation, and gradually drops down in the post-saturation regime [13,30].

The maximum of the energy fluctuations and minimum of the radiation pulse duration are obtained at the end of the exponential gain regime, at about 0.8 of the saturation length. The radiation from a SASE FEL operating in the linear regime holds properties of completely chaotic polarized light [13,30], and the probability distribution of the radiation energy E_{r} is a gamma-distribution [30]:

$$p(E_{\mathrm{r}}) = \frac{M^M}{\Gamma(M)}\left(\frac{E_{\mathrm{r}}}{\langle E_{\mathrm{r}}\rangle}\right)^{M-1}\frac{1}{\langle E_{\mathrm{r}}\rangle}\exp\left(-M\frac{E_{\mathrm{r}}}{\langle E_{\mathrm{r}}\rangle}\right), \tag{7}$$

where $\Gamma(M)$ is the Gamma-function. The physical meaning of M is that it is equal to the total number of modes (longitudinal and transverse) in the radiation pulse. It is connected to the fluctuations of the radiation pulse energy by the relation $M = 1/\sigma_E^2$. Furthermore, at the onset of saturation, M essentially equals the normalized electron pulse duration $\hat{\tau}_{\mathrm{el}}$ (for $M>2$) as shown in Ref. [17].

The radiation of the SASE FEL at the initial stage of the amplification consists of a large number of transverse and longitudinal modes. The number of longitudinal modes is defined by

the fluctuations of the radiation pulse energy filtered with a pin hole, and it is improved along the amplification process, resulting in a reduction of the number of longitudinal modes. The transverse mode selection process leads to a suppression of the higher transverse radiation modes. As a result, primarily the fundamental transverse mode dominates in the high-gain linear regime for diffraction-limited electron beams. This feature makes the one-dimensional model applicable for the description of FELs like FLASH.

A practical estimate for the minimum rms radiation pulse duration at the end of the high-gain linear regime is [16,17]:

$$\tau_{\mathrm{ph}}^{\mathrm{min}} \simeq 0.4\tau_{\mathrm{el}} \simeq \frac{M\lambda z_{\mathrm{sat}}}{15c\lambda_{\mathrm{u}}} \simeq \frac{M\tau_{\mathrm{c}}^{\mathrm{sat}}}{4} \ . \tag{8}$$

The lengthening of the radiation pulse occurs when the amplification process enters the nonlinear regime. This happens due to the electron bunch tails lasing into saturation and the slippage effect. The latter is more pronounced for shorter pulses, as illustrated in Fig. 2. At the saturation point, the lengthening is about a factor of 1.2 greater with respect to the minimum pulse length given by Eq. (8), and it increases up to a factor of 1.8 in the post-saturation regime. To compare these results to the experimentally determined data, a scaling of Eq. (8) to full width half maximum (FWHM) is helpful:

$$\tau_{\mathrm{ph_{FWHM}}}^{\mathrm{sat}} \simeq 0.7M\tau_{\mathrm{c_{FWHM}}}^{\mathrm{sat}} \tag{9}$$

using the experimentally easier accessible FWHM of the coherence time which is linked to $\tau_{\mathrm{c}}^{\mathrm{sat}}$ by $\tau_{\mathrm{c_{FWHM}}}^{\mathrm{sat}} = 2\sqrt{\ln 2/\pi} \times \tau_{\mathrm{c}}^{\mathrm{sat}} \sim 0.94 \times \tau_{\mathrm{c}}^{\mathrm{sat}}$ [28].

In addition, the relation between the number of spikes (N_{spect}) present in the spectral distribution and the number of modes is important for the analysis of the experimental data. Following the argumentation in Ref. [31] we obtain the relation:

$$N_{\mathrm{spect}} \sim 0.7M. \tag{10}$$

Looking at Fig. 3 the following scaling of the pulse duration fluctuation can be deduced:

$$\frac{\sigma_{\mathrm{ph}}}{\tau_{\mathrm{ph}}} \simeq \frac{\alpha_{\mathrm{ph}}}{\sqrt{\hat{\tau}_{\mathrm{el}}}} \simeq \frac{\alpha_{\mathrm{ph}}}{\sqrt{M}} \tag{11}$$

with the scaling parameter α_{ph} ranging between 0.4 for the linear regime and 0.2 in saturation. Equivalently, for the pulse arrival time fluctuation we obtain:

$$\frac{\sigma_{\mathrm{ar}}}{\tau_{\mathrm{ph}}} \simeq \frac{\alpha_{\mathrm{ar}}}{\sqrt{\hat{\tau}_{\mathrm{el}}}} \simeq \frac{\alpha_{\mathrm{ar}}}{\sqrt{M}} \tag{12}$$

with $\alpha_{\mathrm{ar}} \sim 0.7$ for the linear regime and $\alpha_{\mathrm{ar}} \sim 0.4$ in saturation.

The ratio $\sigma_{\mathrm{ph}}/\sigma_{\mathrm{ar}} \simeq 0.6$ remains nearly constant for all the stages of the amplification process. Thus, the SASE induced fluctuation of the arrival time (movement of the centroid) is about twice as large compared to the fluctuations of the pulse duration itself. This has important consequences for high precision pump-probe experiments where the arrival time of the applied pulses has to be known precisely.

Figure 4 shows the correlation plots of the photon pulse duration versus the radiation pulse energy for several thousand simulation runs. A clear correlation is visible in the high-gain linear regime where *shorter* pulses contain *more* energy while for saturation and post-saturation there is no significant correlation as will be discussed in the next section.

In addition to the advanced simulation of the actual SASE process, a very simple but powerful approach based on the *partial coherence model* introduced in Ref. [26] was used to determine to what extent this model agrees with the experiments. This method generates a random spectral
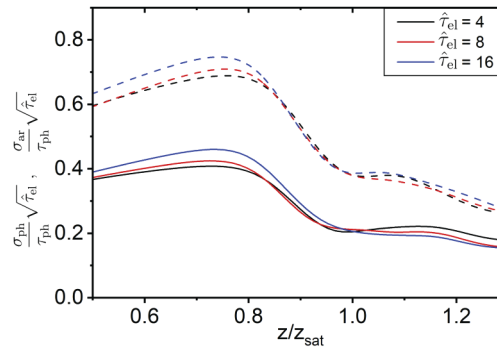
Fig. 3. Shown is the evolution of the fluctuations normalized on the pulse duration for the pulse arrival time $\sigma_{ar}/<\tau_{ph}>$ and pulse duration $\sigma_{ph}/<\tau_{ph}>$ scaled with the normalized electron pulse duration $\sqrt{\hat{\tau}_{el}}$. The plot reflects how the fluctuations decrease as saturation is reached. Pulse arrival time fluctuations dominate over the pulse duration fluctuations. The three different colors of the curves correspond to the different normalized electron pulse durations $\hat{\tau}_{el} = 4$, 8 and 16.
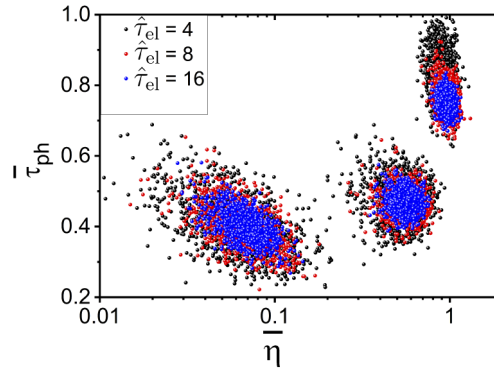

Fig. 4. Correlation plot of the scaled rms photon pulse duration $\bar{\tau}_{ph}$ versus the scaled photon pulse energy $\bar{\eta}$. Black, red and blue colors correspond to the normalized electron pulse durations $\hat{\tau}_{el} = 4$, 8 and 16. The left area of the plot corresponds to the high-gain linear regime ($z = 0.8 \times z_{sat}$), where a negative slope can be observed predicting shorter pulses at larger pulse energies. The middle and right areas correspond to the saturation, and deep nonlinear regime ($z = 1.5 \times z_{sat}$), where no correlation is found (compare with Fig. 2). The notations of scaled parameters are given by Eq. (5).

phase and amplitude distribution at different sample frequencies which are used to create an initial electric field. This field is "filtered" with the (measured) average spectral distribution of the FEL. After a Fourier transform, this leads to a series of coherent spikes in the time domain, which, in a second step, is folded with the desired average pulse duration shape, restricting the electric field to the finite pulse duration. This step finally leads to the characteristic spectral spikes after a second Fourier transform back to the spectral domain. The new filtered electric field will be partially coherent as it is delimited by the known FEL pulse duration and average spectrum and will be different for each random choice of the spectral phase function. Using this approach, one can easily provide a large set of simulated SASE-like pulse distributions to model SASE FEL experiments.

3. Description of experiment

The experiments were performed at the plane grating (PG) beamline [32] of FLASH. For the experiments described here, the PG beamline was operated in so called parallel configuration. This special mode enables the utilization of the zero order of the FEL photon beam (at the PG0 beamline branch) for the pulse length diagnostic based on THz streaking [24], while the dispersed radiation is simultaneously used in the PG2 beamline to measure the FEL spectrum with high resolution [33]. This configuration was used for the presented measurement in order to acquire the maximum amount of information about the XUV SASE pulses.

Various settings of the accelerator were used to provide a large range of different radiation pulse properties. The electron bunch charges were altered from 0.08 nC up to 0.44 nC leading to different XUV pulse durations as well as to XUV pulse energies ranging between only few μJ to > 100 μJ per XUV pulse. FLASH was tuned to a wavelength of 6.8 nm (180 eV) and for a second set of measurements to 20 nm (62 eV).

The FEL was operated in single bunch mode at 10 Hz. To generate single-cycle THz pulses, the near-infrared (NIR) pump-probe laser system at FLASH [34] was used. This Ti:sapphire laser delivers ~100 fs (FWHM) pulses with 6.5 mJ pulse energy at a central wavelength of 800 nm and a repetition frequency of 10 Hz. The overall level of synchronisation between the NIR pulses and the XUV FEL pulses was on the order of few tens of fs jitter (FWHM) (for the description of the synchronization system see e.g. [35]). The THz streaking setup consists of an optical setup with beam size adaption, pulse front tilting, THz generation and transport to the interaction region as well as an UHV interaction chamber. An electron time-of-flight (TOF) with high collection efficiency (Kaesdorf ETF11) mounted on a 3D manipulator records the time-of-flight of photoelectrons upon XUV ionization of the rare gas atoms target. A detailed description of the setup and measurement procedures are presented in Refs. [24,36].

Using the current THz streaking setup it was not possible to resolve the pulse sub structure, e.g the individual longitudinal modes of the pulse. The instrument broadening resulted in a Gaussian photoelectron distribution. The measured photoelectron line was therefore fitted using a Gaussian distribution.

The streaking measurements are rather complex and thus the measurement uncertainty depends on various parameters, which are described in detail in [36]. Generally, an error bar of $\pm$ 20% is in good agreement with the detailed investigations.

In addition to the XUV pulse duration and the XUV spectrum, the shot-to-shot pulse energy was recorded simultaneously using a transparent pulse energy monitor [8,9] located upstream of the THz-streaking setup and the PG beamline as well as the electron bunch arrival time [12].

4. Results and discussion - Characterization of SASE radiation

FLASH is a very versatile free-electron laser, able to deliver radiation across a wide range of wavelengths and pulse durations. Using these opportunities we could experimentally determine dependencies between XUV pulse duration, XUV spectral distribution and XUV pulse energy for many thousands of pulses and different machine settings, as will be shown in this section.

4.1. Fluctuations of the radiation pulse duration

The single-shot SASE XUV pulse duration derived from the THz streaking measurements reveals large fluctuations from shot-to-shot as shown in Fig. 5(a). The pulse duration from one pulse to the next can change by a factor of two to three. Likewise, the pulse energy and arrival time show strong fluctuations as presented in Fig. 5(b). These are the fluctuations experiments must cope with in the course of analyzing and interpreting the measured data. In addition, Fig. 5 emphasizes the need for an online pulse-resolved photon diagnostic of the radiation parameters at SASE FELs. An interesting question arises: What is the actual source of the fluctuations -
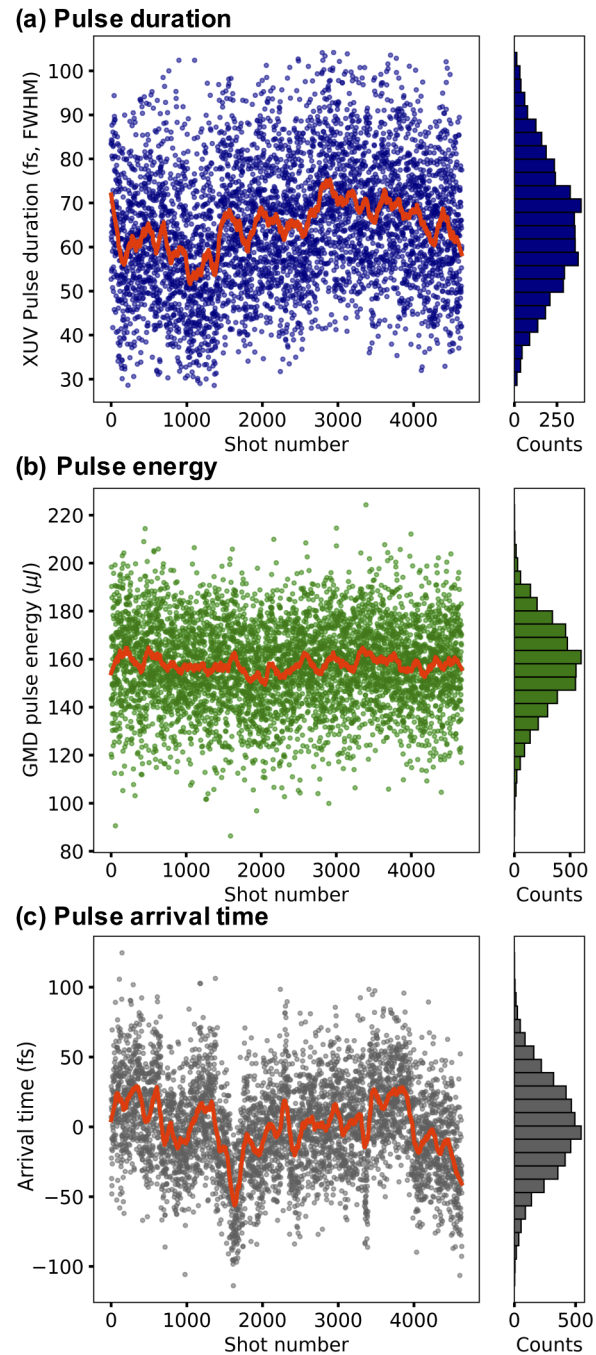
Fig. 5. The plots show how the measured XUV pulse duration (a), energy (b) and arrival time (c) fluctuate from pulse to pulse for around four thousand FLASH pulses. The line indicates the mean value. Error bars (not shown) are on the order of 20 % for the pulse duration and <10% for the pulse energy measurements. The arrival time uncertainty measured by THz streaking was ∼ 20 fs. In addition, the histograms of the shown time series are shown.

SASE or technical fluctuations? To get information on the fluctuations source, simulations of the different FEL parameters that are only taking the SASE process into account are used to compare to the experimentally determined values. That way we can disentangle the fluctuations induced by inherent SASE fluctuations from measurement uncertainties, fluctuations in the energy gain and compression of the electron bunches (related to the acceleration field phase stability), that we summarize and refer to as "technical fluctuations".

As shown in Fig. 5 (a, right side), the histogram of the measured pulse durations has a Gaussian distribution, with its center of mass denoting the mean pulse duration width representing the shot-to-shot fluctuations. To compare the width of the distribution for different pulse duration settings of the FEL, we use the rms of the distribution normalized by the pulse duration (σ_{ph}/τ_{ph}).

Equation (11) shows that the relative fluctuations of the pulse duration depend on the number of spectral modes. Therefore, in order to compare the experimental values measured at 6.8 nm , 20 nm and the simulation, the measured pulse duration was converted to the number of modes using Eq. (9). The coherence times τ_c were taken from Ref. [37]: $\tau_{c_{\mathrm{FWHM}}}(6.8 \text{ nm}) \sim 6$ fs and $\tau_{c_{\mathrm{FWHM}}}(20 \text{ nm}) \sim 15$ fs as summarized in Table 1.

The relative pulse duration fluctuations determined by the THz streaking experiments are plotted in Fig. 6 (dots) together with the simulation results [Eq. (11)] for saturation (full line) and exponential gain regime (dashed line). The experimental data points are the average fluctuations for several thousand FEL pulses recorded for different FEL operation modes. The fluctuation decreases when increasing the pulse duration from ($\sigma_{\mathrm{ph}}/\tau_{\mathrm{ph}}$) $\sim 30\%$ for short pulses to $\sim 10\%$ for longer ones. Therefore, SASE delivers better defined pulse durations for longer pulses than for short pulses. The general trend can be understood by looking at the modal structure; short pulses consist only of a small number of modes/spikes, such that the relative change of ± 1 modes affect the pulse duration much stronger than for longer pulses consisting of many more modes.

Comparing the measured data with the predicted pure SASE fluctuations from the FAST simulation (see Fig. 6), we find that a large fraction of the fluctuations is due to the SASE process. However, 20-50 % of the fluctuations can be attributed to "technical sources". Since the FEL was operating close to or in saturation, the relevant simulation for comparison is that of the solid line. The error bars include the uncertainty of the single-shot pulse duration measurement as described in [36] but accelerator based fluctuations are not taken into account.

The identification and quantification of other sources of fluctuations will have to be addressed in future studies. Even if additional "technical" error sources will be minimized in future accelerators, the pulse duration fluctuations based on pure SASE are still significant. Looking at Fig. 1 the pulse shape and resulting intensity distribution changes much more from shot-to-shot than the rms width, which underlines the demand for a high resolution temporal diagnostic resolving the SASE substructure.

In order to test to what extent the partial coherence model simulation [26] can reproduce the predicted fluctuations, we generated a large set of XUV spectra and temporal distributions. Ensembles of 400 pulses were calculated for different pulse durations between 10 fs and 200 fs in combination with a range of spectral bandwidths from 0.2 % to 0.9 %. For each simulated pulse we derived the pulse duration using Eq. (2) and its number of modes by counting the spectral spikes and using Eq. (10). For each setting, the standard deviation over the 400 pulses was calculated and normalized by the average pulse duration. The result is plotted in Fig. 6 as orange diamonds. Despite the large variation of input parameters, the simulated fluctuations agree very well with the fluctuations for pulses at saturation as predicted by the FAST simulation. Since FLASH typically operates in saturation, we can conclude that the partial coherence model provides a simple scheme to simulate SASE pulses that resemble the theoretically expected scaling of the pulse duration fluctuations.
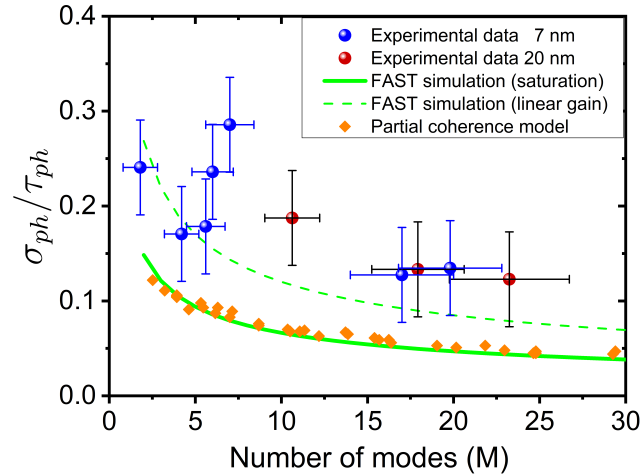
Fig. 6. The relative fluctuation of the SASE pulse durations are shown for the FAST simulation results as well as the experimentally measured values. The experimental pulse durations (for 6.8 nm and 20 nm) were scaled to number of modes using Eq. (9). The expected scaling of the fluctuations [(see Fig. 3 and Eq. (11)] are shown for the linear range and at saturation. In general, the relative fluctuations are decreasing for longer pulse durations while the experimental values (measured at saturation conditions) exceeding the simulation values indicating a significant contribution by technical fluctuations and drifts in the accelerator and measurement uncertainties of the THz streaking. In addition, the normalized fluctuations of 400 simulated pulses, calculated using the partial coherence method [26] are plotted.

4.2. Fluctuations of the radiation pulse energy

The pulse energy fluctuations can be treated analogously to the pulse duration fluctuations. As indicated in Fig. 2, the (relative) pulse energy fluctuations are larger compared to the pulse duration fluctuations and the difference between the linear gain and saturation regime is bigger as well.

Figure 7 summarizes the simulation results and the experimental data points. The experimental data lies between the predicted curves for the linear and the saturation regime. The pulse energy fluctuations of the experimental data are closer to the simulated ones, which is partly due to the much lower measurement uncertainty of typically $\pm(5-10)\%$ for pulse energy measurements [8,9]. Nevertheless, similar to the pulse duration fluctuations, a significant fraction of the fluctuations can be assigned to technical sources. Again, the partial coherence model agrees well with the FAST simulation for the saturation regime.

4.3. Fluctuations of the arrival time

Due to the varying sub-structure of the XUV pulse, the center of mass of the photon pulse (τ_{ar}) is slightly different from pulse to pulse, leading to fluctuations in the arrival time σ_{ar} of the photon pulse with respect to the electron bunch. To compare the prediction to the experimentally determined values we can use the arrival time of the center of mass of the electron bunch with respect to the master optical clock, which is measured at FLASH with high accuracy (~ 10 fs rms [12,35]) by the so called bunch arrival time monitor (BAM). In addition, the THz streaking arrival time measurements of the center of mass of the XUV photon pulse with respect to the THz pulse is monitored with few fs resolution [35]. However, after accounting for the synchronization
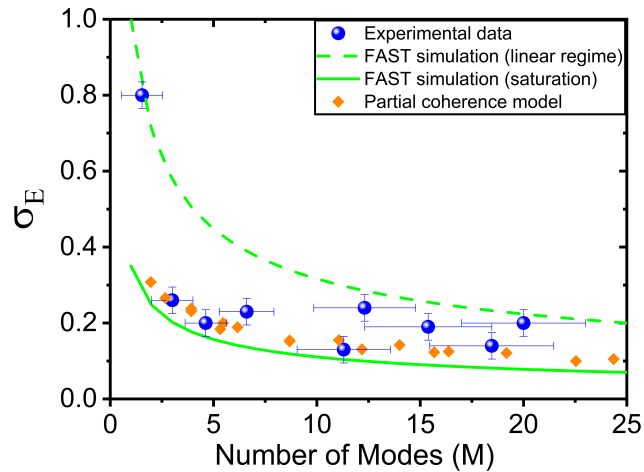
Fig. 7. The relative fluctuation of the SASE pulse energy is shown for the FAST simulation results as well as the experimentally measured values. The experimental pulse energy was measured for different FEL operation modes, from few μJ to up to 50 μJ. The simulated fluctuations are shown for the linear range and at saturation. In general, the relative fluctuations decrese for longer pulse durations. The experimental values (measured at saturation conditions) exceed the simulation values, indicating a significant contribution of technical fluctuations and drifts in the accelerator and measurement uncertainties.

of the THz producing laser to the master optical clock, the distribution of synchronised optical clock signals, transport of the electron bunches and XUV radiation by many tens of meters, as well as several other involved subsystems, the overall accuracy of arrival time determination between the electron bunch and the XUV photon pulse measured with THz streaking is in the range of 15-20 fs rms (corresponding to 30-50 fs FWHM) [24].Looking at the theoretical prediction of SASE arrival time fluctuations [Eq. (12)] we find, for the presented parameter range of wavelengths and pulse durations, that the arrival time fluctuations due to the statistical variation of the photon pulse sub-structure are below 10 fs (rms) and thus can not be determined using current arrival time measurement techniques. Figure 8 shows the relative fluctuations of the arrival time simulated using FAST for the linear and non-linear regime and the partial coherence model. The experimental arrival time fluctuations were calculated by taking the standard deviation of the difference between the photon arrival time measured by THz streaking (τ_{ph}) and the electron beam arrival time (τ_{BAM}). The 15-20 fs rms accuracy of the photon pulse arrival time measurements is much larger as compared to the pulse duration, therefore the relative fluctuations are greater and it is used as the upper limit of the fluctuation's uncertainty.

4.4.   Correlations of the radiation pulse energy and pulse duration

In the previous sections, fluctuations of pulse energy and pulse duration were discussed as average values and independently from each other. With thousands of experimental and simulated pulse durations and corresponding pulse energies of individual SASE pulses, the analysis can be extended to a shot to shot basis.

Studying the temporal structure of the SASE pulses (Fig. 1), one is tempted to conclude that a longer pulse containing more sub spikes (modes) also contains more photons on average and thus has a higher pulse energy. Plotting the single-shot normalized pulse duration and corresponding pulse energies for different FEL settings, we obtain the correlation plots shown in Fig. 9(a). Three different FEL settings were used, with ~17 fs, ~35 fs and ~70 fs (FWHM)
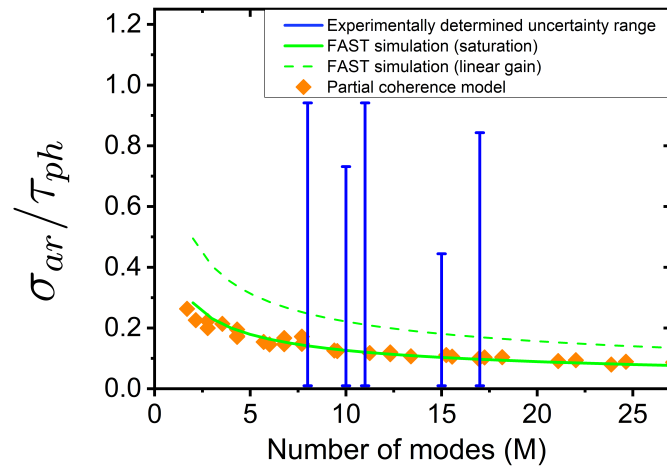
Fig. 8. The relative fluctuation of the SASE arrival time using the FAST and partial coherence model simulations are shown. The fluctuations were calculated for the saturation (solid line) and linear (dashed line) regime. The arrival time fluctuations simulations decrease for longer pulse durations. The current experimental resolution of 15-20 fs gives an upper limit on the uncertainty of the measured arrival time relative fluctuations.

average pulse durations [converted to the number of modes by Eq. (9)]. Firstly, the fluctuations are not correlated for any of the measured FEL settings. Thus, perhaps surprisingly, the pulse energy fluctuates independently of the pulse duration, contradicting the simple interpretation mentioned above. Furthermore, the normalized fluctuations show about the same amplitude for the pulse energy and the pulse duration. In addition, there are smaller fluctuations for longer pulses, containing more modes. These observations are in agreement with the averaged data shown in Figs. 6 and 7. The error bars of a single shot measurement are shown in the lower right edge of Fig. 9(a) - the relatively large uncertainty may obscure any possible correlation. Simulations can help to clarify this situation.The simulation results calculated by FAST are plotted in Fig. 9(b). There is also no sign of correlation between pulse duration and pulse energy, supporting the experimental finding. We therefore conclude that the pulse energy and pulse duration are indeed fluctuating independently. Similar to the experiment, the simulated data shows smaller fluctuations in both quantities for longer pulses (larger number of modes). However, in contrast to the experimental values, the fluctuations for the pulse durations are smaller than those in pulse energy, in agreement with Fig. 2. The simulated pulse duration values fluctuate less in comparison to the experimental ones.

Despite the surprising result that there is no significant correlation between the pulse energy and the pulse duration of individual SASE pulses, there is an even more surprising observation obtained from the simulation for the linear gain regime. Figure 4 displays the pulse resolved correlation plots for the pulse duration and pulse energy at different stages along the undulator. When moving from the linear regime to deep saturation, the pulse energy increases by approximately two orders of magnitude, and the pulse duration increases by a factor of approximately two. While there is no correlation found in saturation, there is a tilted ellipse for the linear regime (Fig. 4), indicating a negative correlation between pulse energy and pulse duration. On average, pulses with shorter pulse duration actually contain *more* pulse energy. One possible explanation would be the following: Slightly increased intensity spikes in the initial random "seed" distribution gain faster more energy due to the exponential growth, leading to strong spikes. In contrast,
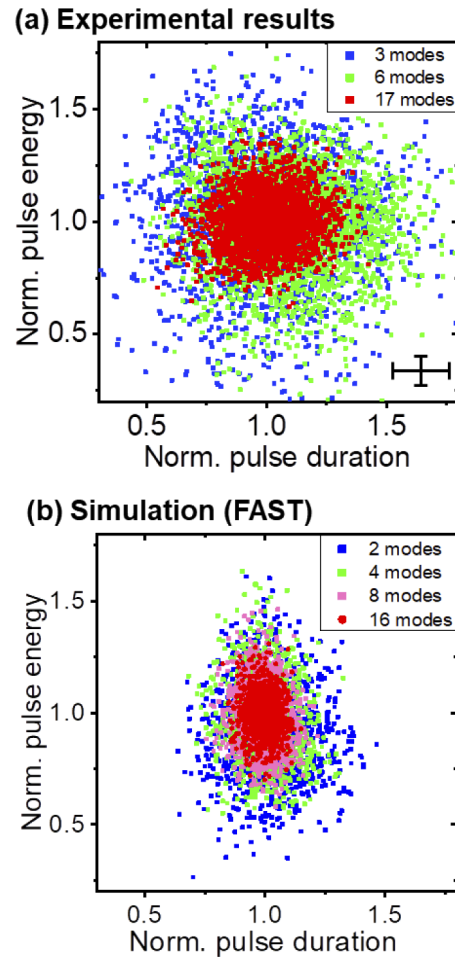
(a) Experimental results

(b) Simulation (FAST)

Fig. 9. Normalized and pulse resolved SASE pulse energy versus radiation pulse duration in the saturation regime. The experimental data (a) results from three different FEL settings at 6.8 nm with average pulse durations of ~15 fs, ~30 fs and ~90 fs (FWHM). The error bars for the single pulse measurements are shown in the lower right corner. Part (b) shows the simulation result (FAST) for different number of modes at saturation ($z/z_{sat} = 1$). The fluctuations of the pulse energy are (for the same number of modes) about a factor of 2 larger as compared to the pulse duration in accordance to Fig. 2. The difference to the experimental result can be explained by measurement uncertainties and accelerator fluctuations.

the less intense parts of the initial distribution gain less energy and catch up only at saturation. Therefore, in the exponential gain regime, single intense spikes are more strongly amplified, leading to a larger fraction of short and intense pulses in the correlation plot. This results in an anti-correlation between pulse energy and pulse duration. Up to now the experimental resolution for pulse duration measurements at very low pulse energies has been insufficient to determine this negative correlation in the linear regime.

4.5.   Radiation pulse duration and spectral structure

Generally, the spectral distribution of SASE XUV pulses also contains important information about the pulse duration. The second order spectral correlation function (g_2) [19–21] is typically

used to determine average pulse duration estimates from spectral information using the width of the spectral spikes. In Ref. [24] it is also demonstrated that there is a good agreement between XUV pulse durations determined by THz streaking and the g_2 method. However, a more experimentally straightforward method is to simply count the number of spectral spikes, which is a widely used technique that has not been investigated in detail so far.

As introduced in Eq. (8), the SASE pulse duration depends linearly on the number of modes. Strictly speaking, this relation only holds for the *linear gain regime* below saturation and it is a statistical parameter for average values calculated from an ensemble of data [19,31]. The extent to which this simple relation can be used as quick online analysis to estimate the pulse duration in saturation was investigated experimentally.

Figure 10 displays the FEL spectra measured as described in section 3, for different pulse lengths. The number of spectral modes was determined by a peak detection algorithm using a threshold of 20% of the maximum peak and a minimum distance between spikes. It was carefully checked that the counted number of peaks did not depend on the exact settings of the algorithm. However, considering that there may be overlapping modes which are not detected as two separated peaks, the number modes determined may underestimate the actual number of modes.
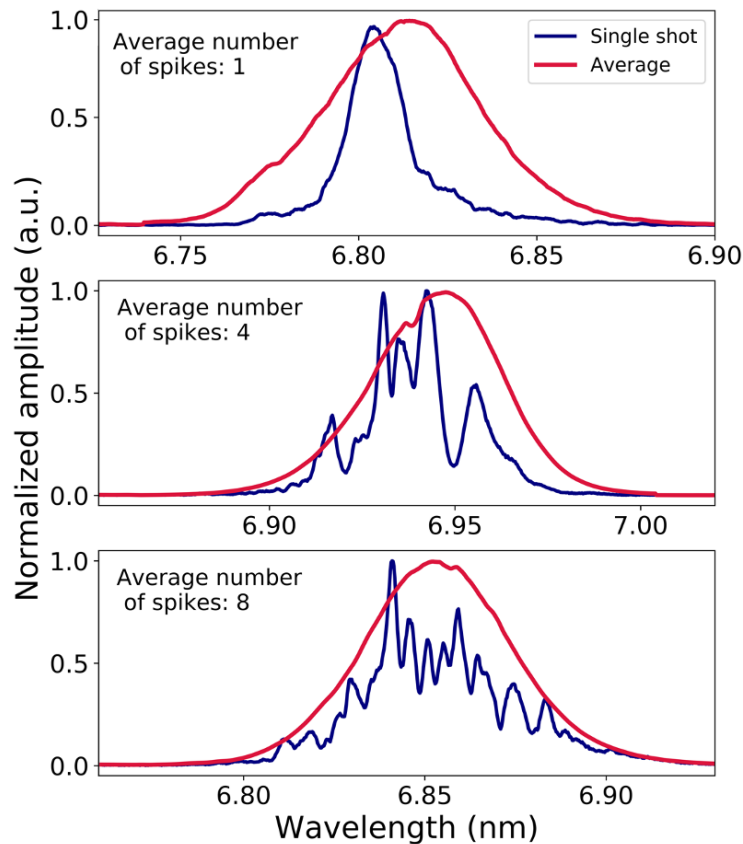

Fig. 10. FEL spectra measured at the PG2 beamline [32] for different pulse lengths. The blue line represents a single spectrum and the red line, the average over thousands of pulses. One can see the spiky nature of the SASE pulses in the spectral domain. The measurements show an increasing number of spikes for longer pulse durations.

Since the XUV spectra and the streaking measurements are acquired simultaneously, we can determine the number of spikes and the pulse duration for each recorded FEL setting. Figure 11 shows the averaged pulse duration and number of spectral spikes for different electron bunch length settings at FLASH. For most of the settings the FEL was operated in saturation, delivering over 15 μJ per XUV pulse. The measured relation between spectral modes and XUV pulse duration can be well approximated with a linear slope -as expected for the linear gain regime-even though already operating in saturation. The slope was determined to be 6.5 fs/spike, yielding a coherence time of $\sim$ 6.5 fs (FWHM) for 6.8 nm [see Eqs. (9) and (10)], which is in good agreement with longitudinal interference measurements presented in Ref. [37]. Figure 11 shows the linear dependence between the *averaged* values of the number of spikes in the spectral domain and the pulse duration measured with streaking.
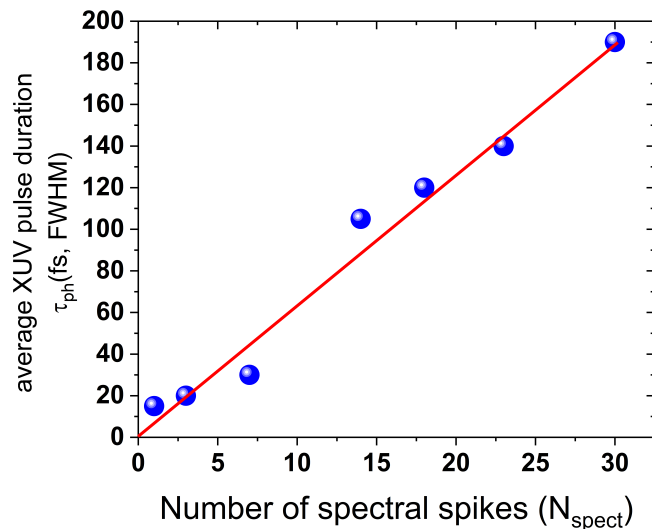

Fig. 11. Plotted is the experimentally determined average pulse duration as function of the average number of spectral spikes for different FEL operation settings (all at a wavelength of 6.8 nm). Several thousand pulse resolved measurements have been averaged for each data point. The FEL was operated close to or in saturation. The linear fit shows 6.5 fs/spectral spike.

To investigate the correlation for single SASE pulses, the number of spikes and the pulse duration are plotted for each SASE pulse in Fig. 12(a). Plotting the data for a fixed FEL setting, there is almost no correlation between the single-shot spike number and the pulse duration. For the same number of spikes, there can be up to a factor of two difference in pulse duration which does not allow one to predict, on a single shot basis, the XUV pulse duration from the spectral measurements. This experimental finding, shown in Fig. 12(a), is also confirmed by simulations. Using the partial coherence model [26], SASE pulses in temporal and spectral domain, were calculated for different average pulse durations and analyzed with the same peak finding algorithm as the experimental data. Similar to the experimental data there is a large scatter observed within the simulation results belonging to the same average pulse duration [Fig. 12(b)].

While there is on *average* and in saturation, a linear dependence between the pulse duration and the number of spectral spikes in the SASE radiation, both quantities fluctuate independently on a single-shot basis.
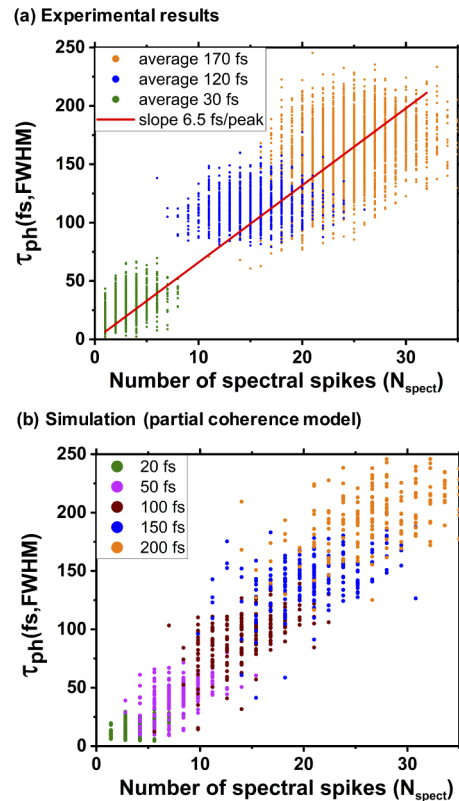
Fig. 12. Shown is the pulse resolved correlation between the number of spectral spikes and the pulse durations. The experimentally determined data was recorded for three different operation modes of the FEL with average pulse durations of 30fs, 120fs and 170 fs (at 6.8 nm). For a fixed FEL operation mode the pulse duration and number of spectral spikes fluctuate independently. This observation is supported by simulation results (b). Using the partial coherence method [26] the same behavior was observed.

5.   Conclusion

We presented experimental data from the XUV SASE FEL FLASH for pulse duration, pulse energy, arrival time and spectral distribution. The fluctuations of these four important radiation pulse properties have been investigated on average and on a pulse to pulse basis for FEL pulses ranging from a few fs to up to 200 fs (FWHM). SASE simulations have been performed to support the experimental results and to disentangle experimental fluctuations and uncertainties from pure SASE related fluctuations. This approach shows that the major contribution of fluctuation is indeed caused by SASE, accompanied by a varying part of "technical" fluctuations. Analyzing the simulation results, scaling laws for the fluctuations have been derived theoretically and validated experimentally. The resulting $1/\sqrt{M}$ scaling allows a fast and precise way to estimate the amount of fluctuations of SASE parameters to expect for different FEL pulse durations and wavelengths without the need to perform complex simulations. Recording spectral and temporal pulse properties simultaneously for a large number of different FEL settings, we could experimentally verify that the linear dependence between the *average* pulse duration and *average* number of spectral spikes which was expected for the linear range by theory, still holds when the FEL is operated in saturation. This linear dependence however, disappears completely when the data is analyzed on a shot-to-shot basis. We found no correlation between single-shot pulse duration and

number of spectral spikes as well as pulse energy - all three parameters fluctuate independently in the experiment and the simulations. This result shows clearly that dependencies that were observed for averaged parameters may not hold for SASE based shot-to-shot fluctuations. This is important for FEL photon diagnostics, pointing out that one can *not* simply employ one quantity to predict the other on a shot-to-shot basis. It is not possible to substitute a complex task such as measuring the XUV pulse duration by just measuring the spectrum or even pulse energy. On the other hand, the missing correlation between the different radiation parameters is good news for the analysis of experimental data since it allows to sort the experimental data independently by one of the parameters without the risk to generate spurious correlations by the sorting procedure.

Disclosures. The authors declare no conflicts of interest.

References

1. W. Ackermann, *et al.*, "Operation of a free-electron laser from the extreme ultraviolet to the water window," Nat. Photonics **1**(6), 336–342 (2007).
2. P. Emma, *et al.*, "First lasing and operation of an ångstrom-wavelength free-electron laser," Nat. Photonics **4**(9), 641–647 (2010).
3. T. Ishikawa, *et al.*, "A compact x-ray free-electron laser emitting in the sub-ångström region," Nat. Photonics **6**(8), 540–544 (2012).
4. E. Allaria, *et al.*, "Highly coherent and stable pulses from the fermi seeded free-electron laser in the extreme ultraviolet," Nat. Photonics **6**(10), 699–704 (2012).
5. W. Decking, *et al.*, "A mhz-repetition-rate hard x-ray free-electron laser driven by a superconducting linear accelerator," Nat. Photonics **14**(6), 391–397 (2020).
6. I. Ko, *et al.*, "Construction and commissioning of pal-xfel facility," Appl. Sci. **7**(5), 479 (2017).
7. C. Milne, *et al.*, "Swissfel: The swiss x-ray free electron laser," Appl. Sci. **7**(7), 720 (2017).
8. M. Richter, "Measurement of gigawatt radiation pulses from a vacuum and extreme ultraviolet free-electron laser," Appl. Phys. Lett. **83**(14), 2970–2972 (2003).
9. K. Tiedtke, J. Feldhaus, U. Hahn, U. Jastrow, T. Nunez, T. Tschentscher, S. V. Bobashev, A. A. Sorokin, J. B. Hastings, S. Möller, L. Cibik, A. Gottwald, A. Hoehl, U. Kroth, M. Krumrey, H. Schöppe, G. Ulm, and M. Richter, "Gas detectors for x-ray lasers," J. Appl. Phys. **103**(9), 094511 (2008).
10. G. Brenner, S. Kapitzki, M. Kuhlmann, E. Ploenjes, T. Noll, F. Siewert, R. Treusch, K. Tiedtke, R. Reininger, M. D. Roper, M. A. Bowler, F. M. Quinn, and J. Feldhaus, "First results from the online variable line spacing grating spectrometer at flash," Nucl. Instrum. Methods Phys. Res., Sect. A **635**(1), S99–S103 (2011).
11. M. Braune, G. Brenner, S. Dziarzhytski, P. Juranic, A. Sorokin, and K. Tiedtke, "A non-invasive online photoionization spectrometer for flash2," J. Synchrotron Radiat. **23**(1), 10–20 (2016).
12. A. Angelovski, M. Kuntzsch, M. K. Czwalinna, A. Penirschke, M. Hansli, C. Sydlo, V. Arsov, S. Hunziker, H. Schlarb, M. Gensch, V. Schlott, T. Weiland, and R. Jakoby, "Evaluation of the cone-shaped pickup performance for low charge sub-10 fs arrival-time measurements at free electron laser facilities," Phys. Rev. Spec. Top.–Accel. Beams **18**(1), 012801 (2015).
13. E. Saldin, E. Schneidmiller, and M. Yurkov, *The Physics of Free Electron Lasers* (Springer, 2000).
14. E. Saldin, E. Schneidmiller, and M. Yurkov, "Statistical properties of radiation from sase fel driven by short electron bunches," *Nuclear Instruments and Methods in Physics Research Section A: Accelerators, Spectrometers, Detectors and Associated Equipment* pp. 101–105 (2003).
15. E. Saldin, E. Schneidmiller, and M. Yurkov, "Statistical properties of the radiation from vuv fel at desy operating at 30nm wavelength in the femtosecond regime," Nuclear Instruments and Methods in Physics Research Section A: Accelerators, Spectrometers, Detectors and Associated Equipment **562**(1), 472–486 (2006).
16. E. Schneidmiller and M. Yurkov, "Application of Statistical Methods for Measurements of the Coherence Properties of the Radiation from SASE FEL," in *7th International Particle Accelerator Conference*, (2016), p. MOPOW013.
17. C. Behrens, N. Gerasimova, C. Gerth, B. Schmidt, E. Schneidmiller, S. Serkez, S. Wesch, and M. Yurkov, "Constraints on photon pulse duration from longitudinal electron beamdiagnostics at a soft x-ray free-electron laser," Physical Review Special Topics - Accelerators and Beams **15**(3), 030707 (2012).
18. A. Singer, F. Sorgenfrei, A. P. Mancuso, N. Gerasimova, O. M. Yefanov, J. Gulden, T. Gorniak, T. Senkbeil, A. Sakdinawat, Y. Liu, D. Attwood, S. Dziarzhytski, D. D. Mai, R. Treusch, E. Weckert, T. Salditt, A. Rosenhahn, W. Wurth, and I. A. Vartanyants, "Spatial and temporal coherence properties of single free-electron laser pulses," Opt. Express **20**(16), 17480–17495 (2012).
19. A. A. Lutman, Y. Ding, Y. Feng, Z. Huang, M. Messerschmidt, J. Wu, and J. Krzywinski, "Femtosecond x-ray free electron laser pulse duration measurement from spectral correlation function," Phys. Rev. Spec. Top.–Accel. Beams **15**(3), 030705 (2012).

20. Y. Inubushi, K. Tono, T. Togashi, T. Sato, T. Hatsul, T. Kameshima, K. Togawa, T. Hara, T. Tanaka, H. Tanaka, T. Ishikawa, and M. Yabashi, "Determination of the pulse duration of an x-ray free electron laser using highly resolved single-shot spectra," Phys. Rev. Lett. **109**(14), 144801 (2012).

21. R. Engel, S. Düsterer, G. Brenner, and U. Teubner, "Quasi-real-time photon pulse duration measurement by analysis of FEL radiation spectra," J. Synchrotron Radiat. **23**(1), 118–122 (2016).

22. U. Fruehling, M. Wieland, M. Gensch, T. Gebert, B. Schutte, M. Krikunova, R. Kalms, F. Budzyn, O. Grimm, J. Rossbach, E. Plönjes, and M. Drescher, "Single-shot terahertz-field-driven x-ray streak camera," Nat. Photonics **3**(9), 523–528 (2009).

23. I. Grguras, A. R. Maier, C. Behrens, T. Mazza, T. J. Kelly, P. Radcliffe, S. Dusterer, A. K. Kazansky, N. M. Kabachnik, Th. Tschentscher, J. T. Costello, M. Meyer, M. C. Hoffman, H. Schlarb, and A. L. Cavalieri, "Ultrafast x-ray pulse characterization at free-electron lasers," Nat. Photonics **6**(12), 852–857 (2012).

24. R. Ivanov, J. Liu, G. Brenner, M. Brachmanski, and S. Düsterer, "FLASH free-electron laser single-shot temporal diagnostic: terahertz-field-driven streaking," J. Synchrotron Radiat. **25**(1), 26–31 (2018).

25. E. Saldin, E. Schneidmiller, and M. Yurkov, "Fast: a three-dimensional time-dependent fel simulation code," Nuclear Instruments and Methods in Physics Research Section A: Accelerators, Spectrometers, Detectors and Associated Equipment **429**(1-3), 233–237 (1999).

26. T. Pfeifer, Y. Jiang, S. Düsterer, R. Moshammer, and J. Ullrich, "Partial-coherence method to model experimental free-electron laser pulse statistics," Opt. Lett. **35**(20), 3441–3443 (2010).

27. R. Bonifacio, C. Pellegrini, and L. M. Narducci, "Collective instabilities and high-gain regime in a free electron laser," Opt. Commun. **50**(6), 373–378 (1984).

28. L. Mandel and E. Wolf, "The measures of bandwidth and coherence time in optics," Proceedings of the Physical Society **80**(4), 894–897 (1962).

29. R. Bonifacio, F. Casagrande, and L. De Salvo Souza, "Collective variable description of a free-electron laser," Phys. Rev. A **33**(4), 2836–2839 (1986).

30. E. Saldin, E. Schneidmiller, and M. Yurkov, "Statistical properties of radiation from vuv and x-ray free electron laser," Opt. Commun. **148**(4-6), 383–403 (1998).

31. S. Krinsky and R. L. Gluckstern, "Analysis of statistical correlations and intensity spiking in the self-amplified spontaneous-emission free-electron laser," Phys. Rev. Spec. Top.–Accel. Beams **6**(5), 050701 (2003).

32. M. Martins, M. Wellhöfer, J. Hoeft, W. Wurth, J. Feldhaus, and R. Follath, "Monochromator beamline for flash," Rev. Sci. Instrum. **77**(11), 115108 (2006).

33. N. Gerasimova, S. Dziarzhytski, and J. Feldhaus, "The monochromator beamline at flash: Performance, capabilities and upgrade plans," J. Mod. Opt. **58**(16), 1480–1485 (2011).

34. H. Redlin, A. Al-Shemmary, A. Azima, N. Stojanovic, F. Tavella, I. Will, and S. Dústerer, "The flash pump–probe laser system: Setup, characterization and optical beamlines," Nuclear Instruments and Methods in Physics Research Section A: Accelerators, Spectrometers, Detectors and Associated Equipment **635**(1), S88–S93 (2011).

35. S. Schulz, I. Grguras, C. Behrens, H. Bromberger, J.T. Costello, M.K. Czwalinna, M. Felber, M.C. Hoffman, M. Ilchen, H.Y. Liu, T. Mazza, M. Meyer, S. Pfeiffer, P. Predki, S. Schefer, C. Schmidt, U. Wegner, H. Schlarb, and A.L. Cavalieri, "Femtosecond all-optical synchronization of an x-ray free-electron laser," Nat. Commun. **6**(1), 5938 (2015).

36. R. Ivanov, I. J. B. Macias, J. Liu, G. Brenner, J. Roensch-Schulenburg, G. Kurdi, U. Frühling, K. Wenig, S. Walther, A. Dimitriou, M. Drescher, I. P. Sazhina, A. K. Kazansky, N. M. Kabachnik, and S. Dústerer, "Single-shot temporal characterization of XUV pulses with duration from ~10 fs to ~350 fs at FLASH," J. Phys. B: At., Mol. Opt. Phys. **53**(18), 184004 (2020).

37. S. Roling, "Temporal and spatial coherence properties of free-electron-laser pulses in the extreme ultraviolet regime," Physical Review Special Topics - Accelerators and Beams **14**(8), 080701 (2011).

A.3   POST-COLLISION INTERACTION EFFECT IN THz-ASSISTED AUGER DECAY OF NOBLE GAS ATOMS

Post-collision interaction effect in THz-assisted Auger decay of noble gas atoms

I J Bermúdez Macias[1],* , S Düsterer[1] , R Ivanov[1] , U Frühling[2,3]   and
N M Kabachnik[1,4,5]

[1] Deutsches Elektronen-Synchrotron (DESY), Notkestrasse 85, D-22603 Hamburg, Germany
[2] Institute for Experimental Physics, University Hamburg, Hamburg, Germany
[3] The Hamburg Centre for Ultrafast Imaging, Luruper Chaussee 149, Hamburg, Germany
[4] Donostia International Physics Center (DIPC), E-20018, San Sebastian/Donostia, Spain
[5] Skobeltsyn Institute of Nuclear Physics, Lomonosov Moscow State University, Moscow 119991, Russia

E-mail: ivette.bermudez@desy.de

CrossMark

Abstract
Auger electron spectra were simulated in the presence of a terahertz streaking field to study
post-collision interaction (PCI) effects in the time-evolution of photoinduced Auger decays.
The PCI is characterized by the ratio of the spectral line width for Auger electron emission in
opposite directions with respect to the THz-field. These calculations have been performed
using the analytical semiclassical model developed by Bauch and Bonitz (2012 *Physical
Review A* **85** 053416). The results are shown for Ne(KLL), Ar(LMM), Kr(MNN) and
Xe(NOO) Auger transitions whereby different possible experimental conditions were
evaluated.

Keywords: post-collision interaction, Auger decay, terahertz streaking

(Some figures may appear in colour only in the online journal)

1. Introduction

The term 'post-collision interaction (PCI)' encompasses a broad range of phenomena in atomic collisions and photoionization, associated with the influence of the Coulomb interaction of slowly receding charged particles on autoionization (Auger) electron spectra [1]. In particular, PCI effects were observed in near-threshold inner shell photoionization of atoms with the following Auger decay (see [2, 3] and references therein). Here, the interaction with the slow photoelectron shifts the energy of the Auger electron and considerably distorts the Auger line-shape in the spectrum. In addition, PCI

is responsible for the recapture of emitted photoelectrons to Rydberg states of the ions [4]. These phenomena were thoroughly studied experimentally in nineties and zeroes at synchrotron radiation facilities (see, for example, [5–9] as well as references in [2, 3]). A good understanding of the PCI effects was achieved first on a semiclassical basis [10–13] and later in a stationary quantum mechanical picture of the process within the unified theory of the Auger process [14, 15] and the random phase approximation with exchange approach [16, 17]. The non-stationary description of the PCI-induced recapture process was developed in [9, 18].

The above mentioned experiments were performed by standard time-integrated spectroscopic methods using high-resolution electron spectrometers. In the past decades, tremendous progress in the availability of femtosecond and subfemtosecond photon pulses has enabled the study of atomic processes in the time-domain, in particular Auger decays [19–25]. A first terahertz (THz)-assisted time-resolved study

of the Auger process in atoms has revealed that PCI leads to a time-dependent (chirped) Auger electron energy [26].

In the experiment [26], Kr MNN and Xe NOO Auger spectra, excited by ultrashort (femtosecond) extreme ultraviolet (XUV) pulses from the free-electron laser in Hamburg (FLASH) [27] and from a high harmonic laser source have been studied. The electrons were ionized in the presence of a co-propagating, linearly polarized THz field which introduced a time dependent modulation (streaking) of the electron energies. By changing the time delay between XUV and THz pulses the time development of the Auger decay has been investigated. A significant difference of the widths of kinetic energy spectra for opposite observation directions and THz field gradients has been observed. This indicates an energetic chirp, i.e. a pronounced time-dependent variation of the Auger electrons kinetic energy. Theoretical interpretation of the results has been given using the semiclassical approach developed by Bauch and Bonitz [28]. It was shown that the chirp may be explained by the PCI of the photo- and Auger electrons in the final state. Later this finding has been used to study the temporal evolution of interatomic-Coulombic decay by evaluating the PCI energy shift of electrons and thereby deducing the ionization times [29]. Moreover, it was demonstrated that the measured PCI effect is very sensitive to the details of the photoinduced Auger emission. Furthermore, it was suggested to use the observed effect in metrology of ultra-fast pulses. These observations stimulate an interest in continuing and broadening the studies of the time-resolved PCI effects. Thus, the present paper shall serve as a basis for experimental studies on FELs or HHG sources in order to determine the optimum experimental conditions to observe a strong PCI effect. In particular, the study is motivated to guide future experiments at the THz streaking setup at FLASH [30, 31].

In the present paper we report the results of the theoretical study of the THz-assisted photoinduced Auger processes in noble gas atoms. The main goal is to investigate the PCI effects in the process and their dependence on the experimental parameters. We used the analytical model of the process developed by Bauch and Bonitz [28]. A concise description of the model is presented in section 2. The calculations have been done for KLL transitions in Ne, LMM in Ar, MNN in Kr and NOO in Xe. The results are shown and discussed in section 3. Finally, section 4 contains the conclusions and outlook.

2. Semiclassical description of PCI

An accurate theoretical description of the THz assisted photoinduced Auger process might be given on the basis of a numerical solution of the time-dependent Schrödinger equation [32] which involves both the exciting XUV pulse and the streaking THz pulse. This approach would automatically include the description of PCI as it was demonstrated in [18] for the case without a THz pulse. However, the long streaking THz pulse in comparison with the fast oscillations of the electronic wave functions makes a direct application of this method not feasible due to prohibitively long computation time. Bauch and Bonitz [28] suggested a simple analytical model which incorporates both the PCI effect and the streaking in the THz field. The model is based on the semiclassical description of the PCI effect [10, 12, 13]. Namely, it is associated with the abrupt change of the screening which is felt by the slowly receding photoelectron at the moment when the fast Auger electron overtakes it. The movement of both electrons is considered classically, and an essential parameter of the model is the distance from the ion nucleus at which the Auger electron overtakes the photoelectron. The model was tested in [28] by comparing it with the solution of the time-dependent one-dimensional Schrödinger equation and Monte Carlo molecular dynamics simulations. Furthermore, it has accurately described the experimental data [26].

In the following, we use the analytical semiclassical model [28] to predict the PCI effects in THz assisted Auger decay in noble gas atoms. In a short description of the model we follow the paper [28].

Consider a photoelectron emitted at a time t_{ph} with a momentum p_{ph} and an Auger electron released after the photoelectron at a time τ_A with a momentum p_A in the presence of a linearly polarized streaking THz field with vector potential $A(t)$. It is supposed that $p_A > p_{ph}$. The Auger decay line-width (without THz field) is denoted Γ_A so that the core-hole life-time is Γ_A^{-1} (here and below atomic units are used unless otherwise indicated). For calculating the Auger-electron spectral line-shape, the THz vector potential is expanded around the moment of the photoemission in Taylor series:

$$A(\tau_A) = A_P + \dot{A}_P \tau_A + \mathcal{O}(\tau_A^2), \tag{1}$$

where $A_P = A(t_{ph})$ while $\dot{A}_P = \frac{dA}{dt}(t_{ph})$ denotes the first time derivative of the vector potential. We consider the Auger electron spectra in two neighbouring zero-crossings of the vector potential where $A_P = 0$. Ignoring the higher order terms of the expansion (1), we obtain that the energy shift for Auger electrons in the THz field $p_A A(\tau_A) = p_A \dot{A}_P \tau_A$ depends on the sign of the derivative $\dot{A}_P$. Moreover, it is clear that the streaking effect for different signs of $\dot{A}_P$ can be equivalently studied by changing the sign of p_A, i.e. by detecting the emitted Auger electrons in opposite directions.

The model Auger spectrum generated by the XUV pulse in the THz field is presented as the numerical convolution of the PCI-distorted spectral line shapes $f\pm(\epsilon)$ with the streaked energy spectrum $f_X(\hat{\epsilon})$ due to the finite XUV pulse duration:

$$f_{X\pm}(\epsilon) = \int_{-\infty}^{+\infty} d\hat{\epsilon} f_X(\hat{\epsilon}) f\pm(\epsilon - \hat{\epsilon}). \tag{2}$$

Here

$$f_X(\hat{\epsilon}) = \frac{1}{\sqrt{\pi}\Gamma_X} \exp\left(-\frac{\hat{\epsilon}^2}{\Gamma_X^2}\right), \tag{3}$$

with

$$\Gamma_X = p_A \dot{A}_P \tau_X, \tag{4}$$

where τ_X is the XUV pulse duration full-width at half-maximum (FWHM).

As demonstrated in [28], for a positive derivative of the streaking electric field $\dot{A}_P > 0$, the spectral line shape $f_+(\epsilon)$ may be presented as:

$$f_+(\epsilon) = \Gamma_4 \frac{k_+ - \epsilon_-}{k_+} e^{-\Gamma_4(k_+ - \epsilon_+)}, \qquad (5)$$

where $\Gamma_4 = |\alpha|\Gamma_A$ with $\alpha = (2p_A\dot{A}_P)^{-1}$.

On the other hand, for negative values of $\dot{A}_P < 0$, the Auger spectral line shape is:

$$f_-(\epsilon) = 2\Gamma_4 e^{-\Gamma_4\epsilon_+}\left(\frac{\epsilon_-}{k_-}\cosh\Gamma_4 k_- - \sinh\Gamma_4 k_-\right). \qquad (6)$$

In these equations $k_\pm = \sqrt{\epsilon_-^2 \pm |\beta|}$, $\epsilon_\pm = \epsilon \pm \frac{\beta}{4}\delta r^*$ with $\beta = 4p_A\dot{A}_P/p_r$.

The parameters p_r and $\delta r*$ determine the classical distance from the ion at which the Auger electron overtakes the slower photoelectron:

$$r^* = \tau_A p_r + \delta r^*. \qquad (7)$$

Here $p_r = p_A p_{ph}/[p_A - p_{ph} + A(t_{ph}) - A(\tau_A)]$, and δr^* is a small correction to the initial distance of the two electrons from the ion. For the derivation of these expressions and their detailed discussion the reader is referred to the paper [28].

As it is shown in [28], due to the influence of PCI the spectral width of the Auger line at $\dot{A} > 0$ (denoted ω_+) is larger than at $\dot{A} < 0$ (denoted ω_-).

Qualitatively, the difference in spectral width at the two slopes of the vector potential may be explained as follows. The energy shift of the Auger electron in the THz field taking into account the PCI effect is $\Delta E_A = -p_A A(t) + A^2(t) + E_{PCI}(t)$, where t is the moment of the Auger electron emission. The term $E_{PCI}(t)$ accounts for the change of Auger electron energy due to the PCI effect. In the semiclassical model, this term is equal to the energy gain of the Auger electron when it overtakes the slow photoelectron at the distance $r^*(t)$. It is due to the change of screening at this moment and is equal to $E_{PCI}(t) = 1/r^*(t)$. When time t increases, the Auger electron overtakes the photoelectron at a larger distance and therefore gains less energy. Thus the energy of the Auger electron depends on time indicating a 'chirp'. The quadratic term $A^2(t)$ is small and may be ignored. The width induced by the THz field and the PCI may be estimated as $\delta(\Delta E_A) = (-p_A dA/dt + dE_{PCI}/dt)\Gamma^{-1}$. The second term does not depend on the sign of dA/dt and is always negative. Therefore, for a positive derivative both terms have the same sign and the width is larger than for a negative one, where the two terms have different signs and partly cancel each other. This is the consequence of the chirp and is similar to the effect of chirp on the spectral width of photoelectrons [33]. On the other hand, these widths are equal if the PCI effect is negligible. Therefore, it is convenient to characterize the PCI effect by the ratio of the widths ω_+/ω_-.

3. Results and discussion

To illustrate the PCI effect for experimentally reachable parameters at FELs or HHG sources in the time evolution of

the Auger decay, the photon energies were varied such that the ratio of the photoelectron to the Auger electron energy ranged between zero (the photon energy is equal to the corresponding threshold energy) and one (the photoelectrons have the same energy as the Auger electrons). Therefore, we have chosen the following representative examples of the Auger transitions:

1. $KL_{2,3}L_{2,3}(^1D_2)$ transition in Ne. This is the strongest line in Ne Auger spectrum at the Auger electron energy of 804.5 eV [34]. The binding energy of the 1 s electron is 870.2 eV and the decay width is $\Gamma_A = 263.2$ meV [35] corresponding to a lifetime of $\Gamma_A^{-1} = 2.5$ fs. The photon energy needed for the experiment is in the interval from 870.2 to 1674.7 eV.

2. $L_3 M_{2,3} M_{2,3}(^1S_o)$ transition in Ar with an Auger electron energy of 201 eV [36]. The binding energy of the $2p_{3/2}$ electron is 248.4 eV and the decay width is $\Gamma_A = 114$ meV [36] corresponding to a lifetime of $\Gamma_A^{-1} = 5.5$ fs. The required photon energy should therefore fall between 248.4 and 449.4 eV.

3. $N_5 O_{2,3} O_{2,3}(^1S_o)$ transition in Xe with an Auger electron energy of 29.8 eV [37]. The binding energy of the $4d_{5/2}$ electron is 67.5 eV and the decay width is $\Gamma_A = 100$ meV [38] corresponding to a lifetime of $\Gamma_A^{-1} = 6.5$ fs. The required photon energy for the experiment is in the interval from 67.5 to 97.3 eV.

4. $M_5 N_1 N_{2,3}(^1P_1)$ transition in Kr that has an Auger electron energy of 38.4 eV [37]. The binding energy of the $3d_{5/2}$ electron is 93.8 eV and the decay width is $\Gamma_A = 88$ meV [22] corresponding to a lifetime of $\Gamma_A^{-1} = 8$ fs. The required photon energy for the experiment is in the interval from 93.8 to 132.2 eV.

X-ray photons with the requisite energy to photoionize Ne and Ar are available at e.g. European XFEL [39] and LCLS [40], while XUV photons for the photoionization of Kr and Xe are available at e.g. FLASH and HHG sources.

For these transitions, we have calculated the ratio of the line width $R_\omega = \omega_+/\omega_-$ as a function of the photoelectron energy. The results are presented in figures 1–4. We note that the value of the parameter δr^* has no significant effect on the final results. Therefore, in all calculations below, we assumed that $\delta r^* = 1$ as it was used in [28]. Furthermore, for a fixed streaking field strength, the calculations are independent of the frequency. For each case, we considered THz field strengths from 30 to 300 kV cm^{-1} and transform limited XUV (x-ray) photon pulses with Gaussian envelopes and durations from 5 to 100 fs FWHM.

Figure 1 shows the results for the Ne(KLL) Auger transitions with a core-hole lifetime of $\Gamma_A^{-1} = 2.5$ fs for a THz field strength of 120 kV cm^{-1}. When the energy of the photoelectron is smallest (close to zero) compared to that of the Auger electron, the width of the spectral line in the falling slope of the vector potential ($\dot{A} < 0$) is smaller than in the rising slope ($\dot{A} > 0$) and the ratio R_ω is highest. This ratio is decreased by increasing the photoelectron energy and it is one (both widths are the same) when the Auger and photoelectrons have the same energy, meaning that the PCI effect is negligible. Furthermore, the effect can be easier resolved (it is more pronounced) for shorter XUV pulse durations.
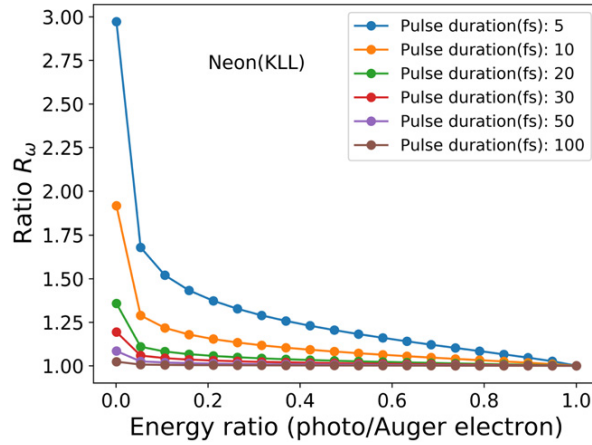
Figure 1. Ratio of the widths R_ω for the neon Auger spectral line $KL_{2,3}L_{2,3}(^1D_2)$ for different photon pulse durations at a 120 kV cm^{-1} THz^{-1} electric field strength. The ratio is maximum when the photoelectron energy is close to zero, and goes to one when both photo and Auger electrons have the same energy.
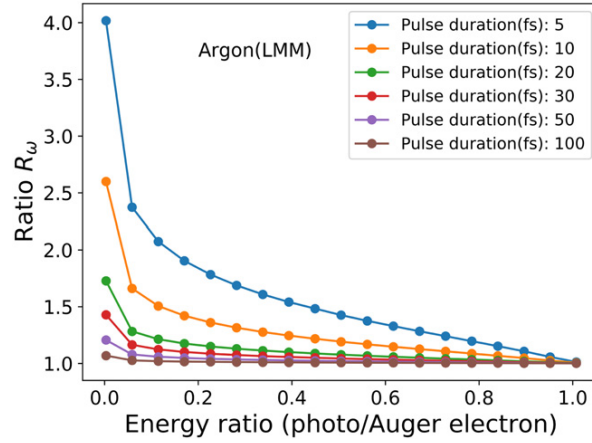

Figure 3. The same as in figure 1 but for the xenon Auger spectral line $N_5O_{2,3}O_{2,3}(^1S_0)$.

Figure 2. The same as in figure 1 but for the argon Auger spectral line $L_3M_{2,3}M_{2,3}(^1S_0)$.

Figure 4. The same as in figure 1 but for the krypton Auger spectral line $M_5N_1N_{2,3}(^1P_1)$.

In figure 2 the results of the Ar(LMM) Auger transitions with a core-hole lifetime of $\Gamma_A^{-1} = 5.5$ fs for a THz field strength of 120 kV cm^{-1} are presented. In this case, similarly to the previous one, the ratio of the spectral line widths at the rising and falling slopes of the THz vector potential is also maximum for relatively slow photoelectrons and goes to one (there is no PCI effect) when both Auger and photoelectrons have the same energy.

The results for the Xe(NOO) Auger transitions with a core-hole lifetime of $\Gamma_A^{-1} = 6.5$ fs and for Kr(MNN) Auger transitions with a core-hole lifetime of $\Gamma_A^{-1} = 8$ fs are shown in figures 3 and 4, respectively. In both cases the THz field strength is 120 kV cm^{-1}. Similarly to the previous atoms, the ratio of the widths of the Auger spectral lines in the rising and falling slopes of the THz vector potential is highest for the slowest photoelectrons and goes to one when both the Auger and photoelectrons have the same energy.
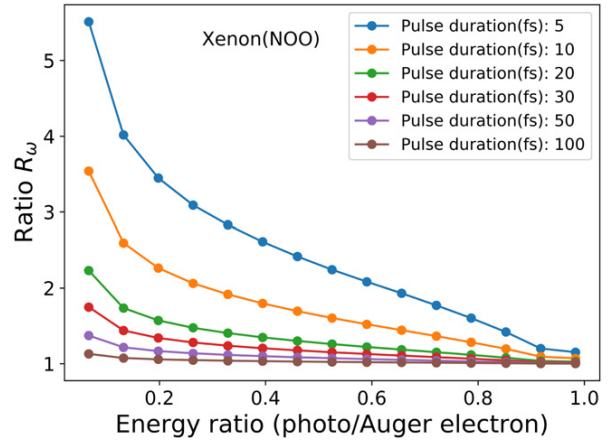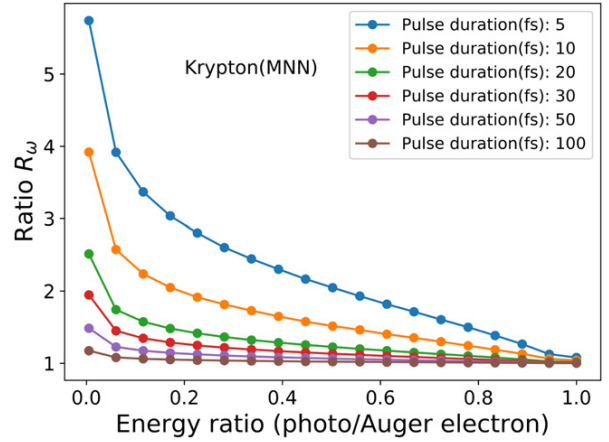
As mentioned earlier, calculations were done for different electric field strengths. In figure 5, the results of the simulations for electric field strengths from 60 to 300 kV cm^{-1} with a photon pulse duration of 20 fs FWHM for Kr(MNN) Auger transitions are shown. Figure 5(a) shows the ratio R_ω as a function of the energy ratio of the photoelectron to the Auger electron. In figure 5(b) the line widths in eV at the rising and falling slopes of the vector potential are plotted. As seen from figure 5(b), the Auger line width is larger for stronger streaking THz field. Furthermore, the ratio R_ω in figure 5(a), which characterizes the PCI effect, is largest for the weakest THz field. This may be explained by the fact that the Auger line width in the THz field is determined by both streaking and PCI effects. The streaking effect increases with the THz field strength, while the PCI effect is independent of the THz field. Therefore, the relative contribution of the PCI effect diminishes with the THz field strength.

Conversely, in order to experimentally measure the PCI effect, one has to account for the experimental resolution of the spectral line widths with an instrument broadening of $\sim$1 eV.
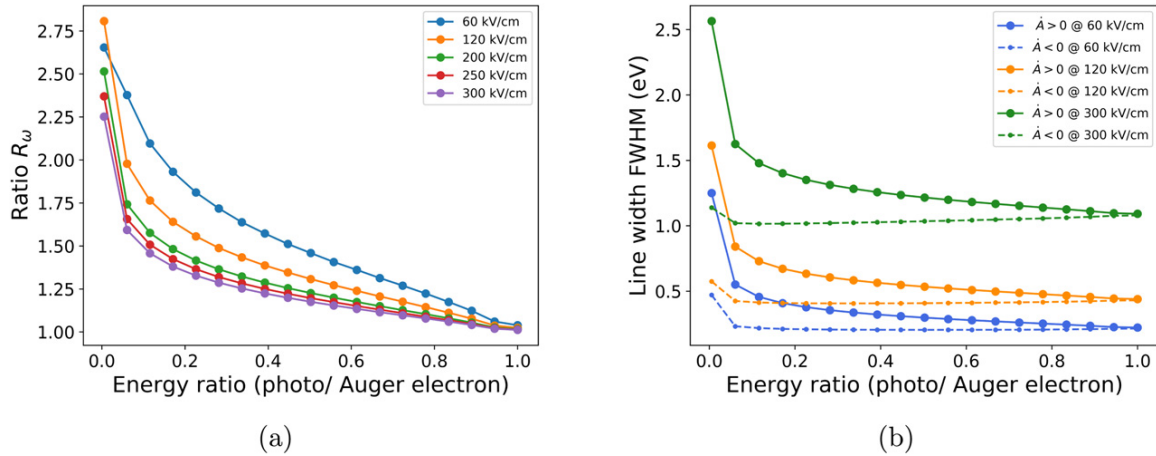
Figure 5. (a) Ratio R_ω for the krypton Auger spectral line $M_5N_1N_{2,3}(^1P_1)$ for different THz streaking field strengths with a photon pulse duration of 20 fs FWHM. (b) Widths in eV of the same krypton spectral line at the rising $\dot{A} > 0$ (solid) and falling $\dot{A} < 0$ (dotted) slope of the THz vector potential. Stronger THz fields streak the pulse more resulting in a broader spectral line.
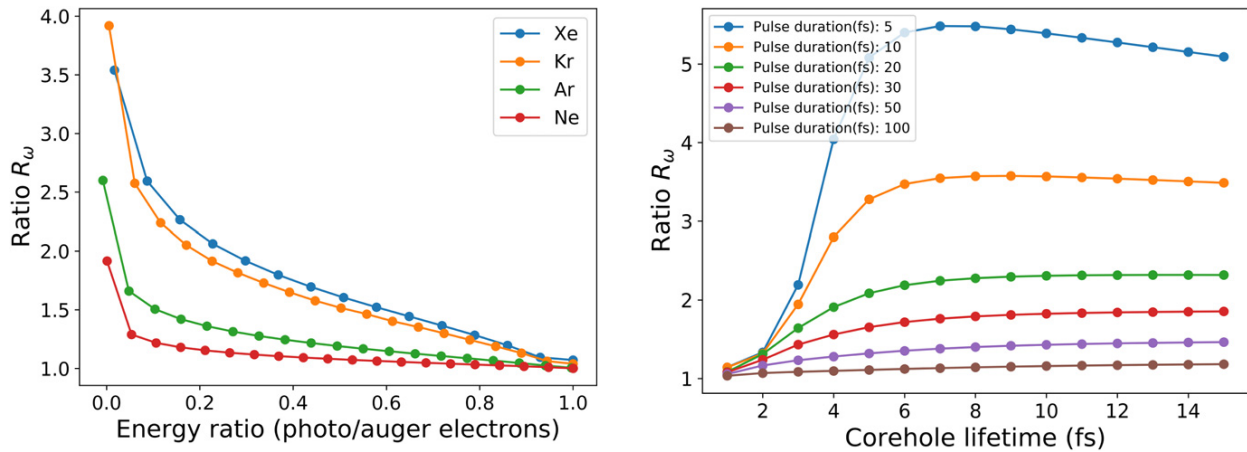

Figure 6. Comparison of the ratio R_ω between xenon, krypton, argon and neon atoms. The calculations were done for a pulse duration of 10 fs and a THz field strength of 120 kV cm^{-1}. The PCI effect is stronger for xenon and krypton atoms compared to argon and neon. The widths' ratio is almost double for the same energy ratio between the photo and Auger electrons. On the other hand, similar behaviour is observed for all of the atoms—the width ratio is maximum for photoelectrons with energy close to zero and it goes to one when both photo and auger electrons have the same energy.

Figure 7. Ratio R_ω of the spectral lines at the rising and falling slopes of the vector potential as a function of its core-hole lifetime. The calculations were done for Auger and photoelectron energies of 30 and 0.5 eV respectively, with a THz field strength of 120 kV cm^{-1} and various photon pulse durations. The PCI effect is negligible (the ratio is one) for relatively short core-hole lifetimes and increases for values longer than 4 fs.

A stronger THz field and thus a broader line width will better resolve the effect. Therefore, the PCI effect (R_ω) together with the experimental resolution is the parameter that has to be optimized.

A comparison between the four considered transitions is shown in figure 6 for an XUV pulse duration of 10 fs and a THz field strength of 120 kV cm^{-1}. It is observed that there is a stronger PCI effect for the xenon and krypton atoms as compared to neon and argon. This can be explained by the different core-hole lifetimes. To show this, calculations at a fixed Auger and photoelectron energies but different core-hole lifetimes ranging from zero to 15 fs were done.

Figure 7 shows the ratio of the spectral line widths at the rising and falling slopes of the THz vector potential for a field strength of 120 kV cm^{-1} and different XUV pulse durations at a photo and Auger electron energies of 0.5 eV and 30 eV respectively. For relatively short core-hole lifetimes, the PCI effect is negligible (the ratio is almost one) and it increases significantly for core-hole lifetimes longer than 4 fs and reaches 'saturation' at 7 fs. Since the core-hole lifetimes of neon and argon are below 7 fs, the effect is not so pronounced in the results shown in figures 1 and 2 as compared to xenon and krypton (figures 3 and 4).

In the semi-classical approach used in our calculations the electron–electron correlations are not included which might influence the accuracy of the results, especially for

low-energy photoelectrons close to threshold. However, full quantum-mechanical calculations of Auger electron spectrum (without THz field), which take into account electron correlations [14, 16], show excellent agreement with the semi-classical approach also for photoelectrons with very low energy. Moreover, in reference [14] it was shown that the semi-classical approach is valid when the excess energy $E_{ex} > (\Gamma E_A)^{1/2}$, where Γ is the Auger width and E_A the Auger electron energy. For our examples, this condition is satisfied when the ratio of photoelectron and Auger electron energies $E_e/E_A > 0.06$ (Xe), 0.05(Kr), 0.02 (Ar, Ne). Thus, we suppose that our results are accurate practically for the whole considered energy range with an exception of points close to zero.

4. Conclusions

Using the semi-classical analytical model developed in [28], we presented the results of numerical calculations of the PCI effect for different noble gas atoms and various experimental conditions. The results show that there is a stronger effect for transitions with a core-hole lifetime longer than 4 fs, namely xenon and krypton. Furthermore, it is easier to resolve the effect for photon pulse durations shorter than 50 fs FWHM as compared to longer ones. Surprisingly, lower streaking THz field strengths result in a larger ratio R_ω. These results will help future experiments at HHG or FEL sources to tailor experimental conditions, in order to determine a parameter space in which a measurable effect can be expected.

Acknowledgments

Data availability statement

The data that support the findings of this study are available upon reasonable request from the authors.

ORCID iDs

I J Bermúdez Macias https://orcid.org/0000-0002-2842-4230
S Düsterer https://orcid.org/0000-0003-4379-1327
R Ivanov https://orcid.org/0000-0002-6716-5104
U Frühling https://orcid.org/0000-0002-8423-786X
N M Kabachnik https://orcid.org/0000-0003-4458-7643

References

[1] Kuchiev M Y and Sheinerman S A 1989 *Usp. Fiz. Nauk* **158** 353–87
[2] Mehlhorn W 1998 *J. Electron Spectrosc. Relat. Phenom.* **93** 1–15
[3] Schmidt V 1997 *Electron Spectrometry of Atoms Using Synchrotron Radiation* (Cambridge: Cambridge University Press)
[4] Eberhardt W, Bernstorff S, Jochims H W, Whitfield S B and Crasemann B 1988 *Phys. Rev.* A **38** 3808–11
[5] Aksela H, Kivilompolo M, Nõmmiste E and Aksela S 1997 *Phys. Rev. Lett.* **79** 4970–3
[6] Armen G B, Southworth S H, Levin J C, Arp U, LeBrun T and MacDonald M A 1997 *Phys. Rev.* A **56** R1079–82
[7] Lablanquie P, Sheinerman S, Penent F, Hall R I, Ahmad M, Hikosaka Y and Ito K 2001 *Phys. Rev. Lett.* **87** 053001
[8] Hentges R, Müller N, Viefhaus J, Heinzmann U and Becker U 2004 *J. Phys. B: At. Mol. Opt. Phys.* **37** L267–73
[9] Hergenhahn U, Fanis A D, Prümper G, Kazansky A K, Kabachnik N M and Ueda K 2005 *J. Phys. B: At. Mol. Opt. Phys.* **38** 2843–57
[10] Niehaus A 1977 *J. Phys. B: At. Mol. Phys.* **10** 1845–57
[11] Morgenstern R, Niehaus A and Thielmann U 1977 *J. Phys. B: At. Mol. Phys.* **10** 1039–58
[12] Ogurtsov G N 1983 *J. Phys. B: At. Mol. Phys.* **16** L745–8
[13] Russek A and Mehlhorn W 1986 *J. Phys. B: At. Mol. Phys.* **19** 911–27
[14] Armen G B, Tulkki J, Aberg T and Crasemann B 1987 *Phys. Rev.* A **36** 5606–14
[15] Tulkki J, Åberg T, Whitfield S B and Crasemann B 1990 *Phys. Rev.* A **41** 181–5
[16] Kuchiev M Y and Sheinerman S A 1985 *J. Phys. B: At. Mol. Phys.* **18** L551–6
[17] Sheinerman S A 2003 *J. Phys. B: At. Mol. Opt. Phys.* **36** 4435–46
[18] Kazansky A K and Kabachnik N M 2005 *Phys. Rev.* A **72** 052714
[19] Drescher M *et al* 2002 *Nature* **419** 803–7
[20] Drescher M, Hentschel M, Kienberger R, Uiberacker M, Westerwalbesloh T, Kleineberg U, Heinzmann U and Krausz F 2004 *J. Electron Spectrosc. Relat. Phenom.* **137–140** 259–64 *iCESS-9 Proceedings of the 9th International Conference on Electronic Spectroscopy and Structure*
[21] Uiberacker M *et al* 2007 *Nature* **446** 627–32
[22] Uphues T, Schultze M, Kling M F, Uiberacker M, Hendel S, Heinzmann U, Kabachnik N M and Drescher M 2008 *New J. Phys.* **10** 025009
[23] Krikunova M *et al* 2009 *New J. Phys.* **11** 123019
[24] Verhoef A J, Mitrofanov A V, Nguyen X T, Krikunova M, Fritzsche S, Kabachnik N M, Drescher M and Baltuška A 2011 *Laser Phys.* **21** 1270–4
[25] Zherebtsov S *et al* 2011 *J. Phys. B: At. Mol. Opt. Phys.* **44** 105601
[26] Schütte B *et al* 2012 *Phys. Rev. Lett.* **108** 253003
[27] Ackermann W *et al* 2007 *Nat. Photon.* **1** 336–42
[28] Bauch S and Bonitz M 2012 *Phys. Rev.* A **85** 053416
[29] Trinter F *et al* 2013 *Phys. Rev. Lett.* **111** 093401
[30] Ivanov R, Liu J, Brenner G, Brachmanski M and Düsterer S 2018 *J. Synchrotron Radiat.* **25** 26–31
[31] Ivanov R *et al* 2020 *J. Phys. B: At. Mol. Opt. Phys.* **53** 184004
[32] Kazansky A K, Sazhina I P and Kabachnik N M 2009 *J. Phys. B: At. Mol. Opt. Phys.* **42** 245601
[33] Frühling U 2011 *J. Phys. B: At. Mol. Opt. Phys.* **44** 243001

[34] Stolterfoht N, Gabler H and Leithäuser U 1973 *Phys. Lett.* A **45** 351–2

[35] Goldsztejn G *et al* 2017 *Phys. Rev.* A **96** 012513

[36] Carroll T X, Bozek J D, Kukk E, Myrseth V, Sæthre L J and Thomas T D 2001 *J. Electron Spectrosc. Relat. Phenom.* **120** 67–76

[37] Werme L O, Bergmark T and Siegbahn K 1972 *Phys. Scr.* **6** 141–50

[38] Penent F, Palaudoux J, Lablanquie P, Andric L, Feifel R and Eland J H D 2005 *Phys. Rev. Lett.* **95** 083002

[39] Decking W *et al* 2020 *Nat. Photon.* **14** 391–7

[40] Emma P *et al* 2010 *Nat. Photon.* **4** 641–7

A.4   Time-dependent postcollision interaction effects in THz-field-assisted Auger decay.

Time-dependent post-collision-interaction effects in THz-field-assisted Auger decay

I. J. Bermúdez Macias [1], I. P. Sazhina,[2] R. Ivanov,[1] S. Düsterer [1] and N. M. Kabachnik [1,2,3,4]

[1]*Deutsches Elektronen-Synchrotron DESY, Notkestr. 85, 22607 Hamburg, Germany*
[2]*Skobeltsyn Institute of Nuclear Physics, Lomonosov Moscow State University, Moscow 119991, Russia*
[3]*Donostia International Physics Center (DIPC), E-20018 San Sebastian/Donostia, Spain*
[4]*European XFEL GmbH, Holzkoppel 4, D-22869 Schenefeld, Germany*

The effects of postcollision interaction (PCI) in the time evolution of photoinduced Auger decay, assisted by a terahertz (THz) field, is theoretically investigated. We propose a time-dependent model which is based on the quantum-mechanical description of the photoinduced Auger process and quasiclassical description of the PCI. The suggested model is used for calculating the PCI distortion of the Auger spectrum at different temporal overlaps of the exciting extreme ultraviolet pulse and the streaking THz pulse.

I. INTRODUCTION

The term postcollision interaction (PCI) is used to describe the effects of the interaction of charged particles in the final state of the atomic collision process [1]. In particular, in the photoinduced Auger process, PCI is the interaction between the photoelectron, the Auger electron, and the residual ion [2,3]. The PCI distorts the shape of the Auger line in the spectrum and shifts the position of its maximum. Furthermore, PCI is responsible for the recapture of slow photoelectrons back to the ion. The effects of PCI were widely discussed in experimental [4–9] and theoretical [10–18] works in the '80s and '90s. With the advent of free-electron lasers in the extreme ultraviolet (XUV) and x-ray regions, and of new XUV sources based on high harmonic generation producing ultrashort XUV pulses, the experimental investigation of the time evolution of the Auger decay has become possible [19–25]. Recently, the first time-resolved observation of the PCI effect in Auger decay has been reported [26]. In the experiment, the Auger spectra for the transitions MNN in Kr and NOO in Xe were investigated using a time-resolved pump-probe method. The Auger transitions were induced by ultrashort XUV pulses. The temporal variation of the Auger spectra were measured using a terahertz (THz)-field-driven streak camera. The difference in the dependence of the spectra on the time delay between the XUV and THz pulses on the ascending and descending slopes of the streaking vector potential (an energetic chirp) has been revealed, which was interpreted as the effect of PCI. For the interpretation of the results, the analytical semiclassical approach, developed in Ref. [27], was used.

The quantum mechanical description of the temporal evolution of the field-assisted Auger decay based on the solution of the time-dependent Schrödinger equation has been developed in Refs. [18,28]. However, the application of these approaches for the considered case of Auger transitions in the THz field is practically impossible at present, since the relevant numerical calculations would demand prohibitively long computer time.

To overcome this problem, Bauch and Bonitz [27] solved the relevant 1D Schrödinger equation and also used the Monte Carlo molecular dynamics method based on classical mechanics. They also developed an analytical (quasi)classical model which describes the PCI effects in the THz-assisted Auger transition. The model is applicable at the extreme of the THz electric field (corresponding to zero values of the vector potential), where the electron does not acquire a net kinetic energy shift. Very recently, this analytical model was used to predict the time-dependent PCI effect of the THz-assisted Auger emission in noble gas atoms [29].

In the present paper, we suggest a more rigorous albeit simple quantum mechanical description of PCI effects in the time-resolved Auger process. It is based on the time-dependent theory of the Auger process induced by an ultrashort XUV pulse in the presence of a powerful laser field as developed by Kazansky *et al.* [28]. To include PCI, we use the quasiclassical approach suggested in Ref. [13]. With this model, we are able to investigate the variation of the PCI effect in the time evolution of the Auger spectra as a function of the overlap between the XUV and the THz pulses. Using the proposed model, we calculated the spectra of Auger electrons for MNN transitions in Kr atoms which are most suitable for experimental investigation [29]. The results are compared to the analytical semiclassical model.

In the next section, we describe the suggested model and the approximations used. Section III shows the results of calculations. Conclusions are presented in Sec. IV.

II. BASIC EQUATIONS AND APPROXIMATIONS

A time-dependent theory of Auger decay induced by ultra-short XUV pulses in a strong laser field has been developed in Ref. [28]. It is based on solving a system of time-dependent Schrödinger equations which describes the photoionization of an inner atomic state and the decay of the created vacancy. In this approach, the Auger electron interacting with the strong

laser field is treated in the strong field approximation [30]. Thus the theoretical description is appropriate for the comparatively fast Auger electrons with energies $E_A > 1$ a.u. In Ref. [28], the following closed expression for the probability of Auger electron emission has been obtained for the near threshold photoionization, which predicts rather accurately the shape of the Auger electron spectra for short exciting pulses. In this paper, atomic units are used unless otherwise indicated:.

$$W(\vec{k}_A) = \frac{\Gamma}{8\pi} \left| \int_{t_0}^{\infty} dt \, e^{iQ(\vec{k}_A,t) - \frac{\Gamma}{2}(t-t_0)} \right.$$
$$\left. \times \int_{t_0}^{t} dt' \, e^{i(E_e - i\frac{\Gamma}{2})(t'-t_0) - i(\omega_X + \epsilon_0)t'} \tilde{\mathcal{E}}_X(t') D_{\bar{k}_e} \right|^2, \quad (1)$$

where

$$Q(\vec{k}_A, t) = -\int_{t_0}^{t} \left[-E_A + \frac{1}{2}[\vec{k}_A - \vec{A}_L(t')]^2 \right] dt'. \quad (2)$$

Here $\vec{k}_A$ is the linear momentum of the emitted Auger electron, t_0 is the time when the XUV pulse starts, $\tilde{\mathcal{E}}_X(t')$ is the envelope of the XUV pulse, ω_X is its central frequency, E_e is the photoelectron kinetic energy, $E_e = k_e^2/2$, ϵ_0 is its binding energy in the atom, Γ is the Auger decay width, and $D_{\bar{k}_e}$ is the dipole matrix element characterizing the interaction of the electron with the electromagnetic field of the XUV pulse. The value $Q(\vec{k}_A, t)$ is the phase, related to the Volkov phase [31], accumulated by the Auger electron moving in the THz field which is characterized by the vector potential $\vec{A}_L(t)$, E_A is the nominal energy of the Auger electron. In the derivation of Eq. (1), the interaction of the photoelectron with the THz field is ignored. Expression (1) describes the Auger electron spectrum for arbitrary XUV and THz pulses, both linearly polarized in the same direction. In the following, the matrix element $D_{\bar{k}_e}$ is set equal to unity. The latter assumption means that we ignore the energy dependence of the matrix elements. Thus we can apply this model in an energy interval which is much smaller than the typical energy of the considered Auger electrons. Within this model, only the shape of the Auger spectrum and energy shift can be discussed but not the absolute value of the cross section.

In the above approach, both photoelectron and Auger electron are considered as independent and noninteracting. Therefore, the PCI effects are not included. To take them into account, we use the semiclassical approach as described in Ref. [13]. The main part of the PCI is considered to be induced by the change of the screening of the ionic core, which is felt by both electrons when the fast Auger electron overtakes the slower photoelectron. This change of the screening leads to an increase of the energy of the Auger electron and, correspondingly, to a decrease of the photoelectron's energy. If one denotes the total energy gained by the Auger electron in PCI as $S_A(t)$, then the outgoing Auger electron will be observed at an energy $E = E' + S_A(t)$, where

$$E' = k_A^2/2 = E - S_A(t) \quad (3)$$

denotes the energy of the electron ignoring PCI.

In the semiclassical approach, the term $S_A(t)$ may be calculated as $S_A(t) = 1/r^*(t)$, where r^* is the distance from the ion nucleus to the point where the Auger electron overtakes

the photoelectron. With sufficient accuracy, it is given as [12] (see also Ref. [27])

$$r^* = t p_r + \delta r^*, \quad (4)$$

with $p_r = k_A k_e/(k_A - k_e + A_L(t_0) - A_L(t))$. The value δr^* is a small correction depending on the radii of the initial and the final electron subshells involved [27]:

$$\delta r^* = \frac{(k_A - A_L(t))R_e - (k_e - A_L(t_0))R_A - A_L(t)(R_A - R_e)}{k_A - k_e + A_L(t_0) - A_L(t)}. \quad (5)$$

Here $A_L(t) = |\vec{A}_L(t)|$, $k_A = |\vec{k}_A|$, R_A, and R_e are the radii of the initial subshells of the Auger and the photoelectron, respectively.

Note that the energy gain $S_A(t)$ depends on the emission time of the Auger electron. At larger t, the Auger electron overtakes the photoelectron at a larger distance from the nucleus, and therefore the energy gain by the Auger electron is smaller.

We further assume that the Auger electron is detected along the polarization direction. Taking into account that $E_e \approx \omega_X + \epsilon_0$, we obtain from Eq. (1) the final expression

$$W(E) = \frac{\Gamma}{8\pi} \left| \int_{t_0}^{\infty} dt \, e^{iQ(E,t) - \frac{\Gamma}{2}(t-t_0)} \int_{t_0}^{t} dt' \, e^{\frac{\Gamma}{2}(t'-t_0)} \tilde{\mathcal{E}}_X(t') \right|^2 \quad (6)$$

with the phase

$$Q(E, t) = -\int_{t_0}^{t} \Big[-E_A + E - S_A(t') \mp k_A A_L(t') $$
$$+ A_L^2(t')/2 \Big] dt', \quad (7)$$

where the minus (plus) sign corresponds to the detection of Auger electron in the (opposite) direction of the vector potential.

This expression reduces to that obtained by Russek and Mehlhorn [13] if we take $A_L(t) = 0$ and assume that the XUV pulse is very short (delta function). On the other side, if we ignore the $S_A(t)$ term, we return to Eq. (1), which describes the Auger electron spectrum induced by a short XUV pulse.

III. RESULTS AND DISCUSSION

In this section, we show some results of the calculations using the theoretical model introduced above, which illustrates the PCI effect for different conditions. In particular, we compare the influence of PCI to the streaking effect in the presence of a THz field. In all calculations, we use the model THz vector potential described by the analytical expression

$$A_L(t) = A_0 \exp\left(-t^2/2\sigma_L^2\right) \cos(2\pi t/T_L),$$
$$-0.75\, T_L < t < 0.75\, T_L. \quad (8)$$

Here A_0 and T_L are the amplitude and period of the THz field vector potential. This vector potential is similar to the vector potential of the single-cycle THz field used in experiments [32]. The ionizing XUV pulse is described by a Gaussian envelope of the electric field,

$$\tilde{\mathcal{E}}_X(t) = \exp\left(-(t - t_d)^2/2\sigma_X^2\right), \quad (9)$$
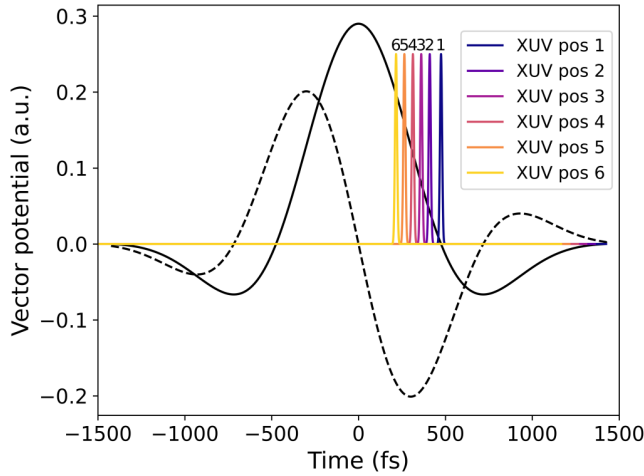
FIG. 1. Vector potential of the THz field in atomic units (black solid curve) and the XUV pulses (in arbitrary units) used in the calculations as a function of time in fs. The position of the maximum of the x-ray pulse for several delay times used in the calculations is indicated by numbers. The dashed line shows the corresponding THz electric field in atomic units multiplied by 10^4.
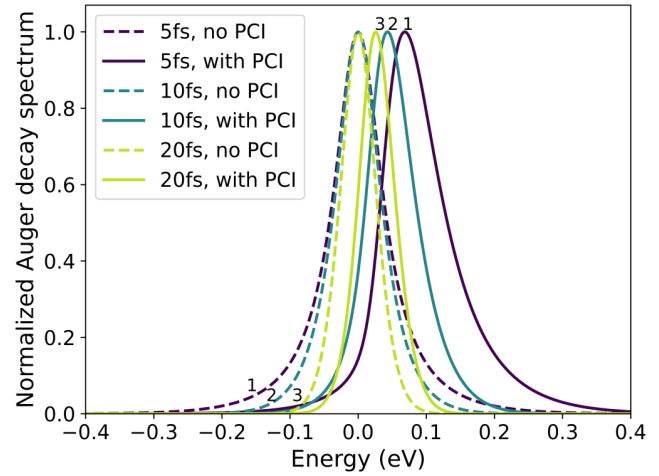

FIG. 2. The shape of the Auger line calculated with (solid curves) and without (dashed curves) PCI effect for different pulse duration (FWHM) of the exciting XUV pulse: 5 fs (lines 1), 10 fs (lines 2), 20 fs (lines 3). The excess energy is 0.5 eV. The spectral lines are normalized to unity in the maximum, the energy scale is relative to the nominal Auger electron energy, E_A.

with intensity full width at half maximum (FWHM) = $2\sqrt{\ln 2}\sigma_X$ and a time-delay t_d with respect to the maximum of $A_L(t)$. Figure 1 shows the used vector potential with amplitude $A_0 = 0.29$ a.u., $\sigma_L = 475$ fs and period $T_L = 1900$ fs, which corresponds to a THz field with the central frequency of 0.53 THz and a field strength of 120 kV/cm. In the same figure, we show the relative positions of six different Gaussian XUV pulses of 10 fs duration (FWHM). Position 1 corresponds to the zero crossing of the vector potential, while positions 2–6 are located on the decreasing slope of it.[1]

As a target atom, we have chosen Kr and considered the MNN Auger transitions which are well investigated experimentally [33,34]. In particular, we have chosen the transition $M_5N_1N_{2,3}(^1P_1)$, resulting in an Auger electron at an energy of 37.7 eV [34]. The corresponding radii of the orbits were taken from Hartree-Fock calculations to be $R_e = 0.538$ a.u. and $R_A = 1.952$ a.u. The threshold energy for Kr $(3d_{5/2})$ ionization is 93.8 eV [35]. The Auger lifetime for this transition is $\tau = 7.5$ fs, $\Gamma = 88$ meV [36]. As shown in Ref. [29], the Kr MNN Auger transition is a good candidate for future experimental investigations of the PCI effects in Auger decays.

A. Auger line shape distorted by PCI in absence of THz field

Let us first consider the PCI effects in the Auger process generated by a short XUV pulse in the absence of the THz field ($A_L(t) = 0$). As is well-known, PCI affects the shape of the Auger spectral line and the position of its maximum. In Fig. 2, we show the shape of the line in the Auger spectrum calculated using expression (6) with and without PCI effect

for different XUV pulse durations of 5 fs, 10 fs, and 20 fs for the excess energy 0.5 eV (energy of the photoelectron). In earlier calculations of PCI effect for Auger transitions (see Ref. [13] and references therein), a prompt ionization was assumed, which corresponds to an ultrashort XUV pulse $\tau_{XUV} \to 0$. In contrast, Fig. 2 shows that the shape of the Auger line depends on the duration of the XUV pulse. The width of the lines for nonzero τ_{XUV} is determined not only by the Auger width but also by the energy spread of the ionizing pulse. When the PCI effect is ignored, the maximum of the Auger line is at the nominal energy of the Auger electron. Its width diminishes by increasing the pulse duration. The PCI shifts the maximum and changes the shape of the line. By increasing the XUV pulse duration, the relative influence of the PCI diminishes. Furthermore, the energy shift becomes smaller and the line shape approaches a Gaussian shape which is determined by the Gaussian shape of the XUV pulse. If the pulse [Eq. (9)] is not Gaussian, the Auger line shape will depend on the XUV pulse shape.

In Fig. 3, we show the calculated Auger line shapes for one duration of the exciting XUV pulse (5 fs) but for different excess energies (kinetic energy of photoelectron) of 0.5 eV, 2.5 eV, 5 eV, and 10 eV. In accordance with Ref. [13], the maximum distortion and maximum energy shift occur at smaller excess energy (see inner figure). By increasing the excess energy, the shift decreases and the line shape becomes close to a Lorentzian shape.

B. Influence of THz field on Auger line shape including PCI

When the THz field is switched on, the Auger spectrum is modified by the streaking effect and this effect strongly depends on the time delay between the THz and the XUV pulses. In Fig. 4, we compare the spectra for one and the same XUV pulse duration (10 fs) and one value of excess energy (1 eV) but for different time delays, as shown in Fig. 1. Note

---

[1]Note that our definition of vector potential differs by sign from that used in Ref. [27]. Therefore, also the terms rising slope and falling slope of the vector potential are interchanged.
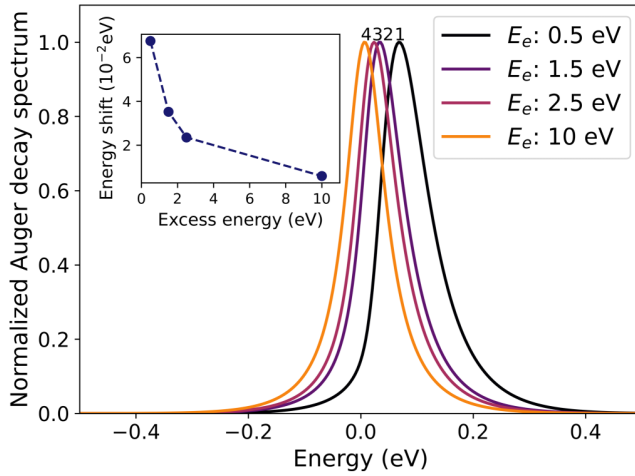
FIG. 3. The shape of the Auger line calculated taking into account the PCI effect for an XUV pulse duration of 5 fs and different excess energies 0.5 eV (line 1), 1.5 eV (line 2), 2.5 eV (line 3), and 10 eV (line 4). The spectral lines are normalized to unity in the maxima, the energy scale is relative to the nominal Auger electron energy, E_A. The inner figure shows the absolute energy shift of the peak of each Auger line as a function of the excess energy E_e. The dashed line is used to guide the eyes.

that the spectra presented in Fig. 4 are not normalized. They are shown in arbitrary units but the units are the same for all spectra. The shown spectra are calculated taking the PCI effect into account (solid lines) and ignoring the PCI effect (dashed lines). The presence of only the THz field shifts the position of the Auger line and changes its width. In addition, the PCI effect distorts and shifts the spectral line as well. Both the streaking and PCI change the width of the Auger line which makes the observation of the PCI effect and its quantitative investigation even more complicated.

In the experiment [26], the shapes of the lines in the spectra of Auger electrons streaked by the THz field have been studied for opposite directions of Auger electron emission: along the polarization of both XUV and THz fields and opposite to it. This is equivalent to studying the streaking at the descending and at the ascending slopes of the vector potential. In Fig. 4(a), we present the results of the calculations for the emission angle $\theta = 0$, i.e., along the polarization, while Fig. 4(b) shows the results for $\theta = \pi$. Spectrum 1 corresponds to the XUV pulse position close to zero vector potential (see Fig. 1). The maximum of the Auger line is close to the nominal position and the line is broadened. Spectra 2–6 show a large energy shift due to interaction with the THz field. On the descending slope of the vector potential, the Auger electron peak in the forward direction is shifted to higher energies and becomes broader. In the backward direction, the peak is shifted to smaller energies and becomes narrower. In both cases, the PCI effect shifts the peak to higher energies and makes it broader.

It is interesting to discuss the variation of the peak widths as a function of the time delay in more detail. Since the spectra presented in Fig. 4 are calculated for the same transition but for different time delays, they only differ by the interaction with the THz field. Thus, the total number of emitted Auger
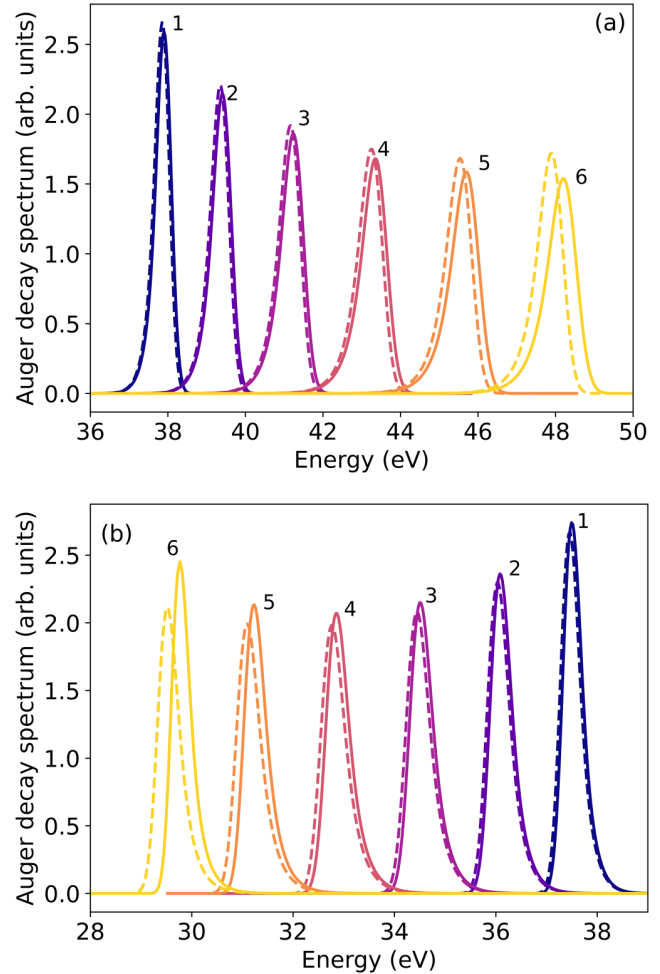

FIG. 4. Spectra of the Auger decay in the THz field calculated including the PCI effect (solid lines) and without PCI (dashed lines) for an XUV pulse duration of 10 fs, for an excess energy of 1 eV and for different time delays between the XUV and the THz field. The numbers near the peaks indicate the XUV pulse position as shown in Fig. 1. (a) Auger electrons detected in forward direction, (b) Auger electrons detected in the backward direction.

electrons (the area under the peak) is the same, and a larger value in the maximum of the spectrum corresponds to a smaller width. Consider first the case without PCI (dashed curves) at Fig. 4(a). One sees that going from spectrum 1 to spectrum 6 (decreasing the time delay), the width of the line first increases and then starts to decrease. The widths of the spectra in Fig. 4(b) also show a similar behavior. This modulation of the width due to streaking can be explained as follows. From the classical theory of streaking [32,37], one knows that the width of the line acquired due to streaking is proportional to the time derivative of the streaking THz vector potential, corresponding to the THz electric field. The latter is presented in Fig. 1 for the chosen vector potential as a dashed curve. The variation of the spectral widths in Fig. 4 follows the change of the derivative of the vector potential.

In Ref. [29], we suggested characterizing the influence of the PCI effects by the ratio of the Auger line widths for opposite emission directions $\theta = 0$ and $\theta = \pi$. It was
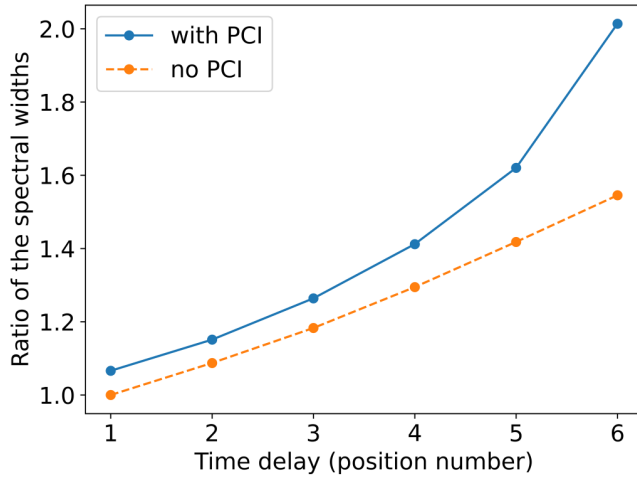
FIG. 5. The ratio of the widths of the Auger line calculated for emission in forward and backward directions as a function of delay. The points in the solid curve (upper line) were calculated with PCI, the points in the dashed curve (lower line) without PCI. The parameters of the pulses are the same as in Fig. 4. The lines are drawn to guide the eyes.

shown that the ratio of the widths, which can be measured in an experiment, is sensitive to the PCI effect. To obtain such ratio, we fitted the streaked Auger lines by the Gaussian curves and determined their width and the ratio. The resulting ratios are shown in Fig. 5 for different time delays.

Qualitatively, the influence of the PCI on the streaked Auger line width and their ratio may be explained as follows. Considering expression (6) for the Auger line shape, the phase $Q(E, t)$ in the first integral is quickly varying. To approximately evaluate the integral, one can use the saddle point approximation [37]. The saddle point is defined by the condition $\frac{\partial Q(E,t)}{\partial t}|_{t=t_s} = 0$, which gives the relation

$$-E_A + E - S_A(t_s) \mp k_A A_L(t_s) + A_L^2(t_s)/2 = 0. \quad (10)$$

Here the minus (plus) sign corresponds to emission in the forward (backward) direction. For the considered experiments, $k_A \gg A_L(t)$. Solving the above equation, we find

$$k_A = \sqrt{2[E_A + S_A(t_s)]} \pm A_L(t_s). \quad (11)$$

Equation (10) links the final momentum k_A, and hence the final Auger electron energy $E = \frac{k_A^2}{2}$, with the time of the Auger electron emission t_s. It qualitatively explains the evolution of the Auger spectral line with the time delay. Going from delay point 1 to point 6, the vector potential increases, thus the Auger energy on the right slope [plus sign in (11)] also increases while on the left slope it decreases. Using Eq. (11), one can also estimate the width of the spectral line for different delays:

$$\delta E = k_A \delta k_A \approx k_A |dA_L(t_s)/dt \pm E_A^{-1/2} dS_A(t_s)/dt|\delta t. \quad (12)$$

If one ignores PCI [$S_A(t) = 0$], then the width is determined by the derivative of vector potential. It is increasing (modulus) by changing the delay from position 1 to 6. Besides, k_A also changes with the time delay. The ratio of widths in the forward

and backward directions is

$$\delta E_+/\delta E_- = \frac{\sqrt{2E_A} + A_L(t_s)}{\sqrt{2E_A} - A_L(t_s)} \approx 1 + 2\frac{A_L(t_s)}{\sqrt{2E_A}}. \quad (13)$$

The ratio is increasing going from point 1 to point 6 (see dashed curve in Fig. 5).

When PCI is taken into account, it gives a contribution to the widths. As we already discussed, the energy gain $S_A(t)$ diminishes with t, thus the derivative $dS_A(t)/dt$ is negative. On the right slope [forward emission, plus sign in Eq. (12)], the derivative of the vector potential is negative, therefore both terms in Eq. (12) have the same sign; the width is increasing due to PCI. On the contrary, on the left slope [minus sign in Eq. (12)], the PCI diminishes the width of the line. The resulting ratio, shown in Fig. 5 by the solid curve, increases steeper from delay 1 to delay 6 than the dashed curve calculated without PCI.

The above calculations have been done for the THz field strength 120 kV/cm and frequency 0.53 THz. To investigate the influence of the PCI on the line shape at different frequencies of the streaking field, we made calculations for the same field strengths but varying the frequencies. The results are shown in Fig. 6. Remember that in the analytical semiclassical model suggested in Ref. [27], the streaked Auger spectrum does not depend on THz frequency. Indeed, the spectrum is considered when the XUV pulse is set at zero vector potential. Then the main parameter which determines the influence of the THz field is the time derivative of the vector potential which is actually the THz electric field. Thus, according to the semiclassical model, for the fixed strength of the THz field, the results should not depend on the frequency. We have verified this prediction using our model. The results are shown in Fig. 6(a). The calculations made for 0.53 THz, 1.05 THz, and 2.1 THz give almost identical results for both the shape and the position of the maximum. Naturally, at other delays the vector potential is nonzero and therefore the position of the Auger spectral line depends on the delay while the width is determined not only by the PCI but also by the streaking. Since the vector potential scales as E_L/ω_L for a fixed THz field strength, it depends on the frequency. Therefore, the line shape and position depend on the frequency as well, as shown in Fig. 6(b).

C. Comparison of the quantum and analytical semiclassical models

Finally, we compare the results of the calculations made using the suggested model, based on the quantum-mechanical approach, with the results of the analytical semiclassical model [27,29]. Remember that in the latter model, simple analytical expressions for the spectral line shape for an infinitesimal XUV pulse duration have been suggested [27]. For a positive derivative of the streaking electric field $\dot{A}_L > 0$, the spectral line shape $f_+(\epsilon)$ is presented as

$$f_+(\epsilon) = \Gamma_4 \frac{k_+ - \epsilon_-}{k_+} e^{-\Gamma_4(k_+ - \epsilon_+)}, \quad (14)$$

FIG. 7. The widths of the Auger line calculated for the emission in the forward (solid lines) and the backward (dashed lines) directions as a function of the ratio of the excess and Auger electron energies. The calculations have been performed for the zero crossing point of the THz vector potential. The result of the calculations using the present quantum mechanical model are shown as black lines, the results of the analytical semiclassical model of Ref. [29] are shown as red lines (lighter gray). The calculations have been done for an XUV pulse duration of 5 fs for an excess energy of 1 eV and THz field strength of 60 kV/cm.

[27]. As a typical example, in Fig. 7 we show the dependence of the Auger line widths for the emission in forward and backward directions on the energy ratio of photo and Auger electrons for the case of an XUV pulse duration of 5 fs and an excess energy of 1 eV at a THz field of 60 kV/cm. The calculations using the quantum model have been performed for a time delay close to the zero-crossing of vector potential where the analytical model is valid. The classical analytical model predicts much broader lines and a considerably larger difference between widths as compared to the quantum model (larger PCI effect).

We note that both models use approximations which are, however, significantly different. In the analytical model [27], the time-to-energy mapping is calculated using a classical description of the Auger electron motion. The energy gained by the Auger electron, due to the change of screening when it overtakes the photoelectron, is added to its classical energy. In the present quantum model, the Auger decay is described quantum mechanically where the energy gain is added to the phase of the Auger electron. Furthermore, the method of averaging over the XUV pulse duration is significantly different for the two models. In the quantum model we consider, in accordance with the rules of quantum mechanics, the amplitude of the Auger emission induced by the finite XUV pulse is calculated, which is then squared to obtain the probability. In contrast, in the analytical model [27], the probability of the Auger emission is calculated for an infinitesimally short XUV pulse, which is then convoluted with the spectral distribution of the finite pulse. The latter approach corresponds to the so-called *ad hoc* model, based on the rate equations. (See discussion, for example, in Refs. [38,39]). Therefore, it is not
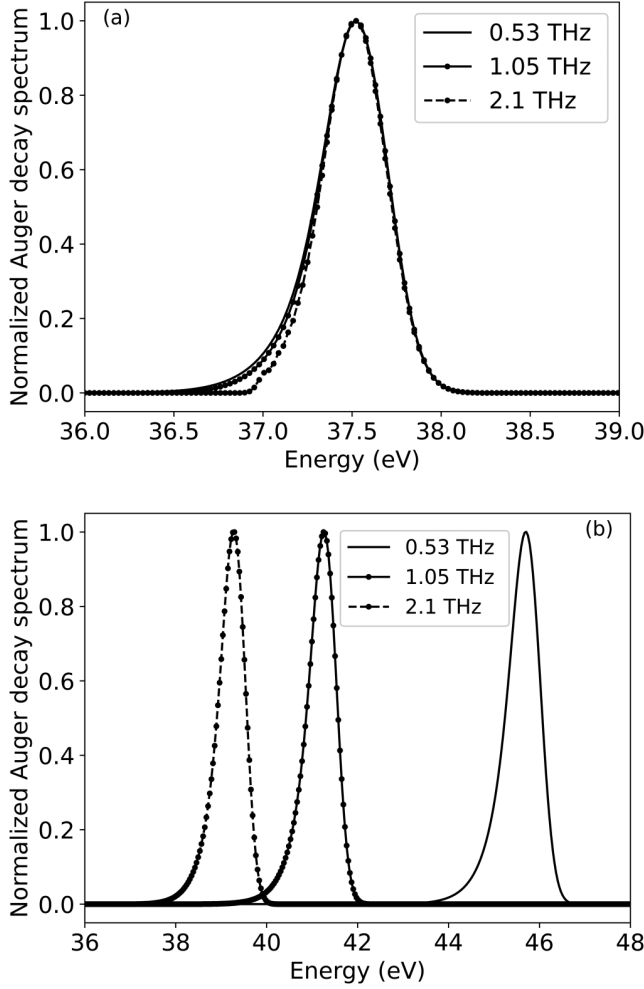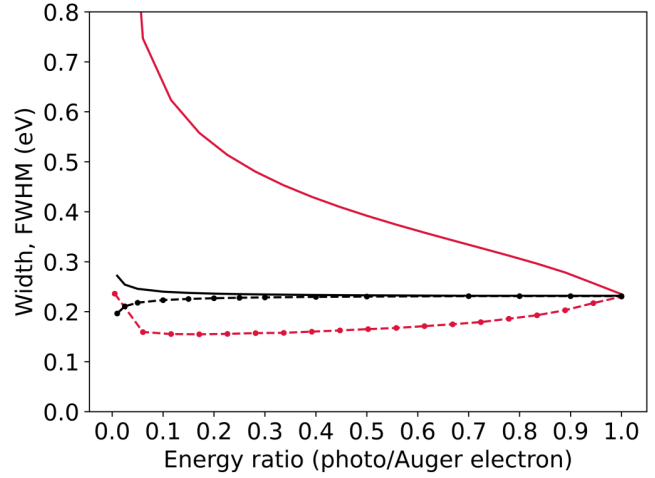
FIG. 6. (a) The shape of the Auger line in the THz field calculated taking into account the PCI effect for the XUV pulse close to the zero crossing of vector potential (position 1 in Fig. 1), for three different THz frequencies 0.53 THz (solid line), 1.05 THz (dotted line), and 2.1 THz (dashed line). An XUV pulse duration of 10 fs, excess energy of 0.5 eV, and THz field strength of 120 kV/cm have been used in the calculations. (b) shows the same as in (a) but for the time delay corresponding to position 5 in Fig. 1.

where $\Gamma_4 = |\alpha|\Gamma$ with $\alpha = (2k_A \dot{A}_L)^{-1}$. For negative values of $\dot{A}_L < 0$, the spectral line shape is

$$f_-(\epsilon) = 2\Gamma_4 e^{-\Gamma_4 \epsilon_+} \left(\frac{\epsilon_-}{k_-} \cosh \Gamma_4 k_- - \sinh \Gamma_4 k_- \right). \quad (15)$$

In these equations, $k_\pm = \sqrt{\epsilon_-^2 \pm |\beta|}$, $\epsilon_\pm = \epsilon \pm \frac{\beta}{4}\delta r^*$ with $\beta = 4k_A \dot{A}_L / p_r$. To obtain the Auger spectrum for a finite pulse duration τ_X, one convolutes these spectral line shapes with the streaked energy spectrum $f_X(\hat{\epsilon})$ due to the finite XUV pulse duration:

$$W(E) = \int_{-\infty}^{+\infty} d\hat{\epsilon}\, f_X(\hat{\epsilon}) f_\pm(E - \hat{\epsilon}). \quad (16)$$

Here $f_X(\hat{\epsilon}) = (\sqrt{\pi}\Gamma_X)^{-1} \exp(-\hat{\epsilon}^2/\Gamma_X^2)$, with $\Gamma_X = k_A \dot{A}_L \tau_X$. For a more detailed description of the semiclassical analytical model, the reader is referred to the paper by Bauch and Bonitz

surprising that the calculated Auger widths are different in the two models.

IV. CONCLUSION

We presented a theoretical model which combines a fully quantum mechanical description of the time-dependent Auger process induced by an ultrashort XUV pulse in the presence of a THz field, with the quasiclassical description of PCI. The model enables the investigation of the time evolution of PCI effects experienced by Auger electrons in a THz field. We analyzed the dependence of the PCI distorted Auger spectra on the pulse duration of the exciting XUV pulse as well as the effect of PCI on the spectra of Auger electrons in the presence of a THz field. An advantage of the suggested model is that it can be used for any time delay between the exciting XUV

and probing THz pulses. The quantum mechanical results are compared to the results of an analytical (semi)classical model [27]. We show that the latter model predicts considerably larger PCI effects in THz streaking spectra as compared to the present quantum model. Further theoretical efforts as well as new experiments devoted to the investigation of the time evolution of PCI effects would be very desirable.

[1] M. Y. Kuchiev and S. A. Sheinerman, Usp. Fiz. Nauk **158**, 353 (1989).

[2] W. Mehlhorn, J. Electron. Spectrosc. Relat. Phenom. **93**, 1 (1998).

[3] V. Schmidt, *Electron Spectrometry of Atoms using Synchrotron Radiation* (Cambridge University Press, Cambridge, 1997).

[4] W. Eberhardt, S. Bernstorff, H. W. Jochims, S. B. Whitfield, and B. Crasemann, Phys. Rev. A **38**, 3808 (1988).

[5] H. Aksela, M. Kivilompolo, E. Nõmmiste, and S. Aksela, Phys. Rev. Lett. **79**, 4970 (1997).

[6] G. B. Armen, S. H. Southworth, J. C. Levin, U. Arp, T. LeBrun, and M. A. MacDonald, Phys. Rev. A **56**, R1079 (1997).

[7] P. Lablanquie, S. Sheinerman, F. Penent, R. I. Hall, M. Ahmad, Y. Hikosaka, and K. Ito, Phys. Rev. Lett. **87**, 053001 (2001).

[8] R. Hentges, N. Mller, J. Viefhaus, U. Heinzmann, and U. Becker, J. Phys. B: At., Mol. Opt. Phys. **37**, L267 (2004).

[9] U. Hergenhahn, A. De Fanis, G. Prmper, A. K. Kazansky, N. M. Kabachnik, and K. Ueda, J. Phys. B: At., Mol. Opt. Phys. **38**, 2843 (2005).

[10] A. Niehaus, J. Phys. B: At. Mol. Phys. **10**, 1845 (1977).

[11] R. Morgenstern, A. Niehaus, and U. Thielmann, J. Phys. B: At. Mol. Phys. **10**, 1039 (1977).

[12] G. N. Ogurtsov, J. Phys. B: At. Mol. Phys. **16**, L745 (1983).

[13] A. Russek and W. Mehlhorn, J. Phys. B: At. Mol. Phys. **19**, 911 (1986).

[14] G. B. Armen, J. Tulkki, T. Aberg, and B. Crasemann, Phys. Rev. A **36**, 5606 (1987).

[15] J. Tulkki, T. Åberg, S. B. Whitfield, and B. Crasemann, Phys. Rev. A **41**, 181 (1990).

[16] M. Y. Kuchiev and S. A. Sheinerman, J. Phys. B: At. Mol. Phys. **18**, L551 (1985).

[17] S. A. Sheinerman, J. Phys. B: At., Mol. Opt. Phys. **36**, 4435 (2003).

[18] A. K. Kazansky and N. M. Kabachnik, Phys. Rev. A **72**, 052714 (2005).

[19] M. Drescher, M. Hentschel, R. Kienberger, M. Uiberacker, V. Yakovlev, A. Scrinzi, T. Westerwalbesloh, U. Kleineberg, U. Heinzmann, and F. Krausz, Nature (London) **419**, 803 (2002).

[20] M. Drescher, M. Hentschel, R. Kienberger, M. Uiberacker, T. Westerwalbesloh, U. Kleineberg, U. Heinzmann, and

F. Krausz, J. Electron. Spectrosc. Relat. Phenom. **137-140**, 259 (2004).

[21] M. Uiberacker, T. Uphues, M. Schultze, A. J. Verhoef, V. Yakovlev, M. F. Kling, J. Rauschenberger, N. M. Kabachnik, H. Schröder, M. Lezius, K. L. Kompa, H. G. Muller, M. J. J. Vrakking, S. Hendel, U. Kleineberg, U. Heinzmann, M. Drescher, and F. Krausz, Nature (London) **446**, 627 (2007).

[22] T. Uphues, M. Schultze, M. F. Kling, M. Uiberacker, S. Hendel, U. Heinzmann, N. M. Kabachnik, and M. Drescher, New J. Phys. **10**, 025009 (2008).

[23] M. Krikunova, T. Maltezopoulos, A. Azima, M. Schlie, U. Frhling, H. Redlin, R. Kalms, S. Cunovic, N. M. Kabachnik, M. Wieland, and M. Drescher, New J. Phys. **11**, 123019 (2009).

[24] A. J. Verhoef, A. V. Mitrofanov, X. T. Nguyen, M. Krikunova, S. Fritzsche, N. M. Kabachnik, M. Drescher, and A. Baltuška, Laser Phys. **21**, 1270 (2011).

[25] S. Zherebtsov, A. Wirth, T. Uphues, I. Znakovskaya, O. Herrwerth, J. Gagnon, M. Korbman, V. S. Yakovlev, M. J. J. Vrakking, M. Drescher, and M. F. Kling, J. Phys. B: At., Mol. Opt. Phys. **44**, 105601 (2011).

[26] B. Schütte, S. Bauch, U. Frühling, M. Wieland, M. Gensch, E. Plönjes, T. Gaumnitz, A. Azima, M. Bonitz, and M. Drescher, Phys. Rev. Lett. **108**, 253003 (2012).

[27] S. Bauch and M. Bonitz, Phys. Rev. A **85**, 053416 (2012).

[28] A. K. Kazansky, I. P. Sazhina, and N. M. Kabachnik, J. Phys. B: At., Mol. Opt. Phys. **42**, 245601 (2009).

[29] I. J. Bermúdez Macias, S. Dsterer, R. Ivanov, U. Frhling, and N. M. Kabachnik, J. Phys. B: At., Mol. Opt. Phys. **54**, 085601 (2021).

[30] L. V. Keldysh, Sov. Phys. - JETP **20**, 1307 (1965).

[31] D. M. Wolkow, Z. Phys. **94**, 250 (1935).

[32] R. Ivanov, I. J. Bermúdez Macias, J. Liu, G. Brenner, J. Roensch-Schulenburg, G. Kurdi, U. Frhling, K. Wenig, S. Walther, A. Dimitriou, M. Drescher, I. P. Sazhina, A. K. Kazansky, N. M. Kabachnik, and S. Dsterer, J. Phys. B: At., Mol. Opt. Phys. **53**, 184004 (2020).

[33] W. Mehlhorn, W. Schmitz, and D. Stalherm, Z. Phys. **252**, 399 (1972).

[34] L. O. Werme, T. Bergmark, and K. Siegbahn, Phys. Scr. **8**, 149 (1973).

[35] G. King, M. Tronc, F. Read, and R. Bradford, J. Phys. B: At. Mol. Phys. **10**, 2479 (1977).

[36] M. Jurvansuu, A. Kivimäki, and S. Aksela, Phys. Rev. A **64**, 012502 (2001).

[37] J. Itatani, F. Quéré, G. L. Yudin, M. Y. Ivanov, F. Krausz, and P. B. Corkum, Phys. Rev. Lett. **88**, 173903 (2002).

[38] O. Smirnova, V. S. Yakovlev, and A. Scrinzi, Phys. Rev. Lett. **91**, 253001 (2003).

[39] D. C. Haynes, M. Wurzer, A. Schletter, A. Al-Haddad, C. Blaga, C. Bostedt, J. Bozek, H. Bromberger, M. Bucher, A. Camper, S. Carron, R. Coffee, J. T. Costello, L. F. DiMauro, Y. Ding, K. Ferguson, I. Grguraš, W. Helml, M. C. Hoffmann, M. Ilchen *et al.*, Nat. Phys. **17**, 512 (2021).

References

[1] W. Ackermann, G. Asova, V. Ayvazyan, A. Azima, N. Baboi, J. Bähr, V. Balandin, B. Beut-
ner, A. Brandt, A. Bolzmann, R. Brinkmann, O. I. Brovko, M. Castellano, P. Castro,
L. Catani, E. Chiadroni, S. Choroba, A. Cianchi, J. T. Costello, D. Cubaynes, J. Dardis,
W. Decking, H. Delsim-Hashemi, A. Delserieys, G. Di Pirro, M. Dohlus, S. Düsterer,
A. Eckhardt, H. T. Edwards, B. Faatz, J. Feldhaus, K. Flöttmann, J. Frisch, L. Fröhlich,
T. Garvey, U. Gensch, C. Gerth, M. Görler, N. Golubeva, H.-J. Grabosch, M. Grecki,
O. Grimm, K. Hacker, U. Hahn, J. H. Han, K. Honkavaara, T. Hott, M. Hüning,
Y. Ivanisenko, E. Jaeschke, W. Jalmuzna, T. Jezynski, R. Kammering, V. Katalev, K. Ka-
vanagh, E. T. Kennedy, S. Khodyachykh, K. Klose, V. Kocharyan, M. Körfer, M. Kollewe,
W. Koprek, S. Korepanov, D. Kostin, M. Krassilnikov, G. Kube, M. Kuhlmann, C. L. S.
Lewis, L. Lilje, T. Limberg, D. Lipka, F. Löhl, H. Luna, M. Luong, M. Martins, M. Meyer,
P. Michelato, V. Miltchev, W. D. Möller, L. Monaco, W. F. O. Müller, O. Napieral-
ski, O. Napoly, P. Nicolosi, D. Nölle, T. Nuñez, A. Oppelt, C. Pagani, R. Paparella,
N. Pchalek, J. Pedregosa-Gutierrez, B. Petersen, B. Petrosyan, G. Petrosyan, L. Petrosyan,
J. Pflüger, E. Plönjes, L. Poletto, K. Pozniak, E. Prat, D. Proch, P. Pucyk, P. Radcliffe,
H. Redlin, K. Rehlich, M. Richter, M. Roehrs, J. Roensch, R. Romaniuk, M. Ross,
J. Rossbach, V. Rybnikov, M. Sachwitz, E. L. Saldin, W. Sandner, H. Schlarb, B. Schmidt,
M. Schmitz, P. Schmüser, J. R. Schneider, E. A. Schneidmiller, S. Schnepp, S. Schreiber,
M. Seidel, D. Sertore, A. V. Shabunov, C. Simon, S. Simrock, E. Sombrowski, A. A.
Sorokin, P. Spanknebel, R. Spesyvtsev, L. Staykov, B. Steffen, F. Stephan, F. Stulle,
H. Thom, K. Tiedtke, M. Tischer, S. Toleikis, R. Treusch, D. Trines, I. Tsakov, E. Vo-
gel, T. Weiland, H. Weise, M. Wellhöfer, M. Wendt, I. Will, A. Winter, K. Wittenburg,
W. Wurth, P. Yeates, M. V. Yurkov, I. Zagorodnov, and K. Zapfe, "Operation of a free-
electron laser from the extreme ultraviolet to the water window," *Nature Photonics*, vol. 1,
pp. 336–342, Jun 2007.

[2] P. Emma, R. Akre, J. Arthur, R. Bionta, C. Bostedt, J. Bozek, A. Brachmann, P. Bucks-
baum, R. Coffee, F.-J. Decker, Y. Ding, D. Dowell, S. Edstrom, A. Fisher, J. Frisch, S. Gile-
vich, J. Hastings, G. Hays, P. Hering, Z. Huang, R. Iverson, H. Loos, M. Messerschmidt,
A. Miahnahri, S. Moeller, H.-D. Nuhn, G. Pile, D. Ratner, J. Rzepiela, D. Schultz,
T. Smith, P. Stefan, H. Tompkins, J. Turner, J. Welch, W. White, J. Wu, G. Yocky, and
J. Galayda, "First lasing and operation of an ångstrom-wavelength free-electron laser," *Na-
ture Photonics*, vol. 4, pp. 641–647, Sep 2010.

[3] T. Shintake, H. Tanaka, T. Hara, T. Tanaka, K. Togawa, M. Yabashi, Y. Otake, Y. Asano,
T. Bizen, T. Fukui, S. Goto, A. Higashiya, T. Hirono, N. Hosoda, T. Inagaki, S. In-
oue, M. Ishii, Y. Kim, H. Kimura, M. Kitamura, T. Kobayashi, H. Maesaka, T. Masuda,
S. Matsui, T. Matsushita, X. Maréchal, M. Nagasono, H. Ohashi, T. Ohata, T. Ohshima,
K. Onoe, K. Shirasawa, T. Takagi, S. Takahashi, M. Takeuchi, K. Tamasaku, R. Tanaka,
Y. Tanaka, T. Tanikawa, T. Togashi, S. Wu, A. Yamashita, K. Yanagida, C. Zhang, H. Ki-

tamura, and T. Ishikawa, "A compact free-electron laser for generating coherent radiation in the extreme ultraviolet region," *Nature Photonics*, vol. 2, pp. 555–559, Sep 2008.

[4] T. Ishikawa, H. Aoyagi, T. Asaka, Y. Asano, N. Azumi, T. Bizen, H. Ego, K. Fukami, T. Fukui, Y. Furukawa, S. Goto, H. Hanaki, T. Hara, T. Hasegawa, T. Hatsui, A. Higashiya, T. Hirono, N. Hosoda, M. Ishii, T. Inagaki, Y. Inubushi, T. Itoga, Y. Joti, M. Kago, T. Kameshima, H. Kimura, Y. Kirihara, A. Kiyomichi, T. Kobayashi, C. Kondo, T. Kudo, H. Maesaka, X. M. Maréchal, T. Masuda, S. Matsubara, T. Matsumoto, T. Matsushita, S. Matsui, M. Nagasono, N. Nariyama, H. Ohashi, T. Ohata, T. Ohshima, S. Ono, Y. Otake, C. Saji, T. Sakurai, T. Sato, K. Sawada, T. Seike, K. Shirasawa, T. Sugimoto, S. Suzuki, S. Takahashi, H. Takebe, K. Takeshita, K. Tamasaku, H. Tanaka, R. Tanaka, T. Tanaka, T. Togashi, K. Togawa, A. Tokuhisa, H. Tomizawa, K. Tono, S. Wu, M. Yabashi, M. Yamaga, A. Yamashita, K. Yanagida, C. Zhang, T. Shintake, H. Kitamura, and N. Kumagai, "A compact x-ray free-electron laser emitting in the sub-ångström region," *Nature Photonics*, vol. 6, pp. 540–544, Aug 2012.

[5] E. Allaria, R. Appio, L. Badano, W. A. Barletta, S. Bassanese, S. G. Biedron, A. Borga, E. Busetto, D. Castronovo, P. Cinquegrana, S. Cleva, D. Cocco, M. Cornacchia, P. Craievich, I. Cudin, G. D'Auria, M. Dal Forno, M. B. Danailov, R. De Monte, G. De Ninno, P. Delgiusto, A. Demidovich, S. Di Mitri, B. Diviacco, A. Fabris, R. Fabris, W. Fawley, M. Ferianis, E. Ferrari, S. Ferry, L. Froehlich, P. Furlan, G. Gaio, F. Gelmetti, L. Giannessi, M. Giannini, R. Gobessi, R. Ivanov, E. Karantzoulis, M. Lonza, A. Lutman, B. Mahieu, M. Milloch, S. V. Milton, M. Musardo, I. Nikolov, S. Noe, F. Parmigiani, G. Penco, M. Petronio, L. Pivetta, M. Predonzani, F. Rossi, L. Rumiz, A. Salom, C. Scafuri, C. Serpico, P. Sigalotti, S. Spampinati, C. Spezzani, M. Svandrlik, C. Svetina, S. Tazzari, M. Trovo, R. Umer, A. Vascotto, M. Veronese, R. Visintini, M. Zaccaria, D. Zangrando, and M. Zangrando, "Highly coherent and stable pulses from the fermi seeded free-electron laser in the extreme ultraviolet," *Nature Photonics*, vol. 6, pp. 699–704, Oct 2012.

[6] M. Altarelli, "The european x-ray free-electron laser facility in hamburg," *Nuclear Instruments and Methods in Physics Research Section B: Beam Interactions with Materials and Atoms*, vol. 269, no. 24, pp. 2845–2849, 2011. Proceedings of the 10th European Conference on Accelerators in Applied Research and Technology (ECAART10).

[7] B. D. Patterson, R. Abela, H.-H. Braun, U. Flechsig, R. Ganter, Y. Kim, E. Kirk, A. Oppelt, M. Pedrozzi, S. Reiche, L. Rivkin, T. Schmidt, B. Schmitt, V. N. Strocov, S. Tsujino, and A. F. Wrulich, "Coherent science at the SwissFEL x-ray laser," *New Journal of Physics*, vol. 12, p. 035012, mar 2010.

[8] J. Han, H. Kang, I. Ko, *et al.*, "Status of the pal-xfel project," in *Proceedings of 3rd Int. Particle Accelerator Conf*, p. 1735, 2012.

[9] J. Feldhaus, M. Krikunova, M. Meyer, T. Möller, R. Moshammer, A. Rudenko, T. Tschentscher, and J. Ullrich "AMO science at the FLASH and european XFEL free-

electron laser facilities," *Journal of Physics B: Atomic, Molecular and Optical Physics*, vol. 46, p. 164002, aug 2013.

[10] C. Bostedt, S. Boutet, D. M. Fritz, Z. Huang, H. J. Lee, H. T. Lemke, A. Robert, W. F. Schlotter, J. J. Turner, and G. J. Williams, "Linac coherent light source: The first five years," *Rev. Mod. Phys.*, vol. 88, p. 015007, Mar 2016.

[11] S. H. Glenzer, L. B. Fletcher, E. Galtier, B. Nagler, R. Alonso-Mori, B. Barbrel, S. B. Brown, D. A. Chapman, Z. Chen, C. B. Curry, F. Fiuza, E. Gamboa, M. Gauthier, D. O. Gericke, A. Gleason, S. Goede, E. Granados, P. Heimann, J. Kim, D. Kraus, M. J. Mac-Donald, A. J. Mackinnon, R. Mishra, A. Ravasio, C. Roedel, P. Sperling, W. Schumaker, Y. Y. Tsui, J. Vorberger, U. Zastrau, A. Fry, W. E. White, J. B. Hasting, and H. J. Lee, "Matter under extreme conditions experiments at the linac coherent light source," *Journal of Physics B: Atomic, Molecular and Optical Physics*, vol. 49, p. 092001, apr 2016.

[12] H. Wabnitz, L. Bittner, A. R. B. de Castro, R. Döhrmann, P. Gürtler, T. Laarmann, W. Laasch, J. Schulz, A. Swiderski, K. von Haeften, T. Möller, B. Faatz, A. Fateev, J. Feldhaus, C. Gerth, U. Hahn, E. Saldin, E. Schneidmiller, K. Sytchev, K. Tiedtke, R. Treusch, and M. Yurkov, "Multiple ionization of atom clusters by intense soft x-rays from a free-electron laser," *Nature*, vol. 420, pp. 482–485, Dec 2002.

[13] B. Pfau, S. Schaffert, L. Müller, C. Gutt, A. Al-Shemmary, F. Büttner, R. Delaunay, S. Düsterer, S. Flewett, R. Frömter, J. Geilhufe, E. Guehrs, C. M. Günther, R. Hawaldar, M. Hille, N. Jaouen, A. Kobs, K. Li, J. Mohanty, H. Redlin, W. F. Schlotter, D. Stickler, R. Treusch, B. Vodungbo, M. Kläui, H. P. Oepen, J. Lüning, G. Grübel, and S. Eisebitt, "Ultrafast optical demagnetization manipulates nanoscale spin structure in domain walls," *Nature Communications*, vol. 3, p. 1100, Oct 2012.

[14] J. C. H. Spence, U. Weierstall, and H. N. Chapman, "X-ray lasers for structural and dynamic biology," *Reports on Progress in Physics*, vol. 75, p. 102601, sep 2012.

[15] M. Meyer, D. Cubaynes, V. Richardson, J. T. Costello, P. Radcliffe, W. B. Li, S. Düsterer, S. Fritzsche, A. Mihelic, K. G. Papamihail, and P. Lambropoulos, "Two-photon excitation and relaxation of the $3d-4d$ resonance in atomic kr," *Phys. Rev. Lett.*, vol. 104, p. 213001, May 2010.

[16] V. Richardson, J. T. Costello, D. Cubaynes, S. Düsterer, J. Feldhaus, H. W. van der Hart, P. Juranić, W. B. Li, M. Meyer, M. Richter, A. A. Sorokin, and K. Tiedke, "Two-photon inner-shell ionization in the extreme ultraviolet," *Phys. Rev. Lett.*, vol. 105, p. 013001, Jun 2010.

[17] A. Barty, J. Küpper, and H. N. Chapman, "Molecular imaging using x-ray free-electron lasers," *Annual Review of Physical Chemistry*, vol. 64, no. 1, pp. 415–435, 2013. PMID: 23331310.

[18] S. Krinsky and R. L. Gluckstern, "Analysis of statistical correlations and intensity spiking in the self-amplified spontaneous-emission free-electron laser," *Phys. Rev. ST Accel. Beams*, vol. 6, p. 050701, May 2003.

[19] C. Pellegrini and J. Stöhr, "X-ray free-electron lasers—principles, properties and applications," *Nuclear Instruments and Methods in Physics Research Section A: Accelerators, Spectrometers, Detectors and Associated Equipment*, vol. 500, no. 1, pp. 33–40, 2003. NIMA Vol 500.

[20] S. Düsterer, M. Rehders, A. Al-Shemmary, C. Behrens, G. Brenner, O. Brovko, M. DellAngela, M. Drescher, B. Faatz, J. Feldhaus, U. Frühling, N. Gerasimova, N. Gerken, C. Gerth, T. Golz, A. Grebentsov, E. Hass, K. Honkavaara, V. Kocharian, M. Kurka, T. Limberg, R. Mitzner, R. Moshammer, E. Plönjes, M. Richter, J. Rönsch-Schulenburg, A. Rudenko, H. Schlarb, B. Schmidt, A. Senftleben, E. A. Schneidmiller, B. Siemer, F. Sorgenfrei, A. A. Sorokin, N. Stojanovic, K. Tiedtke, R. Treusch, M. Vogt, M. Wieland, W. Wurth, S. Wesch, M. Yan, M. V. Yurkov, H. Zacharias, and S. Schreiber, "Development of experimental techniques for the characterization of ultrashort photon pulses of extreme ultraviolet free-electron lasers," *Phys. Rev. ST Accel. Beams*, vol. 17, p. 120702, Dec 2014.

[21] R. Riedel, A. Al-Shemmary, M. Gensch, T. Golz, M. Harmand, N. Medvedev, M. J. Prandolini, K. Sokolowski-Tinten, S. Toleikis, U. Wegner, B. Ziaja, N. Stojanovic, and F. Tavella, "Single-shot pulse duration monitor for extreme ultraviolet and x-ray free-electron lasers," *Nature Communications*, vol. 4, p. 1731, Apr 2013.

[22] T. Maltezopoulos, S. Cunovic, M. Wieland, M. Beye, A. Azima, H. Redlin, M. Krikunova, R. Kalms, U. Frühling, F. Budzyn, W. Wurth, A. Föhlisch, and M. Drescher, "Single-shot timing measurement of extreme-ultraviolet free-electron laser pulses," *New Journal of Physics*, vol. 10, p. 033026, mar 2008.

[23] C. Behrens, F.-J. Decker, Y. Ding, V. A. Dolgashev, J. Frisch, Z. Huang, P. Krejcik, H. Loos, A. Lutman, T. J. Maxwell, J. Turner, J. Wang, M.-H. Wang, J. Welch, and J. Wu, "Few-femtosecond time-resolved measurements of x-ray free-electron lasers," *Nature Communications*, vol. 5, p. 3762, Apr 2014.

[24] C. Gahl, A. Azima, M. Beye, M. Deppe, K. Döbrich, U. Hasslinger, F. Hennies, A. Melnikov, M. Nagasono, A. Pietzsch, M. Wolf, W. Wurth, and A. Föhlisch, "A femtosecond x-ray/optical cross-correlator," *Nature Photonics*, vol. 2, pp. 165–169, Mar 2008.

[25] M. Harmand, R. Coffee, M. R. Bionta, M. Chollet, D. French, D. Zhu, D. M. Fritz, H. T. Lemke, N. Medvedev, B. Ziaja, S. Toleikis, and M. Cammarata, "Achieving few-femtosecond time-sorting at hard x-ray free-electron lasers," *Nature Photonics*, vol. 7, pp. 215–218, Mar 2013.

[26] U. Frühling, M. Wieland, M. Gensch, T. Gebert, B. Schütte, M. Krikunova, R. Kalms, F. Budzyn, O. Grimm, J. Rossbach, E. Plönjes, and M. Drescher, "Single-shot terahertz-field-driven x-ray streak camera," *Nature Photonics*, vol. 3, pp. 523–528, Sep 2009.

[27] I. Grguraš, A. R. Maier, C. Behrens, T. Mazza, T. J. Kelly, P. Radcliffe, S. Düsterer, A. K. Kazansky, N. M. Kabachnik, T. Tschentscher, J. T. Costello, M. Meyer, M. C. Hoffmann, H. Schlarb, and A. L. Cavalieri, "Ultrafast x-ray pulse characterization at free-electron lasers," *Nature Photonics*, vol. 6, pp. 852–857, Dec 2012.

[28] P. L. Kramer, M. C. Hoffmann, and F. Tavella, "Generation of high-field single-cycle terahertz pulses at 100 khz," in *Conference on Lasers and Electro-Optics*, p. STu3G.4, Optical Society of America, 2020.

[29] R. Ivanov, J. Liu, G. Brenner, M. Brachmanski, and S. Düsterer, "FLASH free-electron laser single-shot temporal diagnostic: terahertz-field-driven streaking," *Journal of Synchrotron Radiation*, vol. 25, pp. 26–31, Jan 2018.

[30] C. Pellegrini and U. /SLAC, "The history of x-ray free-electron lasers," *The European Physical Journal H*, 6 2012.

[31] A. M. Kondratenko and E. L. Saldin, "Generating of coherent radiation by a relativistic electron beam in an ondulator," *Part. Accel.*, vol. 10, pp. 207–216, 1980.

[32] Z. Huang and K.-J. Kim, "Review of x-ray free-electron laser theory," *Phys. Rev. ST Accel. Beams*, vol. 10, p. 034801, Mar 2007.

[33] Z. Huang and K.-J. Kim, "Three-dimensional analysis of harmonic generation in high-gain free-electron lasers," *Phys. Rev. E*, vol. 62, pp. 7295–7308, Nov 2000.

[34] R. Bonifacio, C. Pellegrini, and L. Narducci, "Collective instabilities and high-gain regime in a free electron laser," *Optics Communications*, vol. 50, no. 6, pp. 373–378, 1984.

[35] E. Saldin, E. Schneidmiller, and M. Yurkov, "Statistical properties of radiation from sase fel driven by short electron bunches," *Nuclear Instruments and Methods in Physics Research Section A: Accelerators, Spectrometers, Detectors and Associated Equipment*, vol. 507, no. 1, pp. 101–105, 2003. Proceedings of the 24th International Free Electron Laser Conference and the 9th Users Workshop.

[36] E. Saldin, E. Schneidmiller, and M. Yurkov, *The Physics of Free Electron Lasers*. Advanced Texts in Physics, Springer Berlin Heidelberg, 1999.

[37] J. Rönsch-Schulenburg, E. Hass, A. Kuhl, T. Plath, M. Rehders, J. Rossbach, G. Brenner, C. Gerth, U. Mavric, H. Schlarb, E. Schneidmiller, S. Schreiber, B. Steffen, M. Yan, and M. Yurkov, "Short sase-fel pulses at flash," pp. 379–382, 08 2013.

[38] J. Rönsch-Schulenburg, E. Hass, N. Lockmann, T. Plath, M. Rehders, J. Roßbach, G. Brenner, S. Dziarzhytski, T. Golz, H. Schlarb, *et al.*, "Operation of flash with short sase-fel radiation pulses," 2014.

[39] A. Marinelli, J. MacArthur, P. Emma, M. Guetg, C. Field, D. Kharakh, A. A. Lutman, Y. Ding, and Z. Huang, "Experimental demonstration of a single-spike hard-x-ray free-electron laser starting from noise," *Applied Physics Letters*, vol. 111, no. 15, p. 151101, 2017.

[40] E. Saldin, E. Schneidmiller, and M. Yurkov, "Statistical properties of radiation from vuv and x-ray free electron laser," *Optics Communications*, vol. 148, no. 4, pp. 383–403, 1998.

[41] C. Behrens, N. Gerasimova, C. Gerth, B. Schmidt, E. A. Schneidmiller, S. Serkez, S. Wesch, and M. V. Yurkov, "Constraints on photon pulse duration from longitudinal electron beam diagnostics at a soft x-ray free-electron laser," *Phys. Rev. ST Accel. Beams*, vol. 15, p. 030707, Mar 2012.

[42] D. Bradley, B. Liddy, and W. Sleat, "Direct linear measurement of ultrashort light pulses with a picosecond streak camera," *Optics Communications*, vol. 2, no. 8, pp. 391–395, 1971.

[43] J. M. Schins, P. Breger, P. Agostini, R. C. Constantinescu, H. G. Muller, G. Grillon, A. Antonetti, and A. Mysyrowicz, "Observation of laser-assisted auger decay in argon," *Phys. Rev. Lett.*, vol. 73, pp. 2180–2183, Oct 1994.

[44] J. Itatani, F. Quéré, G. L. Yudin, M. Y. Ivanov, F. Krausz, and P. B. Corkum, "Attosecond streak camera," *Phys. Rev. Lett.*, vol. 88, p. 173903, Apr 2002.

[45] R. Kienberger, E. Goulielmakis, M. Uiberacker, A. Baltuska, V. Yakovlev, F. Bammer, A. Scrinzi, T. Westerwalbesloh, U. Kleineberg, U. Heinzmann, M. Drescher, and F. Krausz, "Atomic transient recorder," *Nature*, vol. 427, pp. 817–821, Feb 2004.

[46] P. B. Corkum and F. Krausz, "Attosecond science," *Nature Physics*, vol. 3, pp. 381–387, Jun 2007.

[47] A. M. Dykhne and G. L. Yudin, "Stimulated effects upon "jarring" of an electron in an external electromagnetic field," vol. 20, pp. 80–86, jan 1977.

[48] P. B. Corkum, N. H. Burnett, and F. Brunel, "Above-threshold ionization in the long-wavelength limit," *Phys. Rev. Lett.*, vol. 62, pp. 1259–1262, Mar 1989.

[49] T. F. Gallagher, "Above-threshold ionization in low-frequency limit," *Phys. Rev. Lett.*, vol. 61, pp. 2304–2307, Nov 1988.

[50] F. Quéré, Y. Mairesse, and J. Itatani, "Temporal characterization of attosecond xuv fields," *Journal of Modern Optics*, vol. 52, no. 2-3, pp. 339–360, 2005.

[51] R. Kienberger, M. Hentschel, M. Uiberacker, C. Spielmann, M. Kitzler, A. Scrinzi, M. Wieland, T. Westerwalbesloh, U. Kleineberg, U. Heinzmann, M. Drescher, and F. Krausz, "Steering attosecond electron wave packets with light," *Science*, vol. 297, no. 5584, pp. 1144–1148, 2002.

[52] M. Drescher, M. Hentschel, R. Kienberger, G. Tempea, C. Spielmann, G. A. Reider, P. B. Corkum, and F. Krausz, "X-ray pulses approaching the attosecond frontier," *Science*, vol. 291, no. 5510, pp. 1923–1927, 2001.

[53] L. V. Keldysh *et al.*, "Diagram technique for nonequilibrium processes," *Sov. Phys. JETP*, vol. 20, no. 4, pp. 1018–1026, 1965.

[54] U. Frühling, "Light-field streaking for FELs," *Journal of Physics B: Atomic, Molecular and Optical Physics*, vol. 44, p. 243001, nov 2011.

[55] V. Schmidt, N. Sandner, W. Mehlhorn, M. Y. Adam, and F. Wuilleumier, "Post-collision interaction in the xenon $N_{4,5} - oo$ auger spectrum excited by photon impact," *Phys. Rev. Lett.*, vol. 38, pp. 63–66, Jan 1977.

[56] W. Mehlhorn, "70 years of auger spectroscopy, a historical perspective," *Journal of Electron Spectroscopy and Related Phenomena*, vol. 93, no. 1, pp. 1–15, 1998.

[57] B. Schütte, S. Bauch, U. Frühling, M. Wieland, M. Gensch, E. Plönjes, T. Gaumnitz, A. Azima, M. Bonitz, and M. Drescher, "Evidence for chirped auger-electron emission," *Phys. Rev. Lett.*, vol. 108, p. 253003, Jun 2012.

[58] A. K. Kazansky, I. P. Sazhina, and N. M. Kabachnik, "Time-dependent theory of auger decay induced by ultra-short pulses in a strong laser field," *Journal of Physics B: Atomic, Molecular and Optical Physics*, vol. 42, p. 245601, dec 2009.

[59] S. Bauch and M. Bonitz, "Theoretical description of field-assisted postcollision interaction in auger decay of atoms," *Phys. Rev. A*, vol. 85, p. 053416, May 2012.

[60] P. Schmüser, M. Dohlus, and J. Rossbach, *Ultraviolet and Soft X-Ray Free-Electron Lasers*. Berlin: Springer, 2008.

[61] K. Tiedtke, A. Azima, N. von Bargen, L. Bittner, S. Bonfigt, S. Düsterer, B. Faatz, U. Frühling, M. Gensch, C. Gerth, N. Guerassimova, U. Hahn, T. Hans, M. Hesse, K. Honkavaar, U. Jastrow, P. Juranic, S. Kapitzki, B. Keitel, T. Kracht, M. Kuhlmann, W. B. Li, M. Martins, T. Núñez, E. Plönjes, H. Redlin, E. L. Saldin, E. A. Schneidmiller, J. R. Schneider, S. Schreiber, N. Stojanovic, F. Tavella, S. Toleikis, R. Treusch, H. Weigelt, M. Wellhöfer, H. Wabnitz, M. V. Yurkov, and J. Feldhaus, "The soft x-ray free-electron laser FLASH at DESY: beamlines, diagnostics and end-stations," *New Journal of Physics*, vol. 11, p. 023029, feb 2009.

[62] J. Rossbach, J. R. Schneider, and W. Wurth, "10 years of pioneering x-ray science at the free-electron laser flash at desy," *Physics Reports*, vol. 808, pp. 1–74, 2019. 10 years of pioneering X-ray science at the Free-Electron Laser FLASH at DESY.

[63] B. Faatz, M. Braune, O. Hensler, K. Honkavaara, R. Kammering, M. Kuhlmann, E. Ploenjes, J. Roensch-Schulenburg, E. Schneidmiller, S. Schreiber, K. Tiedtke, M. Tischer, R. Treusch, M. Vogt, W. Wurth, M. Yurkov, and J. Zemella, "The flash facility: Advanced options for flash2 and future perspectives," *Applied Sciences*, vol. 7, no. 11, 2017.

[64] B. Faatz, E. Plönjes, S. Ackermann, A. Agababyan, V. Asgekar, V. Ayvazyan, S. Baark, N. Baboi, V. Balandin, N. von Bargen, Y. Bican, O. Bilani, J. Bödewadt, M. Böhnert, R. Böspflug, S. Bonfigt, H. Bolz, F. Borges, O. Borkenhagen, M. Brachmanski, M. Braune, A. Brinkmann, O. Brovko, T. Bruns, P. Castro, J. Chen, M. K. Czwalinna, H. Damker, W. Decking, M. Degenhardt, A. Delfs, T. Delfs, H. Deng, M. Dressel, H.-T. Duhme, S. Düsterer, H. Eckoldt, A. Eislage, M. Felber, J. Feldhaus, P. Gessler, M. Gibau, N. Golubeva, T. Golz, J. Gonschior, A. Grebentsov, M. Grecki, C. Grün, S. Grunewald, K. Hacker, L. Hänisch, A. Hage, T. Hans, E. Hass, A. Hauberg, O. Hensler, M. Hesse, K. Heuck, A. Hidvegi, M. Holz, K. Honkavaara, H. Höppner, A. Ignatenko, J. Jäger, U. Jastrow, R. Kammering, S. Karstensen, A. Kaukher, H. Kay, B. Keil, K. Klose, V. Kocharyan, M. Köpke, M. Körfer, W. Kook, B. Krause, O. Krebs, S. Kreis, F. Krivan, J. Kuhlmann, M. Kuhlmann, G. Kube, T. Laarmann, C. Lechner, S. Lederer, A. Leuschner, D. Liebertz, J. Liebing, A. Liedtke, L. Lilje, T. Limberg, D. Lipka, B. Liu, B. Lorbeer, K. Ludwig, H. Mahn, G. Marinkovic, C. Martens, F. Marutzky, M. Maslocv, D. Meissner, N. Mildner, V. Miltchev, S. Molnar, D. Mross, F. Müller, R. Neumann, P. Neumann, D. Nölle, F. Obier, M. Pelzer, H.-B. Peters, K. Petersen, A. Petrosyan, G. Petrosyan, L. Petrosyan, V. Petrosyan, A. Petrov, S. Pfeiffer, A. Piotrowski, Z. Pisarov, T. Plath, P. Pototzki, M. J. Prandolini, J. Prenting, G. Priebe, B. Racky, T. Ramm, K. Rehlich, R. Riedel, M. Roggli, M. Röhling, J. Rönsch-Schulenburg, J. Rossbach, V. Rybnikov, J. Schäfer, J. Schaffran, H. Schlarb, G. Schlesselmann, M. Schlösser, P. Schmid, C. Schmidt, F. Schmidt-Föhre, M. Schmitz, E. Schneidmiller, A. Schöps, M. Scholz, S. Schreiber, K. Schütt, U. Schütz, H. Schulte-Schrepping, M. Schulz, A. Shabunov, P. Smirnov, E. Sombrowski, A. Sorokin, B. Sparr, J. Spengler, M. Staack, M. Stadler, C. Stechmann, B. Steffen, N. Stojanovic, V. Sychev, E. Syresin, T. Tanikawa, F. Tavella, N. Tesch, K. Tiedtke, M. Tischer, R. Treusch, S. Tripathi, P. Vagin, P. Vetrov, S. Vilcins, M. Vogt, A. de Zubiaurre Wagner, T. Wamsat, H. Weddig, G. Weichert, H. Weigelt, N. Wentowski, C. Wiebers, T. Wilksen, A. Willner, K. Wittenburg, T. Wohlenberg, J. Wortmann, W. Wurth, M. Yurkov, I. Zagorodnov, and J. Zemella, "Simultaneous operation of two soft x-ray free-electron lasers driven by one linear accelerator," *New Journal of Physics*, vol. 18, p. 062002, jun 2016.

[65] J. Feldhaus, "FLASH—the first soft x-ray free electron laser (FEL) user facility," *Journal of Physics B: Atomic, Molecular and Optical Physics*, vol. 43, p. 194002, sep 2010.

[66] S. Toleikis, "The flash facility current status in 2018 and future upgrade plans," *AIP Conference Proceedings*, vol. 2054, no. 1, p. 030015, 2019.

[67] M. Martins, M. Wellhöfer, J. Hoeft, W. Wurth, J. Feldhaus, and R. Follath, "Monochromator beamline for flash," *Review of Scientific Instruments*, vol. 77, pp. 115108–115108, 11 2006.

[68] N. Gerasimova, S. Dziarzhytski, and J. Feldhaus, "The monochromator beamline at flash: Performance, capabilities and upgrade plans," *Journal of Modern Optics*, vol. 58, pp. 1480–1485, 09 2011.

[69] K. Tiedtke *et al.*, "Gas detectors for x-ray lasers," *Journal of Applied Physics*, vol. 103, pp. 094511 – 094511, 06 2008.

[70] A. A. Sorokin, Y. Bican, S. Bonfigt, M. Brachmanski, M. Braune, U. F. Jastrow, A. Gottwald, H. Kaser, M. Richter, and K. Tiedtke, "An X-ray gas monitor for free-electron lasers," *Journal of Synchrotron Radiation*, vol. 26, pp. 1092–1100, Jul 2019.

[71] G. Brenner, S. Kapitzki, M. Kuhlmann, E. Ploenjes, T. Noll, F. Siewert, R. Treusch, K. Tiedtke, R. Reininger, M. Roper, M. Bowler, F. Quinn, and J. Feldhaus, "First results from the online variable line spacing grating spectrometer at flash," *Nuclear Instruments and Methods in Physics Research Section A: Accelerators, Spectrometers, Detectors and Associated Equipment*, vol. 635, no. 1, Supplement, pp. S99–S103, 2011. PhotonDiag 2010.

[72] M. Wellhöfer, J. T. Hoeft, M. Martins, W. Wurth, M. Braune, J. Viefhaus, K. Tiedtke, and M. Richter, "Photoelectron spectroscopy as a non-invasive method to monitor SASE-FEL spectra," *Journal of Instrumentation*, vol. 3, pp. P02003–P02003, feb 2008.

[73] M. Braune, G. Brenner, S. Dziarzhytski, P. Juranić, A. Sorokin, and K. Tiedtke, "A non-invasive online photoionization spectrometer for FLASH2," *Journal of Synchrotron Radiation*, vol. 23, pp. 10–20, Jan 2016.

[74] M. Braune, J. Buck, M. Kuhlmann, S. Grunewald, S. Düsterer, J. Viefhaus, and K. Tiedtke, "Non-invasive online wavelength measurements at FLASH2 and present benchmark," *Journal of Synchrotron Radiation*, vol. 25, pp. 3–15, Jan 2018.

[75] F. Frassetto, S. Coraggia, N. Gerasimova, S. Dziarzhytski, T. Golz, H. Weigelt, and L. Poletto, "Compact spectrometer for photon diagnostics of the extreme-ultraviolet free-electron-laser radiation," *Nuclear Instruments and Methods in Physics Research Section A: Accelerators, Spectrometers, Detectors and Associated Equipment*, vol. 635, no. 1, Supplement, pp. S94–S98, 2011. PhotonDiag 2010.

[76] F. Frassetto, S. Coraggia, S. Dziarzhytski, N. Gerasimova, and L. Poletto, "Extreme-ultraviolet compact spectrometer for the characterization of the harmonics content in the free-electron-laser radiation at FLASH," *Journal of Synchrotron Radiation*, vol. 19, pp. 596–601, Jul 2012.

[77] F. Frassetto, S. Dziarzhytski, N. Guerassimova, and L. Poletto, "Compact spectrometer for on-line photon diagnostics at FLASH," *Journal of Physics: Conference Series*, vol. 425, p. 122010, mar 2013.

[78] O. H. Altenmueller, R. R. Larsen, and G. A. Loew, "Investigations of traveling-wave separators for the stanford two-mile linear accelerator," *Review of Scientific Instruments*, vol. 35, no. 4, pp. 438–442, 1964.

[79] M. Röhrs, C. Gerth, H. Schlarb, B. Schmidt, and P. Schmüser, "Time-resolved electron beam phase space tomography at a soft x-ray free-electron laser," *Phys. Rev. ST Accel. Beams*, vol. 12, p. 050704, May 2009.

[80] Y. Ding, C. Behrens, P. Emma, J. Frisch, Z. Huang, H. Loos, P. Krejcik, and M.-H. Wang, "Femtosecond x-ray pulse temporal characterization in free-electron lasers using a transverse deflector," *Phys. Rev. ST Accel. Beams*, vol. 14, p. 120701, Dec 2011.

[81] P. Craievich *et al.*, "Status of the Polarix-TDS Project," in *Proc. 9th International Particle Accelerator Conference (IPAC'18), Vancouver, BC, Canada, April 29-May 4, 2018*, no. 9 in International Particle Accelerator Conference, (Geneva, Switzerland), pp. 3808–3811, JACoW Publishing, June 2018. https://doi.org/10.18429/JACoW-IPAC2018-THPAL068.

[82] S. Schulz, I. Grguraš, C. Behrens, H. Bromberger, J. T. Costello, M. K. Czwalinna, M. Felber, M. C. Hoffmann, M. Ilchen, H. Y. Liu, T. Mazza, M. Meyer, S. Pfeiffer, P. Prędki, S. Schefer, C. Schmidt, U. Wegner, H. Schlarb, and A. L. Cavalieri, "Femtosecond all-optical synchronization of an x-ray free-electron laser," *Nature Communications*, vol. 6, p. 5938, Jan 2015.

[83] A. Angelovski, M. Kuntzsch, M. K. Czwalinna, A. Penirschke, M. Hansli, C. Sydlo, V. Arsov, S. Hunziker, H. Schlarb, M. Gensch, V. Schlott, T. Weiland, and R. Jakoby, "Evaluation of the cone-shaped pickup performance for low charge sub-10 fs arrival-time measurements at free electron laser facilities," *Phys. Rev. ST Accel. Beams*, vol. 18, p. 012801, Jan 2015.

[84] U. Frühling, *Light field driven streak-camera for single-shot measurement of the temporal profile of XUV-pulses from a free-electron laser*. Dissertation, University of Hamburg, 2009.

[85] I. Grguraš, *Time resolved photoelectron spectroscopy for femtosecond characterization of X-ray free-electron laser pulses*. Dissertation, University of Hamburg, 2015.

[86] J. Hebling, G. Almási, I. Z. Kozma, and J. Kuhl, "Velocity matching by pulse front tilting for large-area thz-pulse generation," *Opt. Express*, vol. 10, pp. 1161–1166, Oct 2002.

[87] K. Ravi, W. R. Huang, S. Carbajo, E. A. Nanni, D. N. Schimpf, E. P. Ippen, and F. X. Kärtner, "Theory of terahertz generation by optical rectification using tilted-pulse-fronts," *Opt. Express*, vol. 23, pp. 5253–5276, Feb 2015.

[88] K.-L. Yeh, M. C. Hoffmann, J. Hebling, and K. A. Nelson, "Generation of 10μj ultrashort terahertz pulses by optical rectification," *Applied Physics Letters*, vol. 90, no. 17, p. 171121, 2007.

[89] E. Saldin, E. Schneidmiller, and M. Yurkov, "Coherence properties of the radiation from x-ray free electron laser," *Optics Communications*, vol. 281, no. 5, pp. 1179–1188, 2008.

[90] A. K. Kazansky, I. P. Sazhina, and N. M. Kabachnik, "Fast retrieval of temporal characteristics of fel pulses using streaking by thz field," *Opt. Express*, vol. 27, pp. 12939–12944, Apr 2019.

[91] M. Kuhlmann, E. A. Schneidmiller, and M. V. Yurkov, "Frequency doubler and two-color mode of operation at free electron laser FLASH2," in *Advances in X-ray Free-Electron Lasers Instrumentation IV* (T. Tschentscher and L. Patthey, eds.), vol. 10237, pp. 174 – 180, International Society for Optics and Photonics, SPIE, 2017.

[92] E. Schneidmiller, M. Braune, B. Faatz, U. Jastrow, M. Kuhlmann, A. Sorokin, K. Tiedtke, and M. Yurkov, "Two-Color Operation of FLASH2 Undulator," in *39th International Free Electron Laser Conference*, 9 2019.

[93] M. Wöstmann, R. Mitzner, T. Noll, S. Roling, B. Siemer, F. Siewert, S. Eppenhoff, F. Wahlert, and H. Zacharias, "The XUV split-and-delay unit at beamline BL2 at FLASH," vol. 46, p. 164005, aug 2013.

[94] T. Pfeifer, Y. Jiang, S. Düsterer, R. Moshammer, and J. Ullrich, "Partial-coherence method to model experimental free-electron laser pulse statistics," *Opt. Lett.*, vol. 35, pp. 3441– 3443, Oct 2010.

[95] E. Saldin, E. Schneidmiller, and M. Yurkov, "Fast: a three-dimensional time-dependent fel simulation code," *Nuclear Instruments and Methods in Physics Research Section A: Accelerators, Spectrometers, Detectors and Associated Equipment*, vol. 429, no. 1, pp. 233–237, 1999.

[96] V. Ayvazyan, N. Baboi, I. Bohnet, R. Brinkmann, M. Castellano, P. Castro, L. Catani, S. Choroba, A. Cianchi, M. Dohlus, H. T. Edwards, B. Faatz, A. A. Fateev, J. Feldhaus, K. Flöttmann, A. Gamp, T. Garvey, H. Genz, C. Gerth, V. Gretchko, B. Grigoryan, U. Hahn, C. Hessler, K. Honkavaara, M. Hüning, R. Ischebeck, M. Jablonka, T. Kamps, M. Körfer, M. Krassilnikov, J. Krzywinski, M. Liepe, A. Liero, T. Limberg, H. Loos, M. Luong, C. Magne, J. Menzel, P. Michelato, M. Minty, U.-C. Müller, D. Nölle, A. Novokhatski, C. Pagani, F. Peters, J. Pflüger, P. Piot, L. Plucinski, K. Rehlich, I. Reyzl, A. Richter, J. Rossbach, E. L. Saldin, W. Sandner, H. Schlarb, G. Schmidt, P. Schmüser, J. R. Schneider, E. A. Schneidmiller, H.-J. Schreiber, S. Schreiber, D. Sertore, S. Setzer, S. Simrock, R. Sobierajski, B. Sonntag, B. Steeg, F. Stephan, K. P. Sytchev, K. Tiedtke, M. Tonutti, R. Treusch, D. Trines, D. Türke, V. Verzilov, R. Wanzenberg, T. Weiland, H. Weise, M. Wendt, T. Wilhein, I. Will, K. Wittenburg, S. Wolff, M. V. Yurkov, and K. Zapfe, "A new powerful source for coherent vuv radiation: Demonstration of exponential growth and saturation at the ttf free-electron laser," *The European Physical Journal D - Atomic, Molecular, Optical and Plasma Physics*, vol. 20, pp. 149–156, Jul 2002.

[97] S. Roling, B. Siemer, M. Wöstmann, H. Zacharias, R. Mitzner, A. Singer, K. Tiedtke, and I. A. Vartanyants, "Temporal and spatial coherence properties of free-electron-laser pulses in the extreme ultraviolet regime," *Phys. Rev. ST Accel. Beams*, vol. 14, p. 080701, Aug 2011.

[98] E. L. Saldin, E. A. Schneidmiller, and M. V. Yurkov, "Properties of the third harmonic of the radiation from self-amplified spontaneous emission free electron laser," *Phys. Rev. ST Accel. Beams*, vol. 9, p. 030702, Mar 2006.

[99] H. Freund, S. Biedron, and S. Milton, "Nonlinear harmonic generation and proposed experimental verification in sase fels," *Nuclear Instruments and Methods in Physics Research Section A: Accelerators, Spectrometers, Detectors and Associated Equipment*, vol. 445, no. 1, pp. 53–58, 2000.

[100] T. Oelze, O. Kulyk, B. Schütte, U. Frühling, E. Klimešová, B. Jagielski, L. Dittrich, M. Drescher, R. Pan, N. Stojanovic, V. Polovinkin, K. P. Khakurel, K. Muehlig, I. J. B. Macias, S. Düsterer, B. Faatz, J. Andreasson, M. Wieland, and M. Krikunova, "Thz streak camera performance for single-shot characterization of xuv pulses with complex temporal structures," *Opt. Express*, vol. 28, pp. 20686–20703, Jul 2020.

[101] K. Wenig, M. Wieland, A. Baumann, S. Walther, A. Dimitriou, M. J. Prandolini, O. Schepp, I. Bermúdez Macias, M. Sumfleth, N. Stojanovic, S. Düsterer, J. Rönsch-Schulenburg, E. Zapolnova, R. Pan, M. Drescher, and U. Frühling, "Electronic decay of core-excited hcl molecules probed by thz streaking," *Structural Dynamics*, vol. 6, no. 3, p. 034301, 2019.

[102] A. Niehaus, "Analysis of post-collision interactions in auger processes following near-threshold inner-shell photoionization," *Journal of Physics B: Atomic and Molecular Physics*, vol. 10, pp. 1845–1857, jul 1977.

[103] G. B. Armen, J. Tulkki, T. Aberg, and B. Crasemann, "Quantum theory of post-collision interaction in inner-shell photoionization: Final-state interaction between two continuum electrons," *Phys. Rev. A*, vol. 36, pp. 5606–5614, Dec 1987.

[104] M. Drescher, M. Hentschel, R. Kienberger, M. Uiberacker, V. Yakovlev, A. Scrinzi, T. Westerwalbesloh, U. Kleineberg, U. Heinzmann, and F. Krausz, "Time-resolved atomic inner-shell spectroscopy," *Nature*, vol. 419, pp. 803–807, Oct 2002.

[105] M. Drescher, M. Hentschel, R. Kienberger, M. Uiberacker, T. Westerwalbesloh, U. Kleineberg, U. Heinzmann, and F. Krausz, "Time-resolved electron spectroscopy of atomic inner-shell dynamics," *Journal of Electron Spectroscopy and Related Phenomena*, vol. 137-140, pp. 259–264, 2004. ICESS-9 Proceedings of the 9th International Conference on Electronic Spectroscopy and Structure.

[106] A. Russek and W. Mehlhorn, "Post-collision interaction and the auger lineshape," *Journal of Physics B: Atomic and Molecular Physics*, vol. 19, pp. 911–927, mar 1986.

[107] L. O. Werme, T. Bergmark, and K. Siegbahn, "The high Resolution$L_{2,3}$mmand$m_{4,5}$nnauger spectra from krypton and$M_{4,5}$nnand$n_{4,5}$ooauger spectra from xenon," *Physica Scripta*, vol. 6, pp. 141–150, aug 1972.

[108] M. Jurvansuu, A. Kivimäki, and S. Aksela, "Inherent lifetime widths of ar $2p^{-1}$, kr $3d^{-1}$, xe $3d^{-1}$, and xe $4d^{-1}$ states," *Phys. Rev. A*, vol. 64, p. 012502, Jun 2001.

[109] N. Hartmann, G. Hartmann, R. Heider, M. S. Wagner, M. Ilchen, J. Buck, A. O. Lindahl, C. Benko, J. Grünert, J. Krzywinski, J. Liu, A. A. Lutman, A. Marinelli, T. Maxwell, A. A. Miahnahri, S. P. Moeller, M. Planas, J. Robinson, A. K. Kazansky, N. M. Kabachnik, J. Viefhaus, T. Feurer, R. Kienberger, R. N. Coffee, and W. Helml, "Attosecond time–energy structure of x-ray free-electron laser pulses," *Nature Photonics*, vol. 12, pp. 215–220, Apr 2018.

Acknowledgments

The completion of this work was only possible with the support of a lot of great people around me. Firstly, I would like to thank Stefan D., my supervisor at FLASH-DESY, for believing in my potential and giving me the opportunity to realize this thesis. Thank you for your guidance, teaching and patience during my PhD. You always made me feel that I was a valuable part of the streaking team. I would also like to thank Rosen I., for the great support with the experiments and the interpretation of the data. Stefan D., Rosen I. and I had uncountable streaking beamtimes together and I'm grateful for everything that I learned throughout them. Furthermore, I would like to thank Ulrike F., my university supervisor, for her guidance and the great ideas that ended up in new experiments. Special thanks to Nikolay K., who guided my theoretical work during my PhD. Thank you for your support and for the very important feedback regarding my streaking simulations. Your advice was always very much appreciated.

All the experiments at FLASH wouldn't be achieved without the great effort of the whole FLASH-team. Therefore, I would like to acknowledge and thank everyone at FLASH for making such a big machine and complex experiments happen. I would like to thank Erland M., Mikhail Y., Juliane R-S., Marion K., Sören G., Christopher P., Jan S., Siarhei S., Kai T., Elke P., Sven T., Martin B., Günter B., Rolf T., Robin E., Kostja K., Rui P., Mahdi M., Georgia P. and Mabel L-R. from the FLASH-team. Our paths crossed at some point during my PhD and I am thankful for your support when needed. I could not finish thanking the FLASH-team without thanking Hannah G. You "saved my life" so many times, thank you for your excellent work.

A very warm and special thanks to Katja Z. Thank you for being such a good friend and strong support through the good and the tough times. You are a great example of the things that can be achieved after finishing a PhD and I am always very inspired and motivated by you. So thank you for your invaluable input and support all these years.

I would like to extend my deepest gratitude to Dan H., who was there to support me from the beginning of my PhD. Thank you for your friendship, for the countless "streaking"-related discussions, for all the physics/programming-related discussions and for proof-reading a lot of my work. I feel indebted to your support.

I would also like to thank Robin E. and Kostja K., my PhD colleagues and friends. I'm very thankful for your support, for enduring sharing the office with me (and making our office a very nice place to work), for all the good talks during the coffee breaks, for all the sharing of ideas and knowledge, for listening to my uncountable rehearsal talks and for always giving me valuable constructive feedback. Thank you Robin E. for proof-reading my papers and my thesis, your feedback was always most appreciated.

In addition, I would like to thank Nina H., Masha P. and Dan H. that together with Robin E. and Kostja K. made the most fun boardgames and DnD evenings. Thank you guys for your friendship, support and for always being there for me.

Finally, I would like to thank Stephan N. for his support at the "last stage" of my PhD. Writing a thesis and finishing up a PhD is not an easy task but I was lucky enough to have you by my side to support me during these times. Thank you very much for your unconditional support.

I would like to end this list of acknowledgements by thanking all my family back in Mexico, and specially my mom. My mom has always supported my decisions and encouraged me to pursue my dreams and goals. Without her support I definitely wouldn't be where I am now. ¡Gracias mami! te dedico todos estos años de trabajo y sus frutos.

Eidesstattliche Versicherung
Declaration of oath

Hiermit versichere ich an Eides statt, dass ich die vorliegende Dissertationsschrift selbst verfasst und keine anderen als die angegebenen Hilfsmittel und Quellen benutzt habe. Die eingereichte schriftliche Fassung entspricht der auf dem elektronischen Speichermedium. Die Dissertation wurde in der vorgelegten oder einer ähnlichen Form nicht schon einmal in einem früheren Promotionsverfahren angenommen oder als ungen ügend beurteilt.

I hereby declare, on oath, that I have written the present dissertation by my own and have not used any resources and aids other than those acknowledged. The written version submitted corresponds to the one stored electronically. The dissertation presented in this form, has not already been accepted in an earlier doctoral procedure or assessed as unsatisfactory.

Hamburg 2022,

Ivette Jazmín Bermúdez Macias